SOLID-STATE DEWETTING OF MAGNETIC BINARY ALLOY THIN FILMS AND APPLICATION AS NANOWIRE AND NANOTUBE GROWTH CATALYSTS

RIA ESTERINA

(M.Eng., Massachusetts Institute of Technology)

A THESIS SUBMITTED

FOR THE DEGREE OF DOCTOR OF PHILOSOPHY

IN ADVANCED MATERIALS FOR MICRO- AND NANO-SYSTEMS (AMM&NS)

SINGAPORE-MIT ALLIANCE

NATIONAL UNIVERSITY OF SINGAPORE

2014

DECLARATION

I hereby declare that this thesis is my original work

and it has been written by me in its entirety.

I have duly acknowledged all the sources of

information which have been used in the thesis.

This thesis has also not been submitted for any

degree in any university previously.

_____

Ria Esterina

2014

Acknowledgements

First, I would like to express my utmost gratitude to my thesis supervisors, Professor Caroline Ross, Professor Adekunle Adeyeye and Professor Choi Wee Kiong. I have had the great privilege to work under their guidance and support. I would never finish my thesis without their encouragement and unlimited patience. I am also very grateful for the useful discussions I had with my thesis committee, Professor Carl Thompson, Professor Fitzgerald and Professor Vivian Ng, for their insightful advice, suggestions and ideas.

I must also give credit to Walter Lim, Xiao Yun, and Ah Lian Kiat as the technologists of Microelectronics Lab, where I carried out most of my experiments. I would also like to thank my friends in Microelectronics Lab, ISML and SMA who have helped me facing various challenges in study and work.

Special thanks go to my best friend and dearest Yudi. Thank you for always being there for me. I also thank my dear sister, Renna, for her constant encouragement. I would like to dedicate this thesis to my parents, Handoyo and Hoen Fong. I would not have made this far without your unconditional love, support, and prayers. Finally and most importantly, I would like to give thanks to the Lord Jesus for without Him I can do nothing.

Table of Contents

Summary

The objective of this study was to conduct a systematic study of solid-state dewetting process of CoPd and CoAu as representatives of miscible and immiscible alloy systems. Specifically, the objectives were to investigate the dewetting stages, dewetting kinetics, dewetted particles morphology and microstructures. We also characterized the magnetic properties of the particles and explored their potential application as nanowire and nanotube catalysts.

First, we established that CoPd alloy undergoes similar dewetting stages to elemental materials. We found that interstage transition and particle morphologies are material-dependent, particularly determined by surface diffusivity. Equilibrium shape of the dewetted particles are predicted using Winterbottom construction, and compared with experimental results. Plotting the area fraction transformed as a function of homologous temperature allows one to distinguish the effect of crystal structure. Johnson-Mehl-Avrami (JMA) analysis was employed to extract kinetic parameters of dewetting, namely void incubation time and dewetting activation energy. It was concluded that void initiation is governed by surface diffusion.

Next, we investigate the dewetting characteristics of CoAu thin film. We established that CoAu alloy also undergoes similar stages of dewetting as elemental materials. We found that interstage transition and dewetting morphology depend on alloy composition. Three possible scenarios were proposed to distinguish the dewetting morphologies for different Au/Co thickness ratio. For CoAu alloy with high Au composition (Au-to-Co volume ratio $\geq$ 1.5), Au-rich particles and Co-rich particles are distinguishable and we are able to predict the interparticle spacings and particle densities. For this

range of composition, we demonstrated the possibility to create clusters of nanoparticles array without resorting to lithography.

The as-deposited films show the expected in-plane magnetic shape anisotropy. After annealing, the magnetic behavior of dewetted nanoparticles show little anisotropy due to low magnetocrystalline and shape anisotropy of the nearly spherical fcc particles. Exchange interaction between Pd and Co resulted in an increase in the total M_s. For CoAu system, the hysteresis loops are similar to Co because Co-Au is an immiscible system and the magnetic contribution comes solely from Co. The M_s of Co and CoAu nanoparticles slightly decreased due to post-annealing oxidation.

Finally, we demonstrated a simple technique to fabricate SiO_2 nanowires and nanotubes on oxidized Si substrate using CoPd and Pd catalyst via vapor-liquid-solid (VLS) or vapor-solid-solid (VSS) mechanism without using external Si source. The growth occurred when the catalysts are annealed in forming gas which will induce the formation of craters in the oxide layer and lead to the formation of pits in the Si substrate which supplied Si for the nanowire growth. We demonstrated that the thermal budget can be reduced by using CoPd alloy as catalyst compared to Pd. Some of the nanotubes had a series of embedded sub-catalysts that formed branches from the primary nanotube, opening the possibility to grow more complex nanostructures. We also showed that the resulted morphologies depend on the catalyst size, i.e. smaller catalysts give nanowires and larger catalysts give nanotubes. Based on this finding, we have fabricated an array of nanowires using interference lithography patterning technique.

List of Tables

List of Figures

Figure 2.11: Schematic diagram of rim instability. (a) The rim thickens as it recedes and slows down. (b) Perturbation develops in the rim, the thinner part retracts faster than the rest. (c) A series of perturbations in the rim. (d) A series

List of Symbols

2D	Two-dimensional
3D	Three-dimensional
a	Average interparticle spacing
A	Hamaker constant
AC	Alternating Current
AE	Auger electrons
A_f	Facet area
AFM	Atomic Force Microscopy
Ag	Silver
Al	Aluminum
Al_2O_3	Aluminum Oxide
A_P	Empirically determined constant for vapor pressure
Ar	Argon
ARC	Anti-Reflection Coating
A_{sor}	Area of evaporation source
Au	Gold
AuAg	Gold Silver
AuFe	Gold Iron
AuPt	Gold Platinum
A(t)	Time component of the film perturbation
bcc	Body-centered cubic
B	Magnetic induction field
BHF	Buffered Hydrofluoric acid
B^S	Kinetic and material coefficient
BSE	Backscattered electrons
C	A constant in steric repulsion energy equation
Co	Cobalt

CoAu	Cobalt Gold
CoFe	Cobalt Iron
CoO	Cobalt Oxide
CoPd	Cobalt Palladium
CoPt	Cobalt Platinum
Cu	Copper
CuNi	Copper Nickel
CuS	Copper Monosulfide
d	Grain boundary groove depth
D	Particle density
DC	Direct Current
D_S	Surface diffusivity
D_{S0}	Surface diffusion constant
DI	De-ionized
DNA	Deoxyribonucleic acid
D_0	Particle density for film thickness of 25 nm
EDX	Energy Dispersive X-ray spectroscopy
E_A	Dewetting activation energy
E_{MS}	Magnetostatic energy
E_{Si}	Elastic modulus of Si
E_{tot}	Magnetic anisotropy total energy
E_0	Energy of primary electron
E_σ	Magnetoelastic energy
fcc	Face-centered cubic
fct	Face-centered tetragonal
Fe	Iron
Fe_2O_3	Iron Oxide
FESEM	Field Emission Scanning Electron Microscopy
Ga	Gallium

h	Film thickness
H	Magnetic field
hcp	Hexagonal close-packed
HeCd	Helium Cadmium
h_{eq}	Equilibrium film thickness
HF	Hydrofluoric acid
HRTEM	High-Resolution Transmission Electron Microscopy
h_{Si}	Si thickness in SOI structure
H_2	Hydrogen
H_2O	Water
IL	Interference Lithography
In	Indium
IP	In-plane
IPA	Isopropyl alcohol
Ir	Iridium
J	Atomic flux
JMA	Johnson-Mehl-Avrami
J_s	Curavature-driven atomic flux
J_{Si}	Si flux escaping from exposed Si surface
k	Boltzmann constant
K	Figure-of-merit to determine hole formation
k_c	Calibration coefficient in VSM measurement
KOH	Potassium Hydroxide
k_m	Wavelength with maximum growth rate
K_1	First-order magnetocrystalline anisotropy parameter
$L1_0$	Ordered phase with high magnetic anisotropy
M	Magnetic moment
Mn	Manganese
$MnPt_3$	Manganese Platinum

M_S	Saturation magnetization
M_W	Molecular weight
N_h	Number of holes per unit area
Ni	Nickel
NiAg	Nickel Silver
NiAu	Nickel Gold
N_S	Number of surface atoms per area
N_2	Nitrogen
OOP	Out-of-plane
O_2	Oxygen
p	Spatial period in IL exposure
P	Si vapor pressure
p_0	Vapor pressure in equilibrium with a plane surface
Pd	Palladium
PE	Primary Electrons
$P_{eq,T}$	Equilibrium vapor pressure at temperature T
Pt	Platinum
Q_S	Activation energy for surface diffusion
R	Grain radius
r	Particle radius
$\dot{r}$	Hole growth rate
r_c	Radius of cylinder in Rayleigh instability
R_e	Evaporation rate of atoms
RF	Radio Frequency
R_G	Gas constant
SAED	Selected-Area Electron Diffraction
SE	Secondary Electrons
SEM	Scanning Electron Microscopy
Si	Silicon

SiO	Silicon oxide vapor
SiO_2	Silicon Dioxide
SLS	Solid-Liquid-Solid
Sn	Tin
SOI	Silicon-on-insulator
t	Time
T	Temperature
t_i	Void incubation time
TEM	Transmission Electron Microscopy
T_m	Melting temperature
U	Effective voltage generated by changing magnetic flux
v	Number of atoms per unit area
V	Volume in space
v_h	Void growth rate
v_s	Surface density of atoms
v^*	Dimensionless void growth rate
VdW	Van der Waals
v_h	Void growth rate
VLS	Vapor-Liquid-Solid
V_n	Normal surface velocity
VSM	Vibrating Sample Magnetometer
VSS	Vapor-Solid-Solid
W_{sep}	Work of separation
x	x-axis in Cartesian coordinate
X	Characteristic x-ray
X_{dewet}	Fraction of agglomerated area
Z	Atomic number
z (x,t)	Film perturbation as a function of position and time
α	Constant used in grain depth estimation via

	evaporation-condensation
β	Constant used in grain depth estimation via surface diffusion
β_1	Proportionality constant for void growth rate
γ	Surface/interfacial energy
γ_f	Island surface energy per unit area
γ_{fv}	Film surface energy
γ_i	Island-substrate interface energy per unit area
γ_{max}	Maximum surface energy
γ_{min}	Minimum surface energy
γ_s	Substrate surface energy per unit area
γ_{PV}	Particle surface energy
$\gamma_{SiO2\text{-}vac}$	SiO_2 surface energy
$\gamma_{Si\text{-}SiO2}$	$Si\text{-}SiO_2$ interfacial energy
$\gamma_{Si\text{-}vac}$	Si surface energy
γ_{SP}	Particle-substrate interfacial energy
γ_{SV}	Substrate surface energy
δ	Grown oxide thickness
$\Delta E_{surface}$	Surface energy change for agglomeration of Si thin film
ΔE_{strain}	Strain energy change for agglomeration of Si thin film
ΔH_{vap}	Enthalpy of Si evaporation
η	Normalized film profile
θ	Contact angle of a droplet with the substrate
θ_{IL}	Half-angle in Lloyd's mirror IL system
θ_M	Angle between magnetization and sample surface normal
θ_{MS}	Angle between magnetization and stress direction
κ	Local surface curvature
λ	Wavelength of film perturbation

λ_E	Secondary electron escape depth
λ_{IL}	Laser wavelength in Lloyd's mirror IL system
λ_m	Perturbation wavelength with maximum growth rate
λ_{MS}	Magnetostriction constant
μ_0	Permeability in vacuum
ρ	Mass density
σ	Uniaxial stress applied along a certain direction
σ_{Si}	Biaxial stress of Si
τ	Hole incubation time
υ_{Si}	Poisson ratio of Si
ϕ	Effective interface potential
$\phi(h)_{steric}$	Steric repulsion interaction energy
$\phi(h)_{VdW}$	VdW interaction energy
ω	Vibration frequency in VSM system
Ω	Molecular volume

Chapter 1. Introduction

1.1 Background

Nanostructures started to gain much interest after an inspiring lecture by Richard Feynman in 1959, where he described the endless potential that might be realized by manipulating things on a small scale.[1] Recently, nanoparticle arrays have received considerable interest due to their potential applications in various fields such as magnetic recording media,[2,3] medicine,[4,5] optics[6,7] and catalysis.[8-10] Alloy nanoparticles in particular are interesting to study because they often have superior properties, such as higher strength or better corrosion resistance, compared to their constituents.

There are various ways to obtain nanoparticles either by top-down or bottom-up approaches. Top down approaches involve various lithography and etching processes, which offer precision in the location and morphologies of the nanostructures but suffer from high processing cost. On the other hand, bottom up approaches are simpler and lower in processing cost but suffer from lack of precision in location.

Bottom-up synthesis for nanoparticle arrays is usually categorized into gas (vapor) phase fabrication and liquid phase fabrication. Gas phase fabrication, such as pyrolysis or inert gas condensation, involves evaporation, supersaturation, gas-solid surface reaction (nucleation) and grain growth. Liquid phase fabrication, such as solvothermal reaction, sol-gel, or micellar structured media, involves liquid-surface reaction, nucleation and grain growth.

Another bottom-up synthesis of nanoparticles which gains much interest is dewetting or agglomeration process. In the dewetting process, a heat

treatment is applied on a sample coated with a thin film until the thin film agglomerates forming nanoparticles. This process is simple and applicable to almost all materials such as polymers and metals.

Various works have been done to study the dewetting process of metal thin film, both liquid-state dewetting and solid-state dewetting. However, most of the studies are on dewetting of elemental materials. In particular, for solid-state dewetting, there is limited literature about the mechanism of alloy metal dewetting. It is therefore important to conduct a more systematic study on the mechanism of alloy dewetting in order to gain more understanding of the factors that determine the microstructure, size, and density of the alloy nanoparticles and also to explore their potential applications. Cobalt Palladium (CoPd) and Cobalt Gold (CoAu) films are chosen as examples for miscible and immiscible systems. These materials have interesting magnetic and catalytic properties. The subsequent sections will describe general dewetting process of a thin film.

1.2 Dewetting of Thin Film

Dewetting is a dynamic process which occurs when thin film in a non-equilibrium state evolves into equilibrium state of one droplet or a set of droplets. The process of dewetting can generally be divided into three stages: hole generation, hole growth and hole coalescence. A droplet is usually in the form of a spherical cap satisfying the Young-Laplace equation in which the contact angle with the substrate is given by[11]:

$$cos\theta = \frac{\gamma_s - \gamma_l}{\gamma_f}$$

Equation 1.1

where γ_s is the substrate surface energy per unit area, γ_i is island-substrate interface energy per unit area and γ_f is the island surface energy per unit area. Complete wetting of the liquid is characterized by $\theta = 0$, non-wetting case is characterized by $\theta = \pi$, while partial wetting happens when $0 < \theta < \pi$ (**Figure 1.1**).

complete wetting   partial wetting   non-wetting
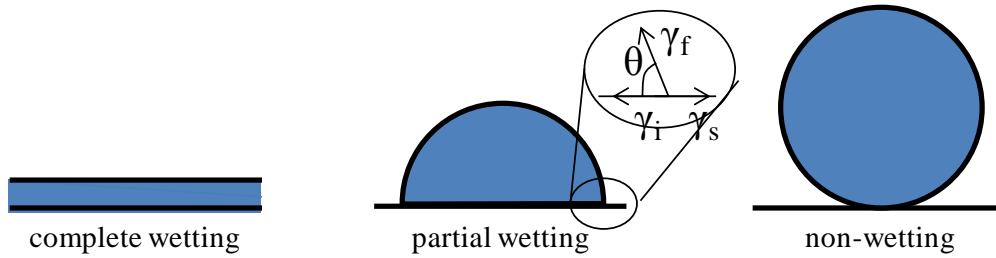
Figure 1.1: Sketch of a liquid drop at solid substrate.

There are generally two types of dewetting process of thin film, liquid-state and solid-state. In liquid-state dewetting, agglomeration can happen on thin film of polymer or metallic materials. For polymer such as polystyrene, dewetting occurs when the film is heated above its glass transition temperature, usually above 100 ℃.[12,13] Meanwhile, metal thin film dewets when it is heated up to above the melting temperature of the material, usually by laser-irradiation[14-18] or ion-irradiation[19,20].

A flat film may dewet by hole nucleation or surface instability, each of which will result in specific dewetting patterns.[21] Thiele et al.[22] has shown that for a relatively thick film, dewetting is dominated by hole nucleation process which is random and hence, the interhole spacing is not correlated with the perturbation wavelength (not ordered). On the other hand, for a thin film, dewetting is governed by surface instability where a periodic set of holes is formed corresponding to the perturbation wavelength and finally evolve into

an ordered pattern. The thickness evolution equation is similar to the Cahn-Hilliard[23] equation describing the spinodal decomposition process and thus, surface-instability-dominated dewetting is often termed as spinodal dewetting.[24] Spinodal dewetting has only been observed in very thin films of liquids or low-viscosity polymers.[24,25]

Spinodal dewetting can be described by considering the effective interface potential ϕ which is the sum of steric repulsion, which is a short-term interaction, and Van der Waals (VdW) force, which is a long-range interaction.[21] Steric repulsion is due to overlapping electron shells and for two planar surface, the interaction energy is given by: [21]

$$\phi(h)_{steric} = \frac{C}{h^8}$$

Equation 1.2

where C is a constant and h is the film thickness. The origin of the VdW force is dipole-dipole interaction between two bodies[26] and the strength is characterized by the Hamaker constant (A), which can be calculated from the optical properties of the involved materials. The VdW interaction energy is also dependent on the shape or geometry of the interacting bodies and for two surfaces (which is most relevant for the study of thin film dewetting phenomenon) is given by: [26]

$$\phi(h)_{VdW} = -\frac{A}{12\pi h^2}$$

Equation 1.3

The summation of **Equation 1.2** and **Equation 1.3** defines the stability of thin film as illustrated in **Figure 1.2**. Line (1) shows a stable film because energy is required to reduce the film thickness. Line (2) shows an unstable film where any film thicker than the equilibrium thickness h_{eq}, will minimize its total energy by developing surface undulation leading to dewetting. The value of h_{eq} is usually in order of several nanometers.[21] Line (3) shows a metastable system whereby dewetting only occurs when the energy barrier is overcome.
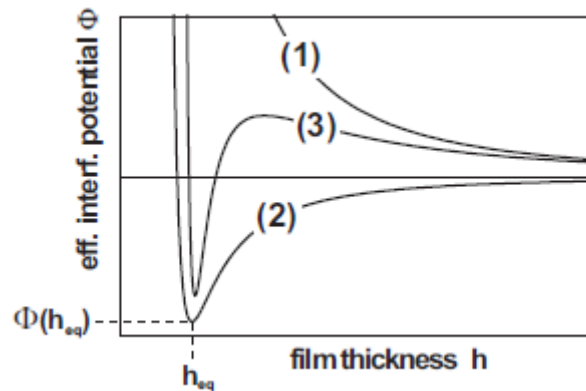
Figure 1.2: Sketch of effective interface potential as a function of film thickness. Line (1) denotes the stable case, line (2) the unstable case and line (3) the metastable case.[21]

In contrast to polymer which dewets only above its glass transition temperature, metal can dewet even at temperature below its melting point, i.e. solid-state dewetting. Solid-state dewetting is generally carried out by furnace annealing in which the thin film is heated below its melting temperature.[27-30] The process is driven by surface energy minimization via surface diffusion and the material remains in solid state. Various factors can influence the process of solid-state dewetting such as film thickness, surface self-diffusivity,

and the presence of contaminants. For polycrystalline films, grain size, grain boundary energies and grain boundary diffusivities should also be considered.[31] Depending on the intended applications, solid-state dewetting can be a more suitable approach than liquid-state dewetting to produce nanoparticles. For example, for magnetic application, solid-state dewetting is preferred because it enables the formation of magnetically hard single crystal nanoparticles, cobalt (Co) and cobalt platinum (CoPt) with $L1_0$ structure.[18,29]

Solid-state dewetting of thin film to fabricate nanoparticles has been extensively studied especially for elemental materials such as gold (Au), silver (Ag), platinum (Pt), nickel (Ni) and cobalt (Co). However, studies on the dewetting mechanisms of alloy materials both in miscible and immiscible system have not been as extensive.

1.3 Research Objectives

In view of the above review, the research gaps for the current study are summarized below:

- Solid-state dewetting is a simple yet powerful way to create nanoparticles. Studies on the dewetting mechanism of elemental materials have been reported,[27,32,33] but few have been reported on the case of alloy materials.

- Report on the microstucture and properties of alloy nanoparticles resulted from solid-state dewetting process is also limited.

- Alloy nanoparticles have various potential applications that are yet to be explored.

The main aims of this study were to conduct a mechanistic study of solid-state dewetting process of alloy materials. The specific objectives were to:

- investigate the solid-state dewetting mechanism for CoPd as a miscible system and conduct microstructural study of the CoPd nanoparticles.

- investigate the solid-state dewetting mechanism for CoAu as an immiscible system and conduct microstructural study of the CoAu nanoparticles.

- investigate the possible applications of CoPd and CoAu nanoparticles as magnetic data storage or as catalysts for nanostructure growth.

1.4   Organization of Thesis

This thesis is divided into eight chapters. Chapter 2 describes the theory of solid-state dewetting of thin film as reported in the literature. Various theories that examine the dewetting mechanism for elemental material will be elaborated. Next, studies of the dewetting mechanism for alloy materials will be discussed. Influence of templating on the dewetting behavior will also be examined.

Chapter 3 describes the experimental procedures and characterization techniques employed in this thesis.

Chapter 4 investigates the dewetting mechanism of CoPd thin film which is a miscible system. The influence of alloying on the interparticle spacings, particle sizes, and dewetting rate are presented. Microstructural characterization on the CoPd films before and after dewetting will also be conducted.

Chapter 5 investigates the dewetting mechanism of CoAu thin film which is an immiscible system.

Chapter 6 examines the magnetic properties of CoPd and CoAu nanoparticles.

Chapter 7 demonstrates the possible application of CoPd as catalysts for nanowire and nanotube growth.

Finally, Chapter 8 summarizes the thesis and proposes several recommendations for future work.

Chapter 2. Literature Review:

Solid-State Dewetting of Thin Film

2.1 Introduction

Dewetting of thin film has recently emerged as an attractive method to fabricate various metal nanoparticles, especially because it is simple and low cost. Dewetting occurs via diffusion to minimize surface energy and interface energy between film and substrate and can occur even in the solid state at temperature below the melting point of the metal thin film.[34]

This chapter will discuss the theory behind solid-state dewetting of metal thin film. Two different types of solid-state dewetting will be elaborated. The first one is dewetting of elemental material, where a thin film is deposited on top of diffusion barrier on Si substrate. The mechanism of dewetting which includes hole nucleation, hole growth, formation of interconnected islands, islands coarsening, particles morphologies and dewetting rate will be discussed. How topography or patterned film affects the dewetting behavior will also be discussed. Finally, dewetting of alloy material which can further be divided into miscible alloy and immiscible alloy will be reviewed.

2.2 Dewetting of Elemental Material

It has been shown that elemental materials undergo specific stages during the dewetting process[35,36]. Muller and Spolenak[36] have also found that miscible AuPt alloy film undergoes specific stages similar to elemental materials namely hole nucleation, hole growth and particle formation. In this section, mechanisms of solid-state dewetting of elemental material will be

presented based on hole nucleation, hole growth. interconnected islands, isolated islands, island coarsening and particle formation.

2.2.1 Hole Nucleation

An infinite defect-free thin film with all surface properties independent of orientation is stable against small perturbations, as long as the amplitude of the perturbation is smaller than the film thickness[31,37], as illustrated in **Figure 2.1**. The perturbation z can be described by Fourier components as follows,

$$z(x,t) = A(t)sin\left(\frac{2\pi x}{\lambda}\right)$$

Equation 2.1

with

$$A(t) = A(0)e^{-B^S\left(\frac{2\pi}{\lambda}\right)^4 t}$$

Equation 2.2

where B^S is a kinetic and material coefficient and λ is the perturbation wavelength. **Equation 2.2** implies that any small perturbation will decay, with higher decay rate for shorter wavelength due to the $1/\lambda$ dependence. The defect-free thin film will only start to agglomerate if the perturbation spans the film thickness and expose the substrate.
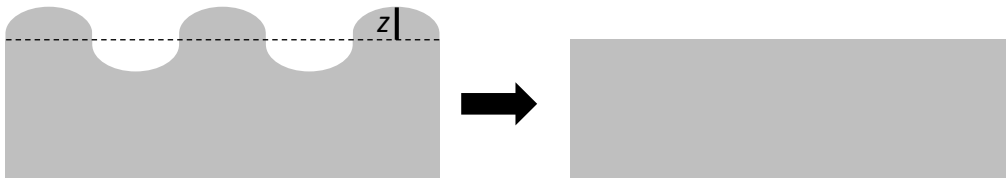
Figure 2.1: Stability of defect-free thin film.
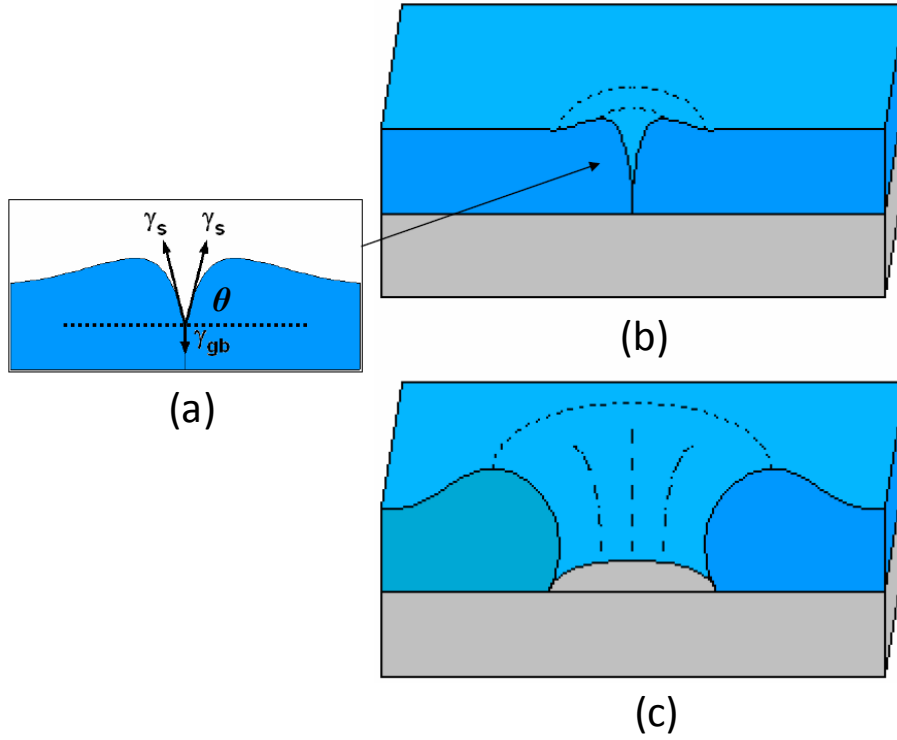
Figure 2.2: (a),(b) Two- and three-dimensional representations of grain boundary grooving. (c) Hole growth once the substrate is exposed.[38]

Mullins[39] calculated the depth d of grain boundary groove for evaporation-condensation and surface diffusion cases. For the case of evaporation-condensation,

$$d = 1.13 \, tan\theta \, (\alpha t)^{\frac{1}{2}}$$

Equation 2.3

While, for the case of surface diffusion,

$$d = 0.973 \, tan\theta \, (\beta t)^{\frac{1}{4}}$$

Equation 2.4

where $\alpha = p_0 \gamma_s \Omega^2 / (2\pi M_W)^{\frac{1}{2}} (kT)^{\frac{1}{2}}$, $\beta = D_s \gamma_s \Omega^2 \nu / kT$, p_0 is the vapor pressure in equilibrium with a plane surface, γ_s is the surface-free energy per unit area, Ω is the molecular volume and M_W is the molecular weight, D_s is the coefficient of surface diffusion and ν is the number of atoms per unit area.

Thus, Mullins showed that for both cases, d increases in time t. This implies that the groove can continue to deepen up to infinity in infinite time.

Srolovitz and Safran[40], however, showed that in realistic microstructures composed of interconnecting grain boundaries which interact with each other via surface diffusion, grain boundary groove has a finite maximum depth even if it is annealed in infinite duration. **Figure 2.3** illustrates grains in the shape of a circular base with grain diameter $2R$ and a spherical cap which intersects the grain boundary at an angle θ. The film thickness is h and the equilibrium groove depth, measured with respect to the flat film, is d. Equilibrium film depth can be written as,

$$d = R \frac{2 - 3cos\theta + cos^3\theta}{3sin^3\theta}$$

Equation 2.5

For the groove to intercept the substrate, the groove depth d must be larger than the film thickness h.
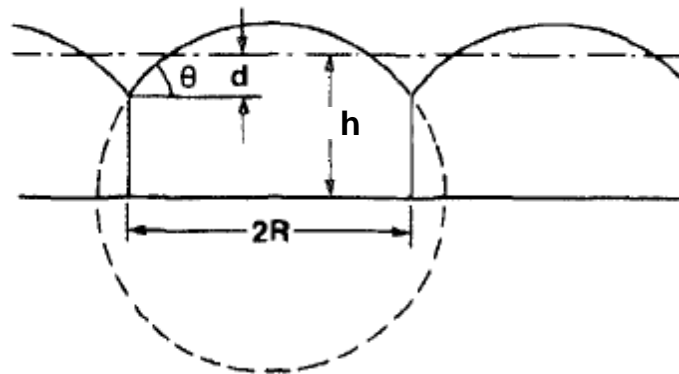
Figure 2.3: The equilibrium grain boundary groove configuration for a circular cross-section grain.[40]

However, not all holes can form due to energetic cost related to increasing surface area associated with the hole walls. For the hole to form, K should be larger than 14.5, with K given as:

$$K = \left(\frac{R}{h}\right)^2 \left(1 + \frac{\gamma_i}{\gamma_s}\right)$$

<div align="right">**Equation 2.6**</div>

where γ_i, γ_s, and γ_f are connected through the Young-Laplace equation as given in **Equation 1.1**.

Srolovitz and Safran[40] also showed that in the case of 3D thin films, the depth of holes at grain boundary triple junction, where three planar grain boundaries meet, will generally be larger than the groove depth between two grain boundaries. Thus, holes are most likely to be initiated at the triple junctions.

2.2.2 Hole Growth

The studies from both Mullins[39] and Srolovitz and Safran[40] have given good understanding of how the hole is initiated. Once the holes have formed, capillary energies will drive hole growth via edge retraction to minimize surface energy and the shape of the edge will further evolve until islands are formed. **Figure 2.4** shows an edge retraction process of an initial hole edge with a sharp corner. As illustrated in **Figure 2.4a**, material is transported from the corner by surface self-diffusion, which is generally accepted as the dominant transport mechanism in solid-state dewetting,[31] with a flux J from the edge to the flat area ahead of the edge. This flux is driven by curvature difference between the edge and the flat area. However, as the curvature gradually decreases, flux divergence occurs resulting in accumulation of mass at the edge, i.e. rim formation. Assuming isotropic energies, the flux J can be described as, [23,39]

$$J = -\left(\frac{D_s \gamma_s N_s \Omega}{kT}\right) \nabla_s \kappa$$

where N_s is the number of surface atoms per area, κ is the local surface curvature, and other variables have been defined earlier.
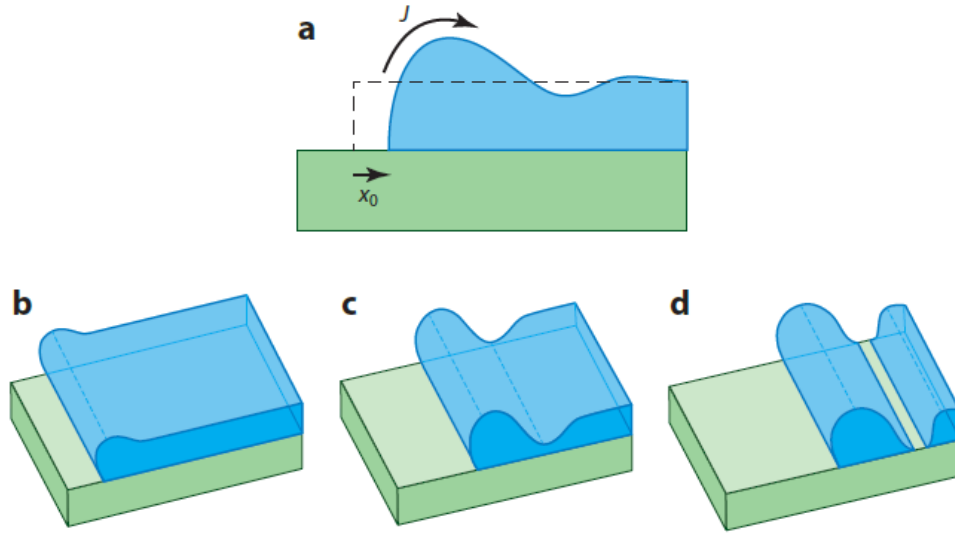
Figure 2.4: (a) Cross-sectional view of a retracting edge of a film, (b) rim thickening, (c) Deepening of the valley ahead of the rim, (d) pinch-off.[31]

The kinetics of the thin film surface evolution is described in term of the normal velocity of the surface V_n as,[39]

$$V_n = \frac{\partial h}{\partial t} = -B^S \Omega N_s^2 \kappa$$

Equation 2.8

where h is the thin film profile. Srolovitz and Safran[41] solved this equation numerically and obtain the film profile as shown in **Figure 2.5**. It can be seen that oscillation develops ahead of the rim, forming a valley in the vicinity of the rim, with amplitude diminished away from the rim. The depth of the valley increases as the edge retracts leading to pinch-off resulting in ridge detached from the film (**Figure 2.4b-d**).

14
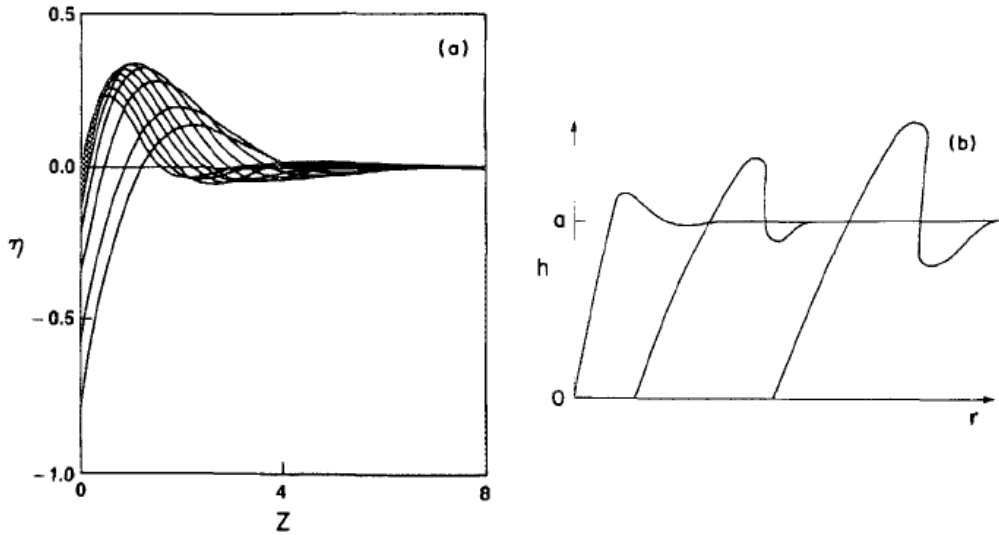
Figure 2.5: (a) The numerically calculated normalized film profile η vs. the normalized distance along the substrate axis. (b) A schematic view of the unscaled film profile.[41]

In some cases, the shapes of the holes in the dewetted film can deviate from circular into fractal-like where the rims of the holes fragmented into fingers.[30,42] **Figure 2.6** shows a comparison between circular and fractal holes. Gadkari *et al*.[42] argued that fractal morphology is associated with the amount of compressive stress in the film. At low deposition pressure, the film has high compressive stress and can develop blisters, which subsequently serve as nucleation sites for fractal growth. At high deposition pressure, the film stress is reduced and circular hole growth results. This implies that fractal morphologies occur only as a consequence of blistering.

Jiran and Thompson[43] have shown that the fractal growth is rather caused by a Rayleigh-like instability in the thickening rim. It was demonstrated that when a patterned Au film is annealed, the edge will retract accompanied by mass accumulation at the rim via surface diffusion. The edge retraction rate decreases with time due to reduced surface curvature gradient as the rim becomes thicker, following the theoretical formulation by Brandon

15

and Bradshaw[44]. However, as the rim becomes thicker, instability may develop where part of the rim is thicker than the other. Consequently, the void propagates faster through the thinnest area of the film, resulting in fractal hole morphology or what they termed as fingering instability. The void growth rate was found to be time-independent and inversely proportional to h^3, according to

$$v_h = \frac{2D_s v \Omega^2 \gamma_{fv}}{\pi k T h^3}$$

Equation 2.9
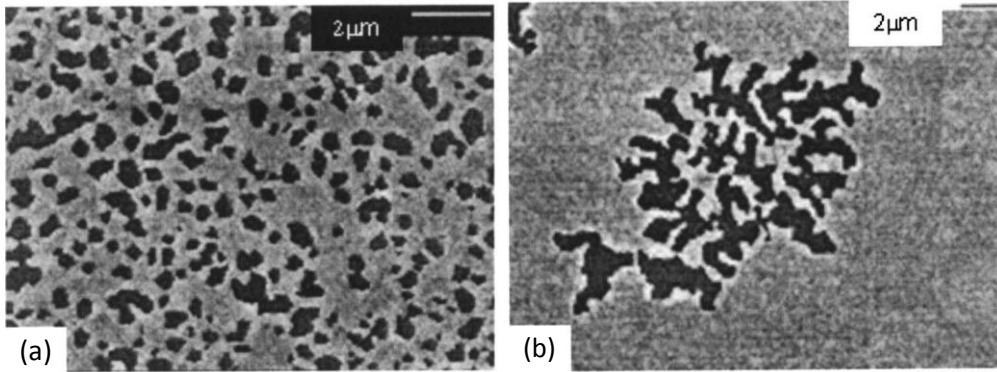
Figure 2.6: (a) Circular holes developed from 50-nm Au deposited at 20mTorr. (b) Fractal-like holes developed from 20-nm Au deposited at 4mTorr. Annealing conditions are 450 °C, 30 minutes, Ar + 3% H_2 atmosphere.[42]

Wong *et al*.[45] conducted a 2D analysis of edge retraction of a semi-infinite uniform thin film on a substrate. Assuming isotropic surface energy and surface diffusion as dominant mechanisms, by solving **Equation 2.8** numerically, they demonstrated that retracting edge forms a thickened ridge followed by a valley which sinks with time. When the valley hits the substrate, the ridge detaches from the film. The new film edge will retract again to repeat the mass shedding cycle. The edge retraction speed is constant over several shedding cycles. Although this 2D analysis cannot describe fingering instability, but the predicted retraction speed was shown to agree

16

quantitatively with Jiran and Thompson's work which observed a constant breakup speed of the annealed Au film to form isolated islands.

The relationship between the dimensionless speed v^* of Wong *et al.*'s work and the dimensional speed v_h of Jiran and Thompson's work is given by:

$$v_h = \frac{\beta_1 v^*}{h^3}$$

Equation 2.10

Kan and Wong[46] further carried out 3D analysis of this 2D film profile and showed that the edge breakdown occurs through fingering instability. They showed that growth rate of the perturbation depends on the edge retraction speed and the wavelength of the perturbation, and that perturbations with long wavelength are unstable. The analysis predicts that the wavelength of perturbation with the highest growth rate determines the distance between adjacent fingers by the following relationship,

$$\lambda_m = \frac{2\pi h}{k_m \theta}$$

Equation 2.11

where k_m is the wavenumber for maximum wavelength. The calculated wavelength agrees well with the distance between adjacent fingers in Jiran and Thompson's work.

Similar phenomenon is also observed in single-cyrstal film, such as in silicon-on-insulator (SOI)[47-49] or single crystal Ni film[50]. In single crystal film, faceting determines the initial shape of the holes. In (001) SOI thin film, agglomeration is initiated by square-shaped holes with the rims surrounding the holes forming 90° contact angle with the SiO_2 substrate and aligned along [110] and [1$\bar{1}$0] directions.[48] High local surface curvature at the edge causes

the material to flow away from the edge towards zero-surface-curvature flat region resulting in thickened rims. However, the material accumulation is less in the corner, possibly because at the corners, material can diffuse away in range of directions whereas at the edges, material can only diffuse normal to the edges.[31] This results in faster retraction rate at corners than along the edges and transforms the shape of the hole from square or rectangular to polygonal. This sequential process is shown in **Figure 2.7**.
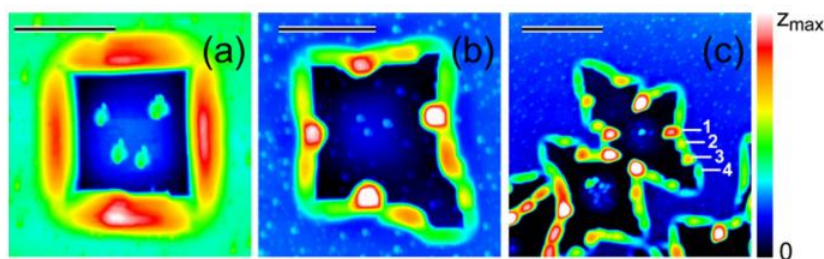
Figure 2.7: Sequence of AFM images documenting the different stages of the evolution of the surface of an SOI sample annealed at 800 °C. (a) Initial stage: square window with thickened rims. Scale bar: 0.5 μm. (b) Formation of faceted Si aggregates at the center of the rims. Scale bar: 1.0 μm. (c) Branching and coalescence of the openings, and hierarchy of Si aggregates. Scale bar: 2.0 μm.[48]
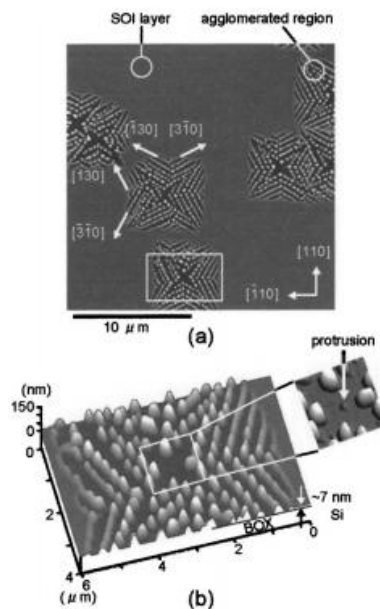
Figure 2.8: (a) Typical AFM image taken on a partially agglomerated 7-nm-thick (001) SOI layer (unpatterned) and (b) magnified image taken on the region surrounded by the white line in (a).[47]

The thickened rims may separate from the film through pinch-off process and form spheres due to Rayleigh instability. Locally thinner regions could also form along the edge resulting in fingering morphology due to faster material diffusion from these regions, as shown in **Figure 2.8**.

2.2.3 Interconnected Islands and Island Formation

The detached ridge forms a cylindrical strand with radius scaling with film thickness[31], as illustrated in **Figure 2.4d**. Many cylindrical strands will form during the dewetting process creating interconnected islands. This strand is subject to Rayleigh instability[51] and is unstable to any perturbation of wavelength greater than $2\pi r_c$ where r_c is the radius of the cylinder. The strand will then disintegrate into islands to minimize surface to volume ratio. The morphology evolution during the dewetting process can be seen in **Figure 2.9**.
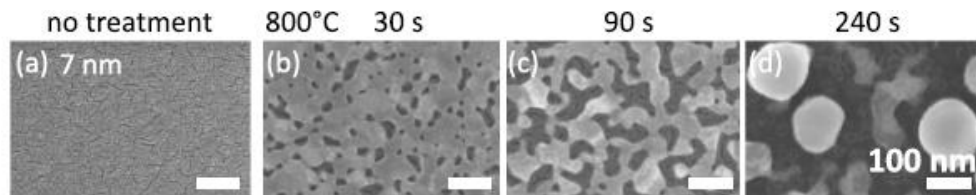
Figure 2.9: Morphology evolution of 7 nm Platinum thin film during annealing at 800 °C: (a) before annealing, (b) hole formation, (c) interconnected islands, (d) isolated islands.[32]

Jiran and Thompson[43] observed that in patterned polycrystalline Au strips, the rims fragmented into fingers as well. **Figure 2.10** shows the transformation of the Au strips into islands through fingering instability. As illustrated in **Figure 2.4**, the retracting edge is thicker than the rest of the film. However, Jiran and Thompson observed that the material accumulation at the

rim is not evenly distributed. The thinner area will retract faster than the thicker area resulting in finger-like structure. The fingering process is shown schematically in **Figure 2.11**. The resulting fingers will then disintegrate further into islands as a consequence of Rayleigh instability.
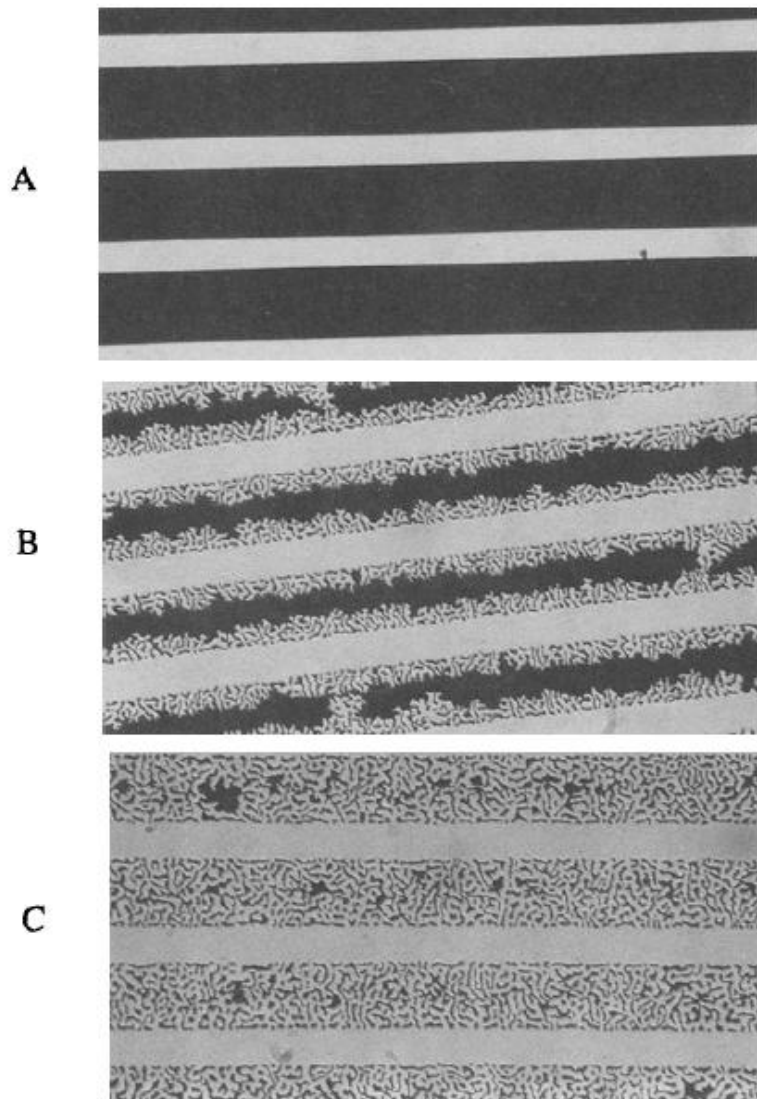
Figure 2.10: The Au strips transformation (a) before annealing, (b) partially agglomerated, and (c) fully agglomerated. Dark area shows Au.[43]
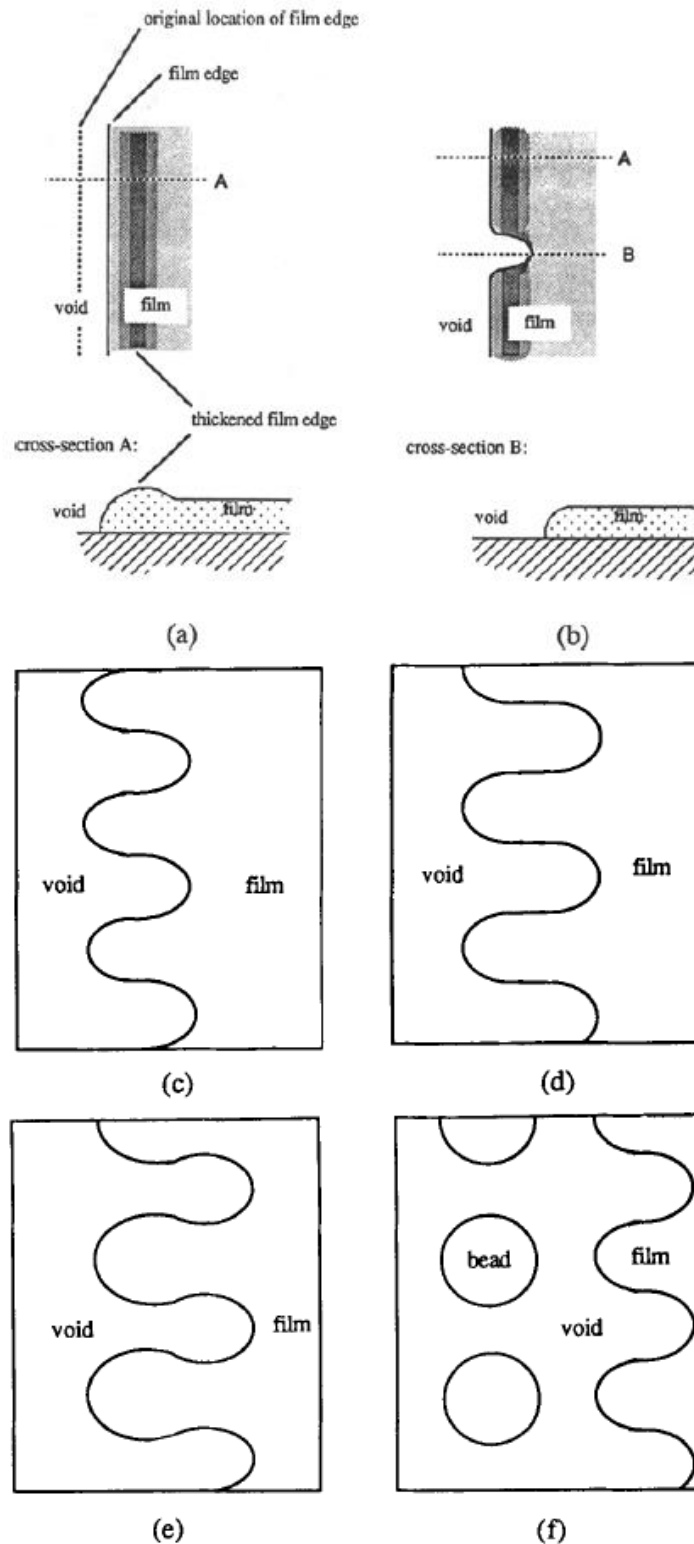
Figure 2.11: Schematic diagram of rim instability. (a) The rim thickens as it recedes and slows down. (b) Perturbation develops in the rim, the thinner part retracts faster than the rest. (c) A series of perturbations in the rim. (d) A series of fingers that form. (e). The fingers lower their surface area by rounding off and thickening. (f). The fingers detach into a series of beads.[43]

2.2.4 Coarsening

After extended annealing, coarsening might occur in which the particle size increases and particle density reduces. **Figure 2.12** shows coarsening process of thin Ni film after vacuum annealing at 500 °C for 2 hours. The coarsening process generally occur via two different mechanisms, Ostwald ripening and Smoluchowski ripening.[33] The two mechanisms are illustrated in **Figure 2.13**.

(a)	(b)
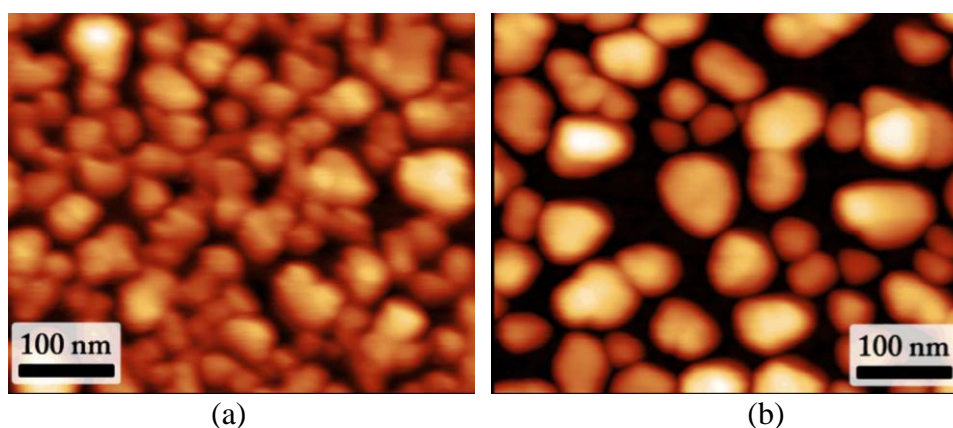
Figure 2.12: AFM micrographs of a 4.0 nm thick Ni films during different stages of dewetting: (a) before and (b) after coarsening.[33]

In Smoluchowski ripening, the whole islands migrate on the surface and collide with each other resulting in coalescence. This requires sufficiently high adatoms mobility. Smaller islands generally have higher mobility than larger islands.[52]

In Ostwald ripening, larger particles grow in the expense of shrinking the smaller particles. Large particles, which have lower surface to volume ratio, are energetically more stable. Meanwhile, adatoms on the surface of the smaller particles tend to diffuse to the environment of large particles via evaporation-condensation mechanism causing the large particle to grow.[52]
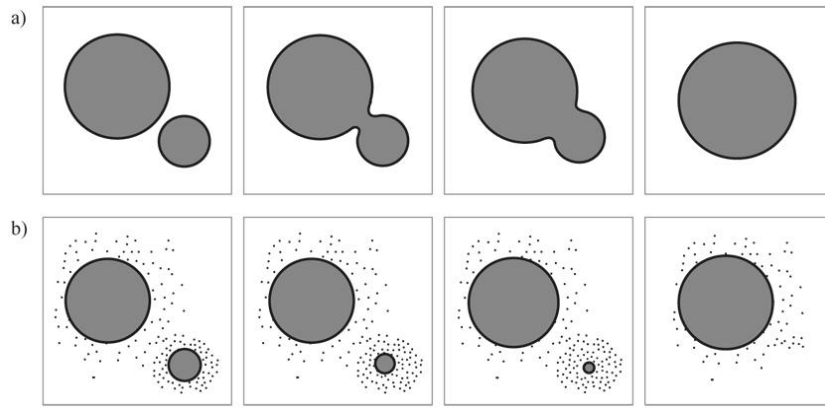
Figure 2.13: (a) Smoluchowski ripening mechanism and (b) Ostwald ripening mechanism.[53]

2.2.5 Particle Formation

After the islands coarsen, they will further evolve into energetically favored shape. The equilibrium shape of a crystal is determined by the energy minima in the Wulff plot.[54] Wulff plot shows polar representation of surface energies. An example of Wulff plot is given in **Figure 2.14**. The inner envelope of all Wulff planes determines the equilibrium shape of the crystal. Particle with anisotropic surface energy will exhibit strong faceting while the particle with isotropic surface energy will exhibit more spherical shape.
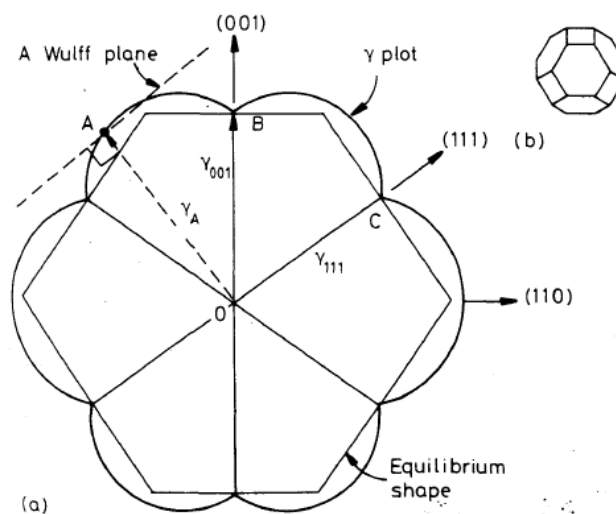
Figure 2.14: (a) An example of a Wulff plot of an fcc crystal. (b) The equilibrium shape in three dimensions.[54]

The Wulff construction, however, only applies for free-standing particles. For particles in contact with a substrate, one most consider a modified Wulff construction, familiarly known as a Winterbottom construction. In this approach, two additional vectors are factored in into the equilibrium shape construction, namely the particle-substrate interfacial energy (γ_{SP}) and the surface energy of the substrate (γ_{SV}), as shown in **Figure 2.15**. Adhesive interaction between particle and substrate is therefore expected to play a role. The inner envelope (the rectangular shape in **Figure 2.15**) represents the equilibrium shape of the particle. **Figure 2.16** shows faceted Au particles and more spherical Co particles after dewetting.
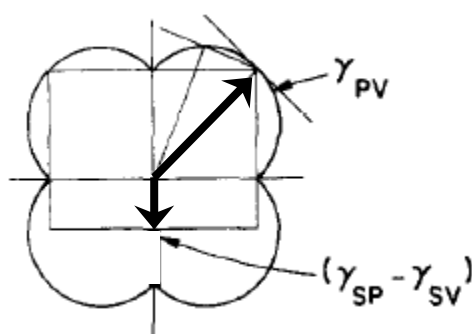
Figure 2.15: Winterbottom plot for a 2D solid with cubic symmetry.[55] γ_{PV} is the surface energy of the particle, γ_{SP} is the particle-substrate interfacial energy, and γ_{SV} is the surface energy of the substrate.

| (a) | (b) |
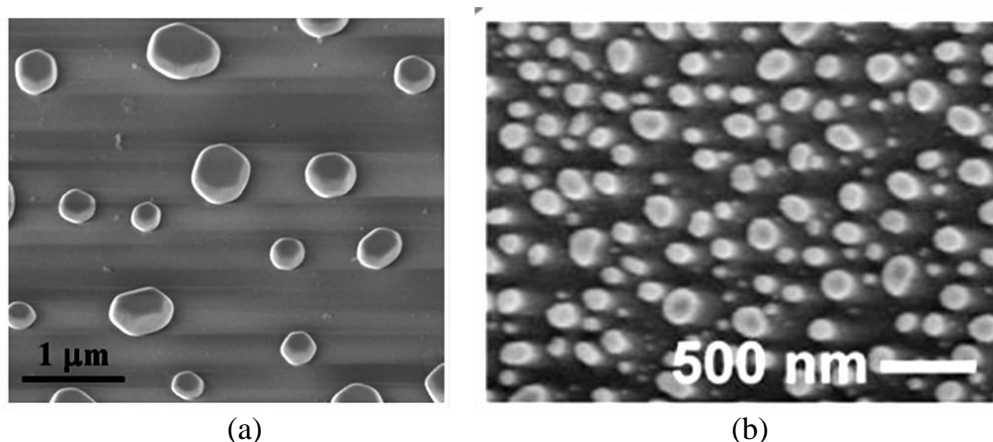
Figure 2.16: (a) Faceted Au nanoparticles annealed at 950 °C for 10 minutes.[56] (b) Spherical Co nanoparticles annealed at 850 °C for 2 hours.[29]

The size and interparticle distance of the dewetted particles depend on the initial film thickness. It is found that average particle diameter and interparticle distance increase linearly as a function of initial film thickness, as shown in **Figure 2.17**. However, not much is known on the effect of different material on the resulting particles size and interparticle distance.

(a)   (b)
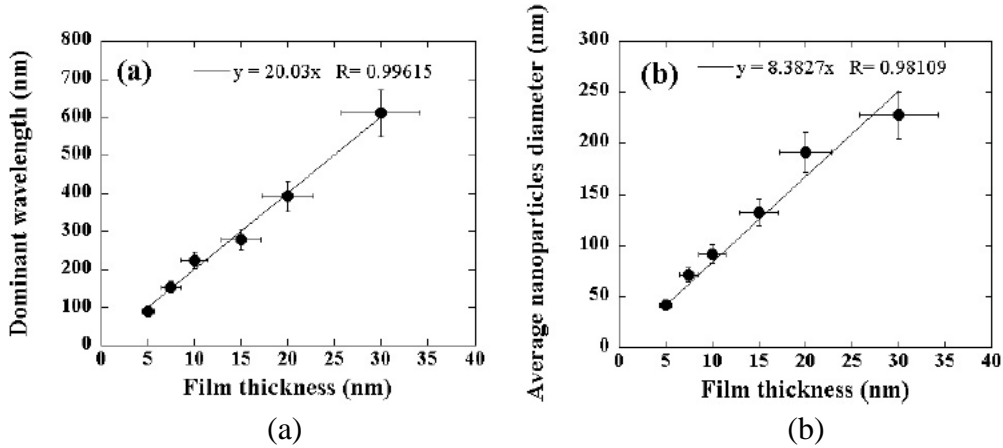
Figure 2.17: (a) Interparticle spacing and (b) average diameter of Au nanoparticles as a function of initial film thickness.[57]

2.2.6 Dewetting Rate

The rate of dewetting is affected by each process from hole nucleation to edge retraction, rim pinch-off, and fingering instability. **Table 2.1** shows the rate for the different processes.

Table 2.1: Rate for different processes in dewetting.

Process	Rate	Reference
Hole nucleation	$t_{hole\ nucleation} \propto h^4 D_s^{-1}$	[39]
Edge retraction	$\dot{r} \propto D_s^{\frac{2}{5}}(ht)^{-\frac{3}{5}}$	[44]
Rayleigh instability	$t_{Rayleigh} \propto \dfrac{r_c^4}{D_s}$	[31,58]

The overall dewetting rate can be described using Johnson-Mehl-Avrami (JMA) analysis[36,59]. In this analysis, the rates of various processes

during dewetting are incorporated in the rate of transformation of the total film area. The fraction of the area transformed is,

$$X_{dewet} = 1 - exp[N_h \pi \dot{r}^2 (t - \tau)^2]$$

Equation 2.12

where N_h is the number of holes per unit area, $\dot{r}$ is the growth rate of the hole, and τ is the incubation time. **Figure 2.18** shows the predicted result of this analysis.
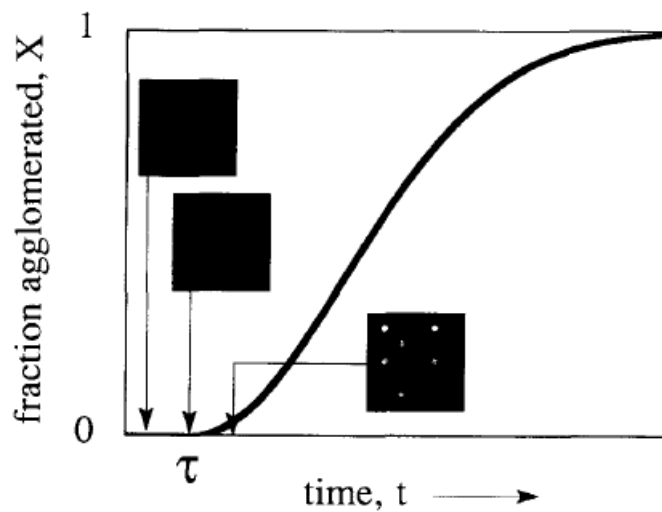
Figure 2.18: Theoretical prediction for the area fraction X agglomerated as a function of time, according to Johnson-Mehl-Avrami analysis.[59]

By fitting the experimental data, activation energy for void initiation and void growth can be extracted. Muller and Spolenak found that the activation energy for void initiation in Au film increases with film thickness, as shown in **Figure 2.19a**. Jiran and Thompson compared void growth rates of Au thin film in O_2 and Ar environment and found similar activation energy of 1.2eV, as shown in **Figure 2.19b**.
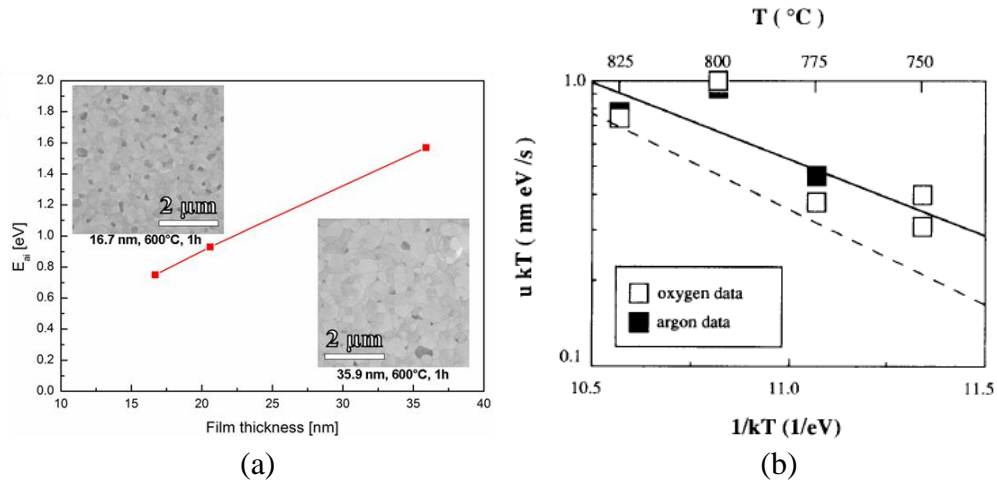
Figure 2.19: (a) Activation energy for void initiation for various Au film thicknesses.[36] (b) Activation energy for void growth for 60-nm Au film.[59]

2.3 Templated Dewetting

In order to fabricate a regular array of nanoparticles, we may template the dewetting process by either utilizing topographical template or patterning the film.

2.3.1 Topographical Template

On a flat substrate, a thin film dewetted into particles of various size and spacing distribution. Introducing a topographical feature on the substrate creates an interaction with the dewetted particles such that more ordered array of nanoparticles results. One of the most commonly used templates is inverted pyramid, fabricated by a combination of interference lithography and KOH etch.[10,27]
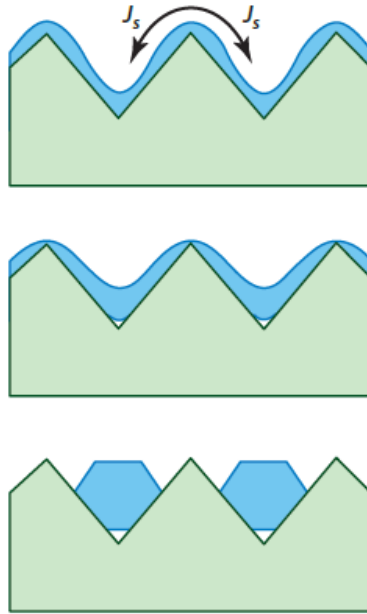
Figure 2.20: Schematic cross-sectional view of a film dewetting on a surface patterned with pits. J_s is the curvature-driven atomic flux on the surface.[31]

Conformally deposited film will share the topographical feature of the template, as shown in **Figure 2.20**. As the film is heated, top surface of the film will experience curvature-driven surface self-diffusion. This resulted in a mass flow into the pits to form ordered array of nanoparticles. In general, critical dimensions of the template and film, i.e. pit depth, mesa width, period, and film thickness, must be satisfied to achieve perfect ordering. **Figure 2.21** shows how different set of parameters significantly affect the degree of achievable ordering. For shallow pit and wide mesa, particles form both on the pit and the mesa (**Figure 2.21b**). When the film is too thin, multiple particles form in the pit (**Figure 2.21c**). Conversely, when the film is too thick, there is no interaction with the topography (**Figure 2.21d**). Only when the template dimensions and film thickness are matched, one particle per pit results, as shown in **Figure 2.21a**.
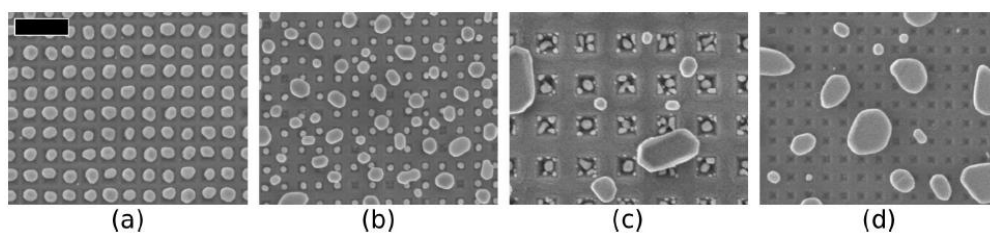
Figure 2.21: Four categories of dewetting on topography. (a) Ordered arrays of one particle per pit with no extraneous particles. (b) Ordered arrays of one particle per pit with particles on mesas. (c) Multiple particles form per pit with no ordering. (d) Film not interacting with topography. Scale bar is 500 μm.[27]

Giermann and Thompson[27] also discovered that the Au particles within pits were crystallographically aligned with (100) texture and uniform in-plane orientation. Oh *et al.*[29] utilized the same template to fabricate one Co nanoparticles per pit. While this is achievable, the Co particles were found not to have crystallographic alignment.

Besides inverted pyramid template, other topographical templates such as ripple patterned substrate,[30] line grooves[60-62] and grid grooves can also be used.[60] On the substrate with grid grooves patterned,[60] at the edge of a groove we will have a positive excess chemical potential and a negative excess chemical potential in the valley. Thus, to reduce the local energy, the material at the edges will flow to the flat area between the grooves and the valleys of grooves during the dewetting process and the particle size is limited due to the high positive excess potential at the both edges of a groove. The particles with diameter larger than the grooves width disappear at deeper grooves since deeper groove has a higher local curvature and thus a higher barrier for the mass flow. Moreover, film thinning at the edge of a groove is expected and film discontinuity could appear at the edge with increased groove depth. The almost one particle with similar size in one square unit is obtained because the

diffusion of material is limited inside of the square (**Figure 2.22a**). The resulting particles have bimodal distribution, representing segregation of the particles on the square mesas from the particles in the pit (**Figure 2.22b**).
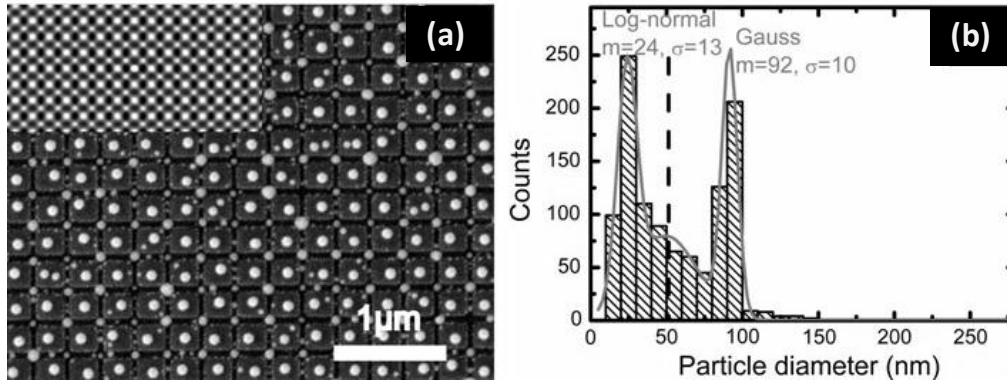
Figure 2.22: (a) SEM image of Au nanoparticles formed after annealing of 10 nm Au film at 900 ℃ in N_2 ambient on the grid grooves substrate. (b) Histograms of the mean particle diameter showing bimodal distribution.[60]

2.3.2 Patterned Film

Patterned thin films showed different dewetting behavior depending on their width, length, and initial film thicknesses. Kim *et al.*[28] showed that in contrast to the dewetted continuous film that forms islands with irregular size and spacings, the films patterned into rectangles can develop into ordered particles, e.g. a single particle, single rows of particle or double rows of particles (**Figure 2.23**). The tendency to form ordered particles decreases with increasing pattern dimension, in either length or width.

Thus, although dewetting of a blanket thin film generally resulted in particles with range of size and spacings, it is possible to combine the dewetting technique with lithography either by patterning the substrate or the film to form ordered arrays of nanoparticles. Ordered array of nanoparticles are generally required for various applications. It is also possible to engineer

the size and location of the particles by adjusting several parameters such as initial film thickness, size of patterned film or spacing of the topographical templates.
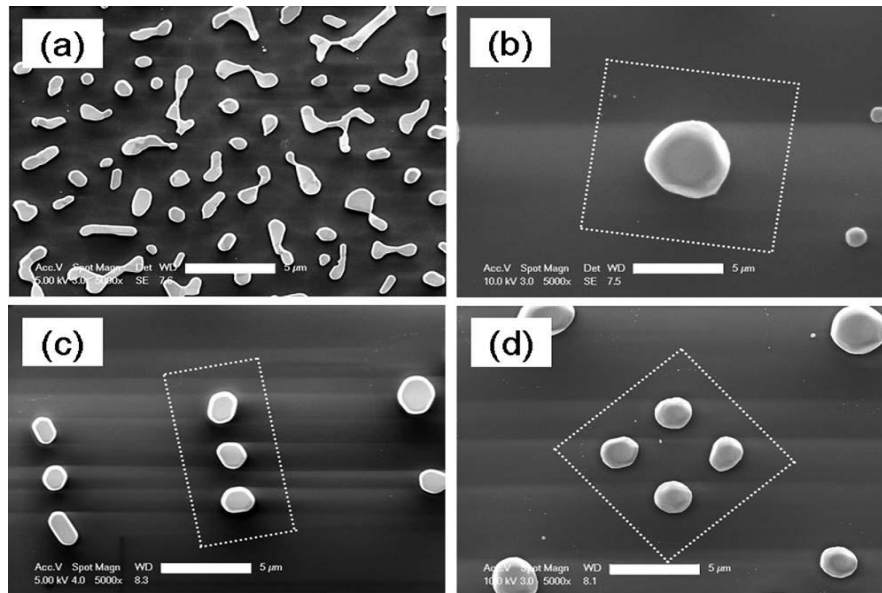
Figure 2.23: (a) A continuous film dewets into islands/particles with broadly distributed sizes and spacings. The film thickness is 30 nm. (b) A single Au particle developed when an 11 μm x 11 μm x 240 nm square pattern dewet. (c) A single row of three particles developed when a 4 μm x 11 μm x 60 nm rectangular pattern dewet. (d) Double rows of two particles developed when a 9.3 μm x 9.3 μm x 120 nm square pattern dewet. Scale bars = 5 μm.[28]

2.4 Dewetting of Alloy

In this section, study on solid-state dewetting of miscible and immiscible alloy will be discussed.

2.4.1 Miscible System

Miscible system is a system where the constituent materials are mutually soluble in each other due to similar crystal structure, atomic radii, electronegativity, and valence.[63] The effect of alloying has interesting effect

on the alloy material properties, but there have been limited studies on miscible alloy systems.

Oh et al.[18] investigated annealing behavior of CoPt bilayer thin film with compositions 52% Pt (CP52) and 36% Pt (CP36). This work focuses more on creating ordered array of nanoparticles and exploring possible magnetic application. Oh et al. utilized topographical (inverted pyramid) template to obtain particles with more uniform size and interparticle distance. Templating also help to produce more uniform composition as the Co and Pt layers rupturing at the same locations due to topographical template. The dewetted particles are mainly single crystal although some twin boundaries are observed. As predicted, CP36 produced magnetically soft fcc phase particles while CP52 produced magnetically hard $L1_0$ fct phase. For magnetic application, it is desired that the $L1_0$ fct particles have easy axis [001] perpendicular to the substrate plane but the majority of the observed particle have easy axis [110], [001] and [112] oriented normal to the substrate. It was found that annealing at 900 ℃ resulted in the highest frequency of [001] perpendicular easy axis with the array having in-plane coercivity of 10 kOe and out-of-plane coercivity of 14 kOe.

Another study by Muller and Spolenak[36] focuses more on the dewetting mechanism, for which they selected Au and AuPt alloy systems. Morphology maps were created for both materials. It is found that alloying influences the dewetting behavior at 500 ℃, as higher Pt content showed delayed dewetting, but not at higher temperatures (700 – 900 ℃). They distinguished three zones in the morphology map, namely continuous film, partial dewetting, and complete dewetting. They utilized JMA analysis (**Equation 2.12**), which was

previously used by Jiran and Thompson[59], to determine the activation energies for void initiation and void growth. They successfully extracted the relevant activation energies for Au dewetting process. However, they found that there is non-linearity behavior in the Arrhenius plot for AuPt alloy with increasing Pt content, as shown in **Figure 2.24**. They argued that Pt content only affects one of the several processes that are active during the dewetting process, such as surface diffusion and grain-boundary diffusion. More data points might be needed to justify whether non-linearity behavior really exists in the alloy dewetting. It might be important to compare the alloy dewetting behavior to Pt film as well.
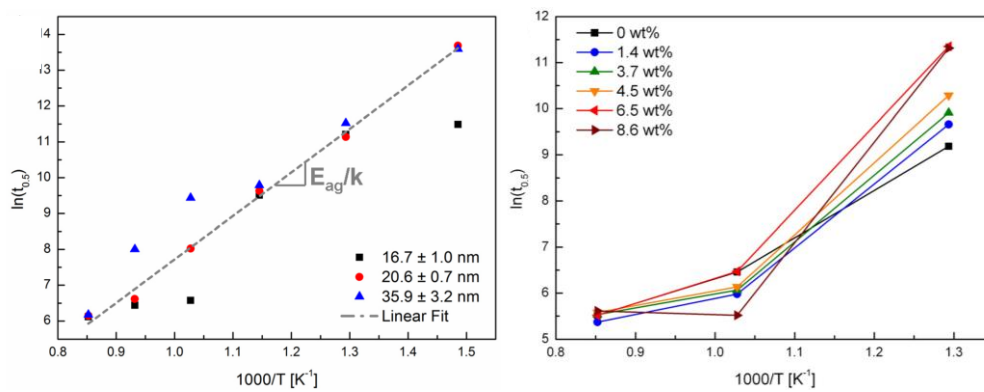
Figure 2.24: (a) Arrhenius plot for pure Au of three different initial film thicknesses. (b) Arrhenius plot for 20-nm-thick AuPt alloys of various Pt contents.[36]

Recently, Haniff et al.[64] studied the morphologies and properties of thin film CoFe (4-10 nm) on oxidized Si when they were heat-treated under H_2 plasma at 700 °C for 10-60 minutes. They also studied Co and Fe thin film as comparisons. They found that particle size increases with increasing film thickness and plasma treatment duration. In comparison, Co particle size and interparticle distance are larger than the rest of the materials under study. However, the definition of particle is loosely defined, by including also the

stage where the islands are still not in their equilibrium shape or irregular. It was found that for elemental materials (Co and Fe), resistivity increases with film thickness due to increasing particle distance. Interestingly, however, the resistivity trend for alloy shows a maximum for film thickness of ~ 8 nm. This behavior is attributed to the increased surface contact area between nanoparticles owing to coalescence for the case of film thickness larger than 8 nm. On the other hand, it was found that magnetoresistance decreases with film thickness, irrespective of the materials, due to increasing particle size and distance. For the alloy, magnetoresistance increases with increasing Fe content.

Wang and Schaff recently explored to Au-Ag system to fabricate nanoporous Au nanoparticles[65]. Bilayer Au-Ag was annealed and, after cooling down to room temperature, the Ag component was selectively removed resulting in nanoporous structure that possess high surface-to-volume ratio. This nanoporous structure may find its usefulness in various applications, such as photonic, catalytic, and chemical. Recently, they have successfully created an ordered array of these nanoparticles using inverted pyramid template, as can be seen in **Figure 2.25**.[66]
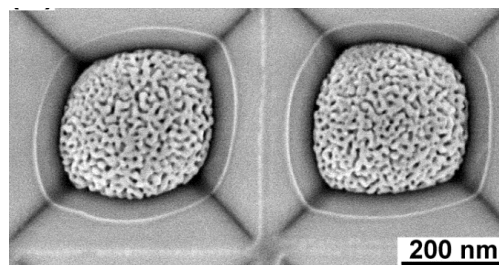
Figure 2.25: Nanoporous Au nanoparticles.[66]

2.4.2 Immiscible System

In this section, solid-state dewetting studies on immiscible system will be reviewed. In a pioneering work on NiAg system by Petersen and Mayr[30], it was found that the addition of Ag transforms the dewetting mode from capillary-driven for Ni (**Figure 2.26a**) to fractal-like growth (**Figure 2.26b**). It was argued that Ag segregates to surface, acting as a catalyst for the fractal formation by creating local tensile stress. To relieve the stress, the void will grow along high-energy grain boundaries in a branch-like fashion.

The assumption that solute segregation creates a stress concentration leading to fractal growth, however, disagrees with the observation from Jiran and Thompson[43]. In their studies, pure Au film, i.e. no solute, also exhibits fractal growth and this phenomenon is rather attributed to the local variation in the edge retraction rate due to thickening rim instability. Following this argument, the findings from Petersen and Mayr[30] may therefore be explained in that the addition of Ag increases the local edge retraction variation of the receding film, as compared to pure Ni film, resulting in different dewetting mechanism between NiAg and Ni.
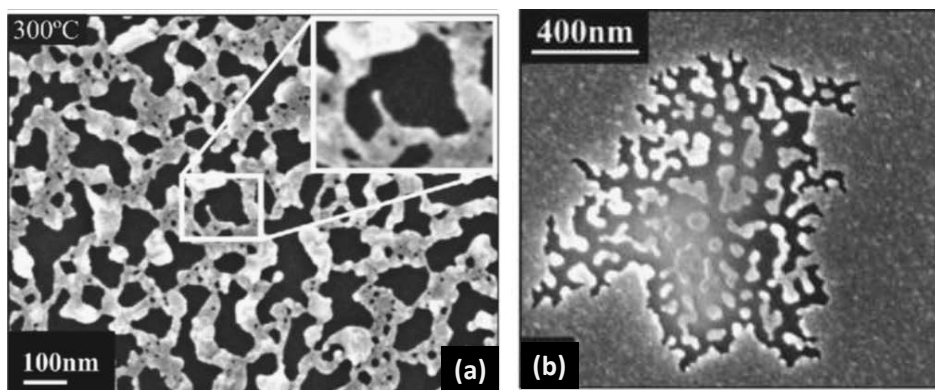
Figure 2.26: (a) Ni film and (b) NiAg film after *in situ* annealing at 300 ℃ for 1 hour.[30]
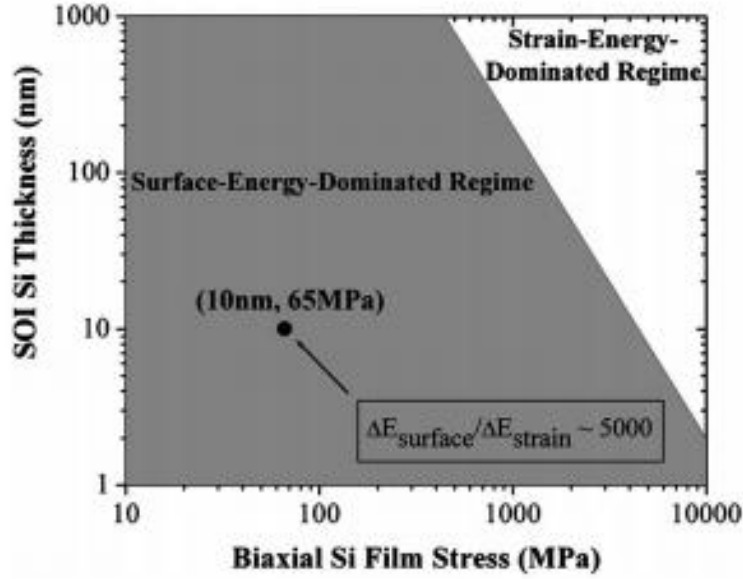
Figure 2.27: Plot indicating regimes of SOI thickness and biaxial Si film stress where surface energy reduction (shaded) and strain energy reduction (unshaded) would dominate during agglomeration. The SOI films that have been observed to undergo agglomeration (h_{Si} < 30 nm and σ_{Si} < 100 MPa) can be seen to lie within the surface-energy-dominated regime, strongly indicating that SOI agglomeration is a surface-energy-driven phenomenon.[49]

Danielson *et al.*[49] demonstrated that surface energy is the primary driving force in dewetting. They calculated the changes in surface energy and strain energy during agglomeration of an initially flat biaxially stressed square-shaped SOI film. Assuming the Si islands to be hemispherical and that the island radius scales with the SOI thickness (taken to be equal to 20 of silicon-on-insulator/SOI thickness), as well as volume is conserved during dewetting, they obtained,

$$\Delta E_{surface} = -\frac{\pi}{3} h_{Si}^2 [13600\gamma_{Si-vac} - 14800(\gamma_{SiO2-vac} - \gamma_{Si-SiO2})]$$

Equation 2.13

$$\Delta E_{strain} = -\frac{\pi}{3} h_{Si}^3 \left[16000 \frac{(1 - \upsilon_{Si})\sigma_{Si}^2}{E_{Si}}\right]$$

Equation 2.14

where γ is the surface energy, σ_{Si} is the biaxial stress of Si, υ_{Si} is the Poisson ratio, E_{Si} is the elastic modulus of Si, and h_{Si} is the initial Si thickness. From **Figure 2.27**, it can be seen that the surface energy reduction in the agglomeration process for SOI (biaxial stress < 100 MPa) is far greater than the strain energy reduction. Metal thin films have been found to have relatively low biaxial stress at high temperature. It has been established that the film stress at 400 ℃ for Al and Cu is well below 100 MPa, even for thicknesses above 1 μm.[67-69]

Immiscibility between materials can also be utilized to fabricate interesting nanostructures. Wang and Schaaf[70] demonstrated the fabrication of NiAu nanoalloy particles from Ni-Au bilayer of 1:1 volume ratio. After annealing, Ni-rich and Au-rich phases are clearly separated, as shown in **Figure 2.28**.

EDX linescans further reveal that the Ni-rich phase has higher matrix content (10:1) as compared to the Au-rich portion (3:1). This is in agreement with the skewed solubility gap profile exhibited by Ni-Au phase diagram[71], i.e. Au solid solubility limit is less than that of Ni. Wang and Schaaf also found that the shape of particles depend on the annealing temperature, in that higher annealing temperature resulted in more spherical particles.
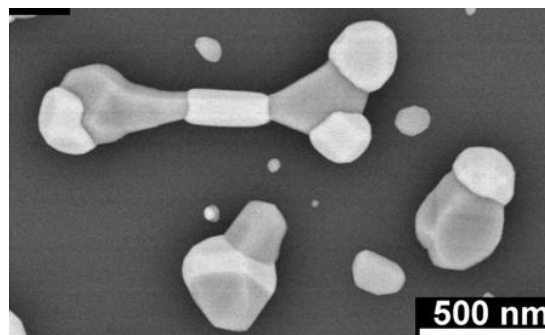
Figure 2.28: Ni-Au nanoalloy particles.[70]

Amram *et al.*[72] investigated the precipitation of Fe phase from Au-Fe system and developed a thermodynamic model to explain the kinetics and morphology of the Fe precipitate. The Au-Fe layer was annealed at 600 ° and 900 ℃ in Ar + 10% H_2 ambient. At 600 ℃, two phases are in equilibrium, namely fcc Au and bcc α-Fe, while at 900 ℃, only fcc Au is in equilibrium. Based on the model, they predicted core-shell configuration, where Fe precipitate is embedded inside the parent Au-rich. However, experimental results show that the core-shell configuration is satisfied only up to a critical thickness, above which the particle adopts partially embedded Fe-precipitate configuration. For even thicker film, the Fe precipitate will be at the same height as the parent Au-rich. Thus, for the same composition of alloy, one can achieve different morphology depending on the initial film thickness.

From the literature review above, it can be seen that alloy nanoparticles can be created by a simple dewetting method. They have interesting properties and can be utilized to create various structures. The study of alloy dewetting is still limited, but there have been some works on the dewetting morphologies and dewetting rate of miscible system and the process of precipitation in immiscible alloy dewetting.

2.5 Summary

Solid-state dewetting of elemental materials has been extensively studied and much understanding has been obtained from the initial stage of hole initiation to particle coarsening. Templated dewetting has also been studied to produce regular array of nanostructures. However, the influence of different materials and alloy addition on the dewetting process has not been much

explored. A few studies have been carried out to investigate the dewetting morphology, rate, and possible applications. Since alloy offers interesting properties which might be useful in various applications such as magnetism, optics, or nanofabrication, a more comprehensive study of alloy dewetting, both miscible and immiscible systems should be conducted.

Chapter 3. Experimental Methods

3.1 Introduction

This chapter presents detailed experimental methods used in this study. **Section 3.2** describes the sample preparation procedures which involve sample cleaning and growth or deposition of diffusion barrier. **Sections 3.3** and **3.4** discuss the metal thin film deposition and the subsequent annealing process. **Section 3.5** presents the lithography process to pattern the samples. Finally, **Sections 3.6**, **3.7**, and **3.8** describe microstructural analysis techniques which include scanning electron microscopy (SEM), transmission electron microscopy (TEM), and energy dispersive x-ray spectroscopy (EDX).

3.2 Sample Preparation

The Si wafer preparation procedure consists of wafer dicing, sample cleaning, and growth or deposition of diffusion barrier. First, p-type Si wafers of (100) orientation were coated with resist, to protect the wafers from debris during dicing, and were diced into a size of 0.5 cm $\times$ 0.5 cm. The samples were then immersed in acetone for 30 minutes to remove the resist. Afterwards, they were immersed in isopropanol for 5 minutes and rinsed in flowing de-ionized (DI) water with bubbler. The samples were then blown dry with N_2 gun and are ready for the next processing step.

The next step is to grow or deposit a layer of oxide that acts as a diffusion barrier between the metal and the Si. Two types of diffusion barriers were used in this work, silicon oxide (SiO_2) and aluminum oxide (Al_2O_3).

SiO$_2$ layer is a good diffusion barrier for most metals. However, in forming gas ambient at high temperature (higher than 450 – 500 ℃), Pd can reduce SiO$_2$ to Si and forms palladium silicide[73]. Therefore, for most cases, Al$_2$O$_3$ is used as a diffusion barrier.
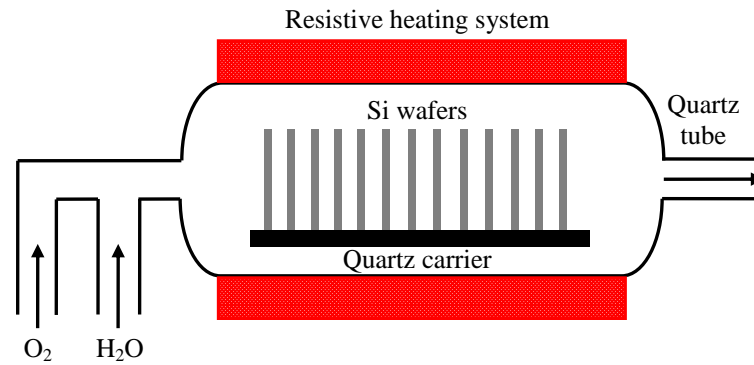
Figure 3.1: Schematic of a Si oxidation system.

The SiO$_2$ layer was grown by thermal oxidation process using Tystar Model Mini Tytan oxidation system. The oxidation system is schematically illustrated in **Figure 3.1**. In this work, thin oxide layer (~10 nm) was grown by dry oxidation process, while thicker oxide layer (80 nm and above) was grown by wet oxidation process. The oxidation reaction takes place at the Si/SiO2 interface according to the reaction of Si + O$_2$ → SiO$_2$ for dry oxidation and Si + 2H$_2$O → SiO$_2$ + 2H$_2$ for wet oxidation[74]. The basic oxidation process of silicon is described in **Figure 3.2**. As the oxide layer becomes thicker, the oxide growth rate will be diffusion-limited. For dry oxidation process, the diffusion-limited regime is ~4 nm while for wet oxidation process the diffusion-limited regime is ~100 nm[75]. As a consequence, wet oxidation process is typically used to grow thicker oxide layer even though dry oxidation produces a more uniform and denser thermal oxide[74].
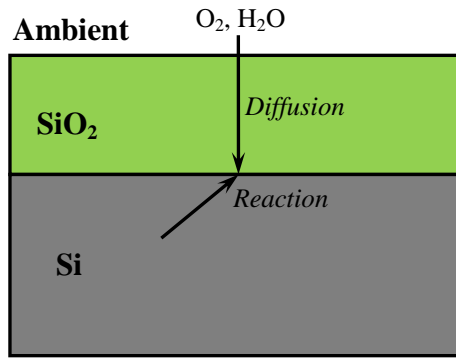
Figure 3.2: Basic oxidation process of silicon.

The Al_2O_3 layer was deposited by using Anelva L-332S-FH radio frequency (RF) sputtering system. In direct current (DC) sputtering system, an inert gas is fed into the chamber at low pressure, after which a voltage is applied across the cathode (target) and anode (sample) to create plasma. The positive ions in the plasma are accelerated to the target and sputter the target atoms which will then travel as a vapor and deposit on the surface of the sample. Problem arises when the target is an insulating material because when the negative DC voltage is applied, positive charge (Ar^+) from the plasma will build up on the negatively charged insulator and the negative surface voltage will not be sufficient to sustain the plasma[74]. Thus, high frequency, commonly 13.56 MHz, alternating potential is used to maintain continuous plasma discharge. The target area is made smaller than the anode to ensure the voltage drop at the target is much greater than the voltage drop at the anode, so that the sputtering occurs almost entirely at the target surface. The RF sputtering system is depicted schematically in **Figure 3.3**. The Al_2O_3 layer was deposited at a deposition rate of 1 nm/min with a base pressure of $\sim 1 \times 10^{-6}$ Torr.
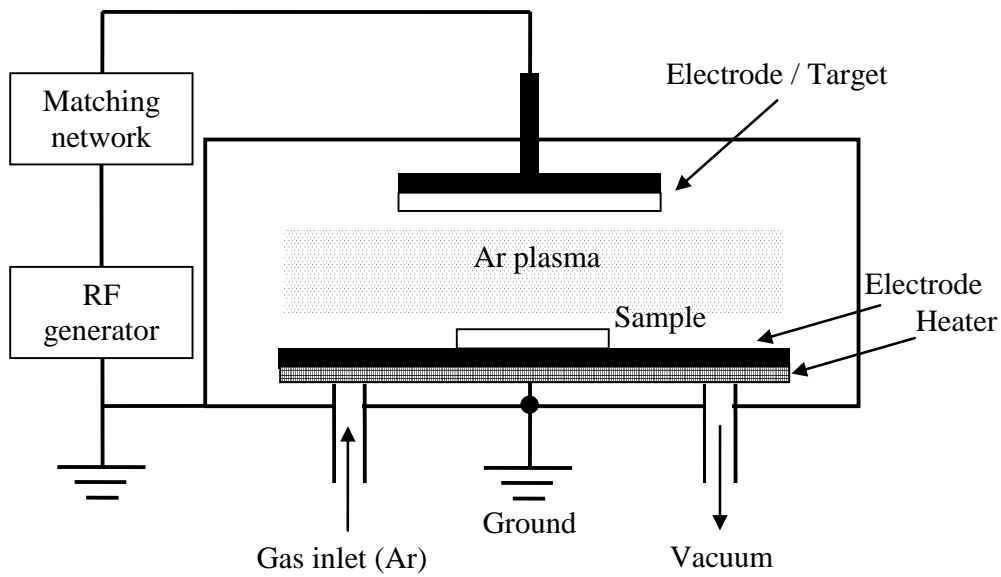
Figure 3.3: Schematic diagram of RF sputterer.

3.3   Metal Film Deposition

In magnetron sputtering, a magnetic field is applied around the target to increase the efficiency of Ar atoms ionization. A permanent magnet structure is placed behind the target and the resulting magnetic field will act as an electron trap, causing the electron to move in a spiral motion by Lorentz force and increasing the probability of collisions with Ar atoms. Thus, more Ar^+ will strike the target and deposition rate will increase accordingly. In addition, a lower Ar pressure can be used and the resulting metal film quality will improve due to less Ar incorporation in the film[74]. All the metal films in this work were deposited by AJA ATC 2200-V magnetron sputtering with a base pressure of 5×10^{-8} Torr.

3.4 Furnace Annealing

The annealing process was performed in a three-zone furnace at atmospheric pressure. The schematic drawing of a horizontal furnace used in this work is provided in **Figure 3.4**. The evolution of the metal film during the annealing process is affected by three important parameters: temperature, duration, and ambient. In this study, annealing was carried out in either N_2 ambient or forming gas (90% N_2 + 10% H_2) ambient, with temperature varies from 150 − 1050 ℃ and annealing duration of 5 minutes − 2 hours. The temperature and duration needed to reach complete dewetting also depends on the material of the film. Since the furnace cannot be evacuated, there was always some air present in the chamber. Thus, the effect of oxidation by residual oxygen present in the chamber might also influence the final morphology, especially for non-noble metals.
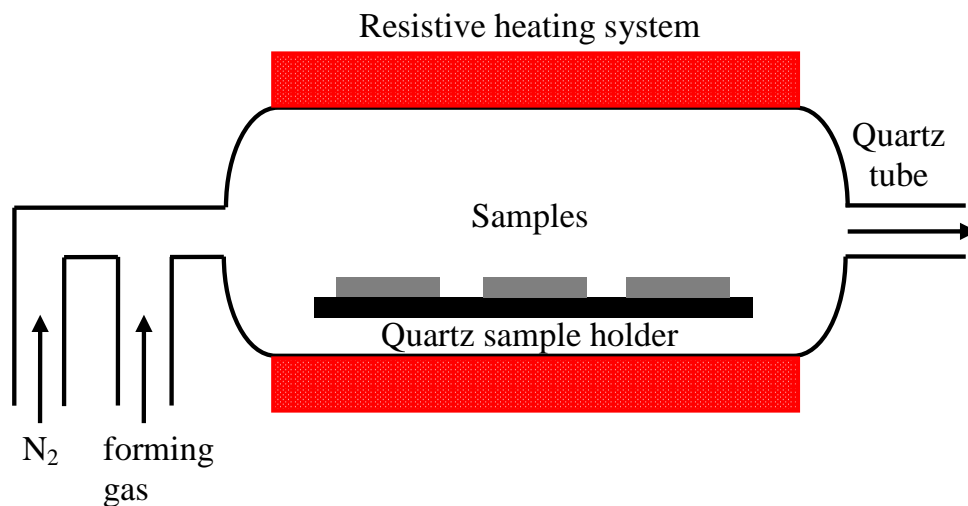
Figure 3.4: Schematic diagram of furnace annealing.

3.5 Lithography

First, the sample was coated with developable WiDE-C anti-reflection coating (ARC) via a two-step spin coating process. The sample was spun at

500 rpm for 2 seconds (acceleration of 560 rpm/sec) to ensure uniform resist coating over the entire surface of the sample, followed by spinning at 2000 rpm for 58 seconds (acceleration of 1680 rpm/sec) to get ARC layer with ~ 85 nm thickness. The sample was then baked at 165 ℃ for 2 minutes. The ARC layer was necessary to create undercut profile to help in the lift-off process of a thick film. After that, the sample was coated with Ultra-i 123 positive resist via a two-step spin coating process, 500 rpm for 2 seconds (acceleration of 560 rpm/sec) followed by 3000 rpm for 58 seconds (acceleration 1680 rpm/sec). After the resist coating, the sample was soft baked at 90 ℃ on a hotplate for 90 seconds to remove excess solvent within the photoresist and to improve the adhesion of photo resist to the sample.

Subsequently, interference lithography (IL)[76,77] with Lloyd's mirror configuration[78] and HeCd laser source (λ_{IL} = 325 nm) was used for film patterning. This method was employed as it can cover a large area within a short period of time and no mask is required. In the Lloyd's mirror configuration, the mirror is fixed perpendicularly to the substrate on a rotating frame that can be rotated to a certain angle (θ_{IL}). The incoming laser beam will interfere with the beam reflected off the mirror to form a standing wave pattern that will be recorded in the photoresist, with a spatial period (p) given by,

$$p = \frac{\lambda_{IL}}{2 \sin \theta_{IL}}$$

Equation 3.1

Figure 3.5a describes the schematic of Lloyd's mirror IL system and **Figure 3.5b** shows the interfering beams on the photoresist.

45
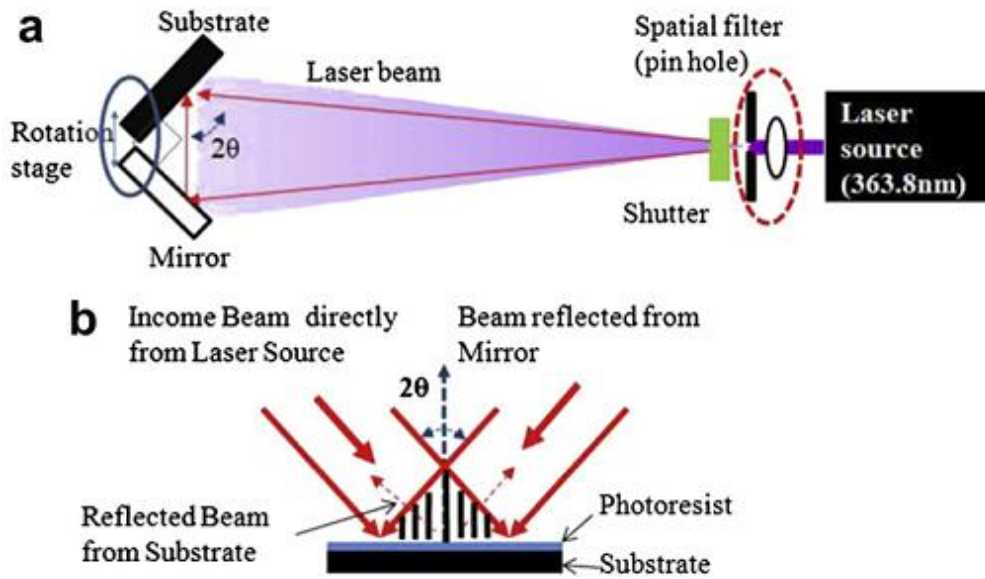
Figure 3.5: (a) Lloyd's mirror interference lithography setup, (b) interfering beams on the photoresist.[79]

After exposure, the sample was baked at 110°C on a hotplate for 90 seconds and then immersed in Microposit MF CD-26 developer for 60 seconds to produce the pattern. The sample was then rinsed with DI water and blown dry with N_2 gun.

After patterned resist was obtained and metal was deposited on the sample, lift-off was performed to remove the metal-coated resist and ARC, leaving behind the metal pattern on the substrate. To remove the resist, sample was put on the sample holder and immersed in an acetone-filled beaker which was then put in an ultrasonic bath (Branson B2510DTH). After the sample was subjected to ultrasound agitation at 40 kHz for about 10 minutes, the resist should be completely removed. To remove the ARC, similar step was performed but with Microposit MF CD-26 developer instead of acetone. The final pattern of the metal will be the negative image of the original pattern on the resist.

3.6 Scanning Electron Microscopy

Characterization of the surface morphology of the samples was carried out using scanning electron microscope (SEM) FEI Nova NanoSEM 230. In an SEM, electrons from a field-emission cathode are accelerated when voltage is applied between cathode and anode. Primary electrons (PE) that strike the sample will generate secondary electrons (SE), backscattered electrons (BSE), Auger electrons (AE) and characteristic x-ray (X). Schematic illustration of electron-sample interaction and information depth of the emitted signals are described in **Figure 3.6**.
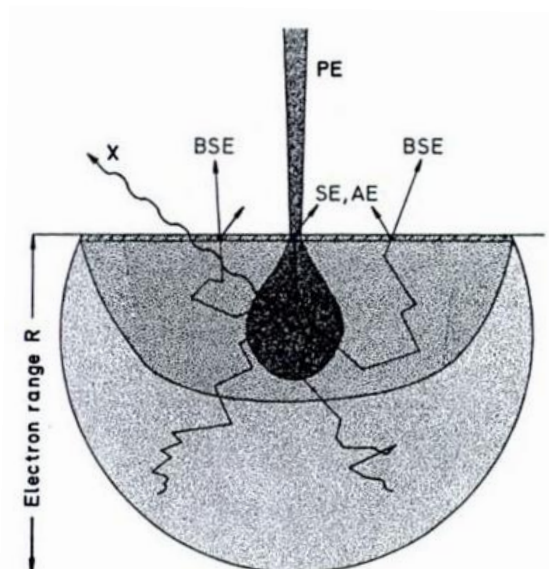
Figure 3.6: Origin and information depth of SE, BSE, AE and X for normal incidence of PE.[80]

SE and BSE are usually detected with a scintillator-photomultiplier detector. SE is resulted from inelastic scattering. As shown in **Figure 3.6**, some of the SE near the surface (within the escape depth (λ_E) of ~ 2 nm) can escape and be detected. Since λ_E is very small, SE image will give topographical information of the sample[81]. **Figure 3.7a** shows that for an inclined surface (B), the number of escaping SE per PE (SE yield) is larger

than that of a flat surface (A) as can be seen by comparing the hatched area in A and B. Thus, protrusion features will appear brighter than their surroundings. **Figure 3.7b** shows that interaction volume increases with the PE energy (E_0) due to more scatterings and decreases with the sample atomic number (Z) because the PE is being slowed down due to more atoms available per unit volume. The dependence on Z implies that materials with difference Z will also create contrast in SE image. However, to obtain stronger Z-contrast image, SEM should be operated under BSE mode.

<center>(a)   (b)</center>
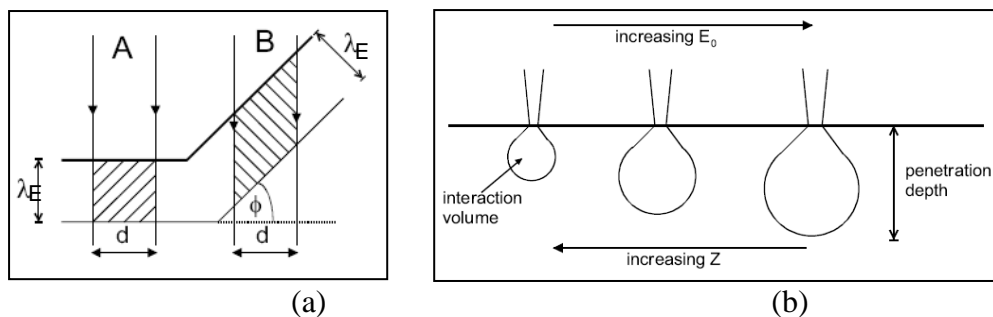
Figure 3.7: (a) SEM incident beam that is normal to a specimen surface (at A) and inclined to the surface (at B). (b) Schematic dependence of the interaction volume and penetration depth as a function of incident energy E_0 and atomic number Z of the incident (primary) electrons.[81]

BSE is a primary electron that is ejected from the sample by elastic scattering with angle greater than 90°. The BSE signal comes from up to half the penetration depth of PE, which is much larger than the escape depth of SE. The fraction of primary electrons that can escape as BSE is proportional to Z and thus materials with difference chemical composition will create contrast in BSE image.[81]

3.7   Transmission Electron Microscopy

Transmission electron microscope (TEM) is used to obtain diffraction patterns and high-magnification images, generally in the range of 10^3-10^6 of a

sample.[81] The TEM images in this work were obtained from JEOL 2010F and JEOL 3010 systems. **Figure 3.8** shows simplified schematic images of two TEM basic operations, diffraction mode and image mode. Basic component of TEM are vacuum system, high-voltage source and column, which consists of electron gun, condenser lens and apertures, specimen holder, objective lens system and objective apertures, intermediate and projector lens system, and image recording device.
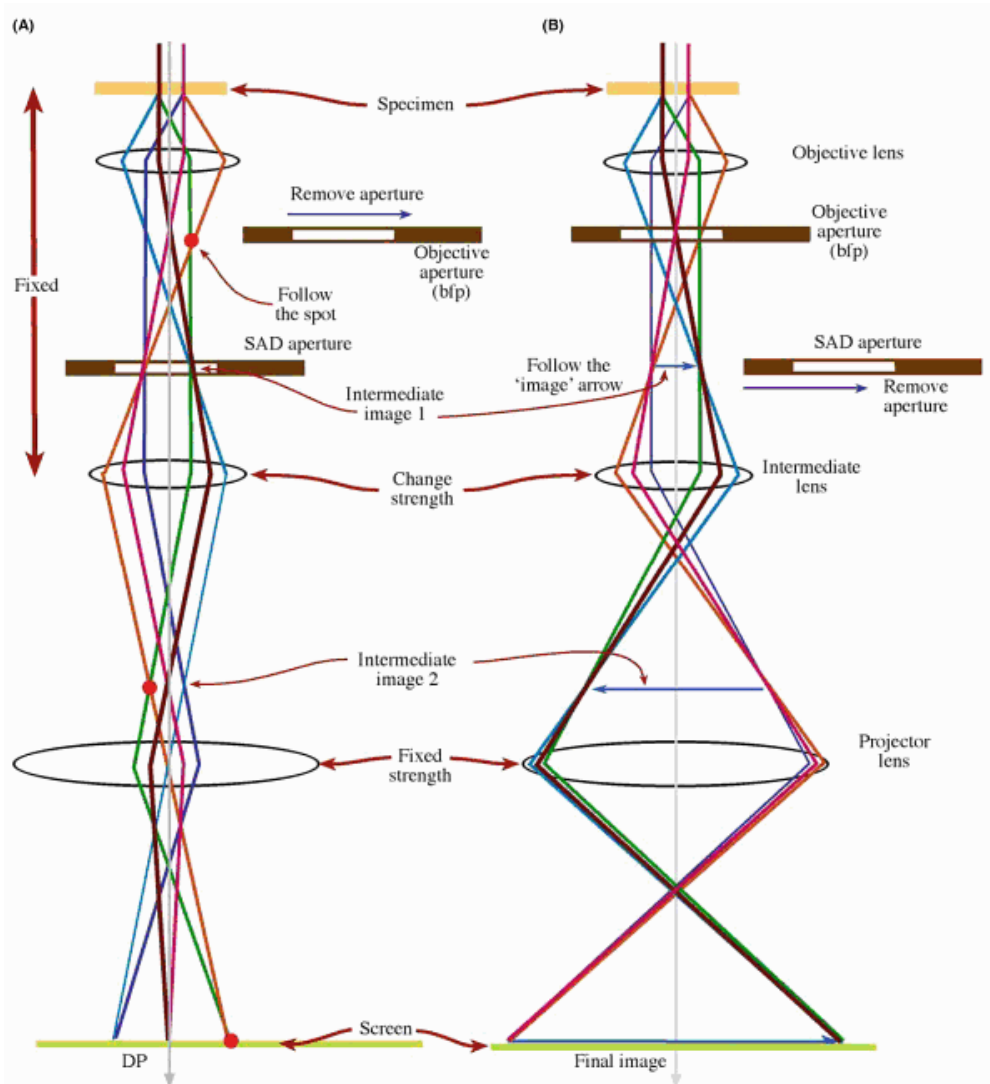
Figure 3.8: Two basic operations of TEM imaging system: (a) diffraction mode, (b) image mode.[82]

Electrons from electron gun are accelerated by the applied voltage and are gathered and focused by condenser lens systems. After passing through the specimen, the objective lens system will either diffract or scatter the electrons in the forward direction. The objective lens directly determines the resolution of the TEM. Further magnification will occur in the intermediate and projector lens systems.

In the diffraction mode, the electron beams that pass through the specimen are diffracted then passed through the objective lens. Parallel beams are focused in the back-focal plane which acts as the object plane for the intermediate lens. Selected-area diffraction aperture is inserted to select a specific area of the specimen to contribute to the diffraction pattern.
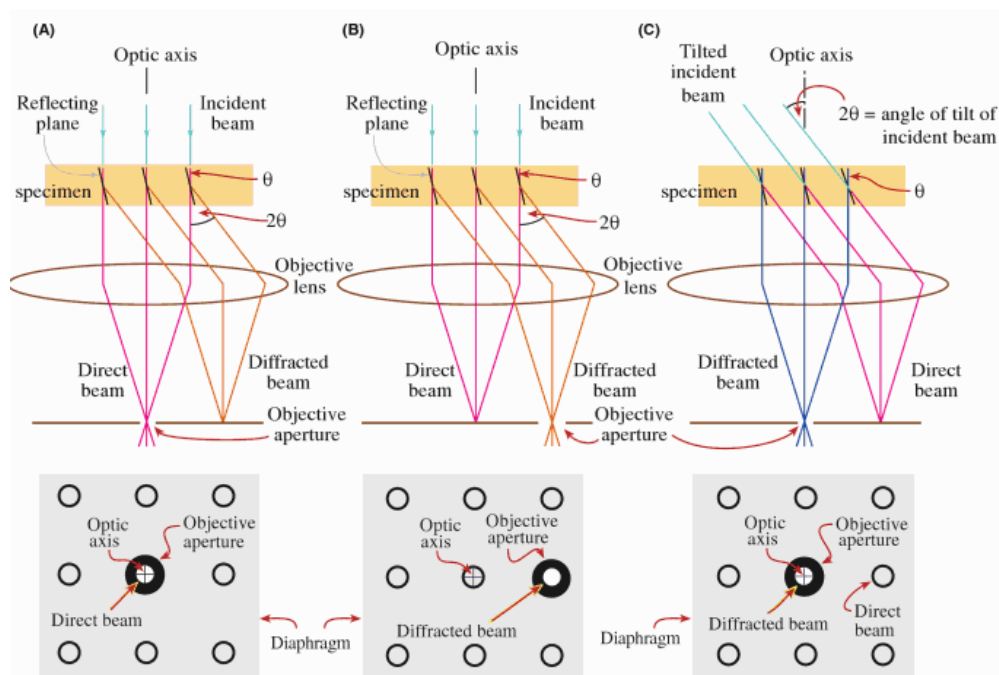
Figure 3.9: (a) Bright-field image formation from the direct electron beam, (b) displaced-aperture dark-field image formation, and (c) centered dark-field image formation.[82]

In the image mode, objective aperture is inserted and the intermediate lens is adjusted so that the image plane of the objective lens becomes the

object plane of the intermediate lens. Either direct beam or scattered beam can be selected to form bright-field and dark-field images. In bright-field imaging, the directly transmitted beam enters the objective lens. Defect will appear dark because it scatters the beam. While in dark-field imaging, the directly transmitted beam is blocked and only scattered beam enters the objective lens. Dark-field imaging allows us to extract useful information such as planar defects, stacking faults, or particle size. **Figure 3.9** illustrates dark-field and bright-field images formation.

3.8   Energy-Dispersive X-Ray Spectroscopy

Energy-dispersive X-ray Spectroscopy (EDX) is generally used for elemental analysis of a sample. In this work, we used INCA x-sight detector EDX system. **Figure 3.10** shows a simple diagram of electron shells following the Bohr model. At ground state, electrons of an atom within the sample are positioned in discrete energy levels. When a high-energy beam of charged particles, for example electrons from SEM or TEM, is focused into the sample, the electron in the inner shell can be ejected from the shell creating a hole. An electron from a higher energy level can then fill the hole while releasing its energy in the form of an X-ray which can be measured using an energy-dispersive spectrometer. Energy of the X-rays is characteristic of the atomic structure of the element and thus this method allows us to measure the elemental composition of the sample.
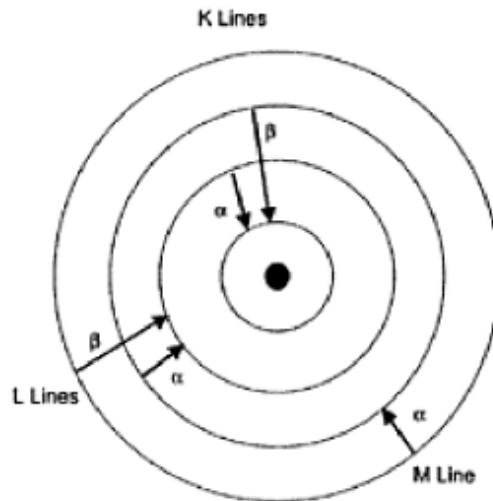
Figure 3.10: Simplified diagram of electron shells, following the Bohr model of the atom.[83]

3.9   Vibrating Sample Magnetometer

Vibrating Sample Magnetometer (VSM), which is based on Faraday's Law of Induction, is used to measure the magnetic properties of a sample. **Figure 3.11** shows a schematic of VSM. In VSM, the sample is placed in a constant magnetic field and vibrated at constant frequency ω in a vertical direction so that the magnetic flux is changing as a function of time. In this work, we used LakeShore 7404 VSM.
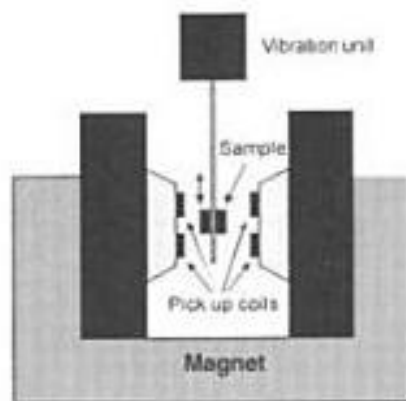
Figure 3.11: Schematic of VSM.[84]

The change in magnetic flux will produce an electric field, according to Faraday's Law of Induction[85], with an effective voltage given by :

$$U = k_c \omega M$$

Equation 3.2

where U is the voltage, k_c is a coefficient determined by calibration, and M is the magnetic moment of the sample. The induced AC voltage can be detected by a set of pick-up coils.

Chapter 4. Solid-State Dewetting of Cobalt Palladium

4.1 Introduction

In recent years, solid-state dewetting[18,27-29,31,36] of metal thin film, has emerged as a promising low-cost nanoparticle fabrication method. This method involves simple steps of depositing the thin film followed by heat treatment. The dewetting or agglomeration process is driven by surface energy minimization facilitated by surface diffusion process. For solid-state dewetting of alloy, it is worthwhile to distinguish two different systems, miscible and immiscible alloy.
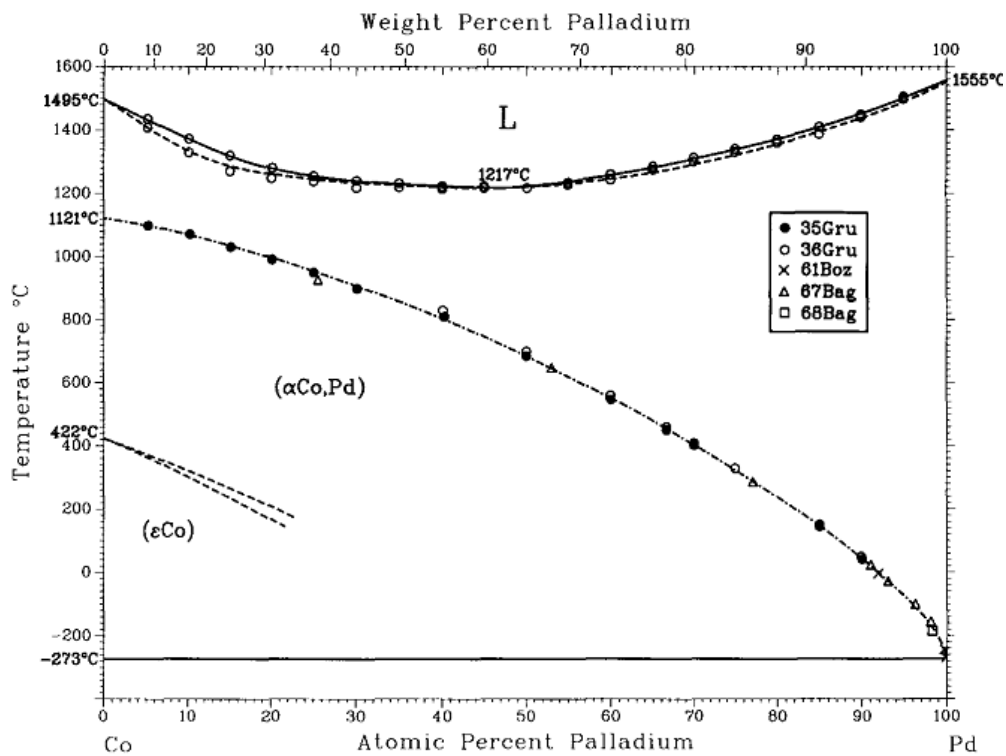
Figure 4.1: Co-Pd phase diagram.[86]

In this chapter, we report a systematic study on the dewetting mechanism of CoPd alloy, which is a miscible alloy.[86] The phase diagram for Co-Pd system is given in **Figure 4.1**. As can be seen, Co and Pd form solid solution

across the entire composition. So far, most studies on solid state dewetting focus on elemental material and only limited works have been done on miscible alloy dewetting[18,36]. Structural characterization of the CoPd film and CoPd nanoparticles will be presented. Dewetting kinetics will be studied using JMA analysis and the results are compared with experimental data. The role of material composition and initial layer configuration on the interparticle spacing, particle density, and size will be discussed.

4.2 Experimental Details

p-type Si (100) wafers were used as substrate for the dewetting experiments. The wafers were covered with resist and cut into 0.5×0.5 cm^2 chips. The resist protected the substrate from debris generated during dicing. The samples were then cleaned in acetone for 30 minutes to remove the resist followed by immersing in IPA for 5 minutes and rinsing with DI water. For the next step, 100-nm Al$_2$O$_3$ layer was sputter-deposited on the Si wafer, serving as a silicidation barrier. Afterwards, 25-nm CoPd film was sputter-deposited with different layer configurations as follows:

(1) 10-nm Pd/15-nm Co, hereafter will be termed as 10Pd/15Co.

(2) 2-nm Pd/5-nm Co/3-nm Pd/5-nm Co/3-nm Pd/5-nm Co/2-nm Pd, hereafter will be termed as 2Pd/5Co/3Pd/5Co/3Pd/5Co/2Pd.

(3) 15-nm Co/10-nm Pd, hereafter will be termed 15Co/10Pd.

(4) 3-nm Co/3-nm Pd/4-nm Co/4-nm Pd/4-nm Co/3-nm Pd/4-nm Co, hereafter will be termed as 3Co/3Pd/4Co/4Pd/4Co/3Pd/4Co.

The different layer configurations are schematically shown in **Figure 4.2**. In addition, 25-nm Co film and 25-nm Pd film were also deposited to

study the behavior of the alloy material constituents. 25-nm Au film was prepared as a comparison.
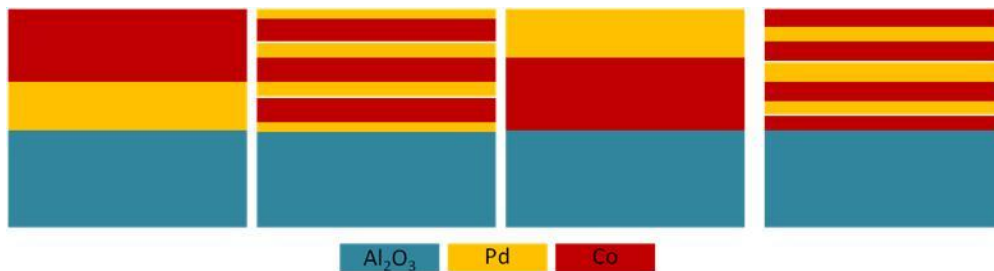
Figure 4.2: Schematic illustration of different CoPd layer configurations used in this study. Co atomic ratio is fixed at 66.7 at. %.

The samples were loaded into a furnace in forming gas ambient (10% H_2) with 1800 sccm flow rate. The furnace was then heated up with a ramp rate of about 20 ℃/minute to the setpoint temperature. It takes 1-2 minutes before the temperature stabilizes. After maintaining the setpoint temperature for the desired duration, the furnace was subsequently cooled down to room temperature, which takes approximately 4 hours, before the samples were retrieved. The sample morphology after annealing was characterized using SEM (FEI Nova NanoSEM 230) and TEM (JEOL 2010F and JEOL3010). Composition analysis was carried out using EDX (INCA x-sight detector).

4.3   Effect of Layer Configuration

To investigate the effect of initial layer configuration on the CoPd dewetting process, the four different layer configurations were deposited and then annealed at 800 ℃ for 2 hours. **Figure 4.3** shows that the morphologies of the different layer configurations after annealing are similar. The average interparticle spacing for all four layer configurations of CoPd films, each of which was calculated from 50 data points in an SEM image, is approximately

600 nm. This suggests that Co and Pd intermixed completely during the dewetting process.
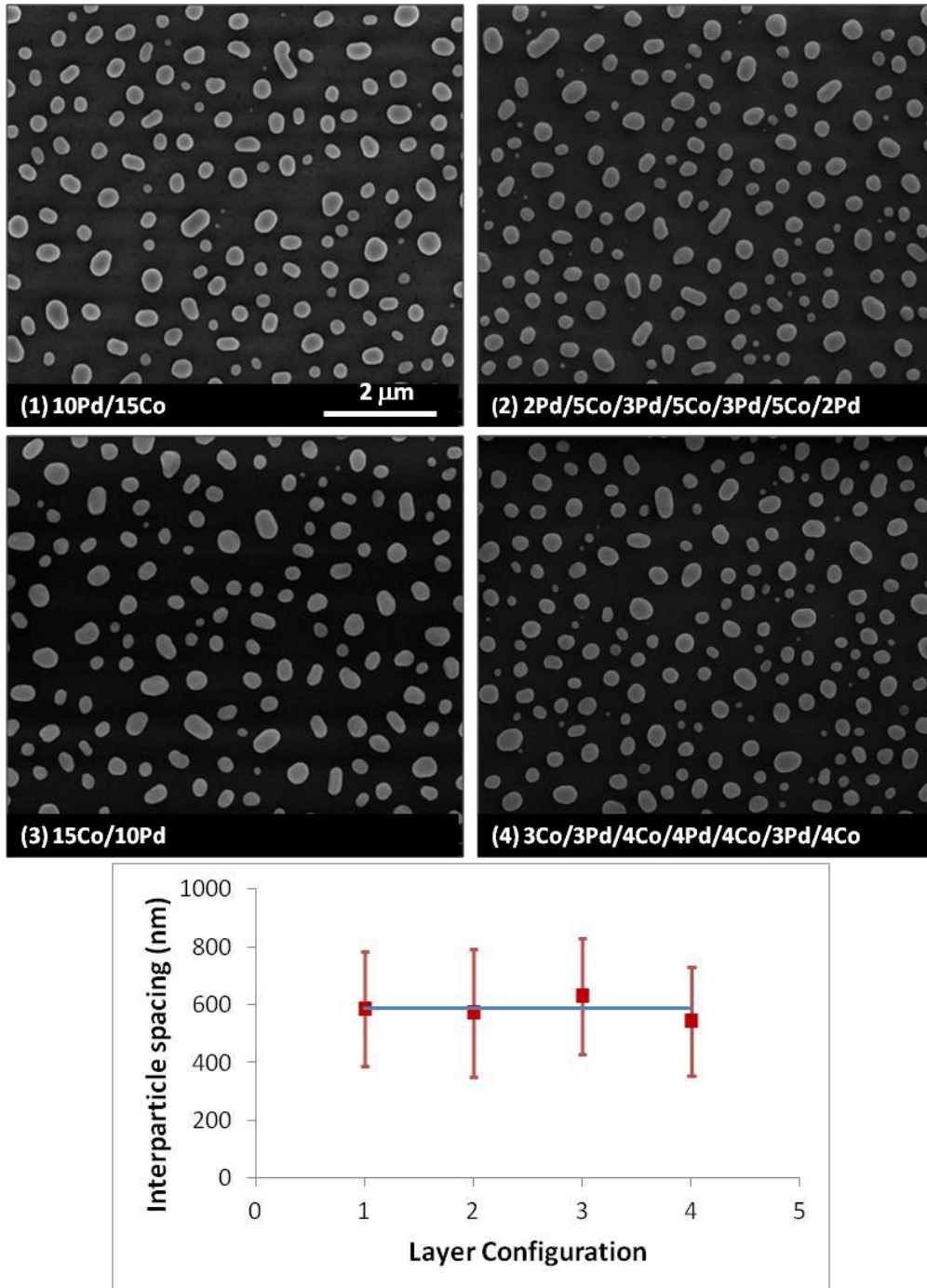
Figure 4.3: CoPd (66.7 at. % Co) film after annealing at 800 ℃ for 2 hours and the average interparticle spacing for different layer configurations.

4.4 Stages of Dewetting

It has been studied that elemental material undergoes specific stages during the dewetting process[35,36]. Furthermore, Muller and Spolenak[36] also found that miscible AuPt alloy undergoes specific stages similar to Au film which is divided into hole initiation, hole growth, and hole coalescence or particle formation.

Six stages are proposed in this work for the dewetting process of Au, Co, CoPd and Pd, as follows: hole initiation, hole growth, interconnected islands, isolated islands, island coarsening, and particles. **Figure 4.4**, **Figure 4.5** and **Figure 4.6** capture these dewetting stages for Au, Co and Pd thin film, respectively. Co and Pd form miscible alloy in the entire range of temperatures under study. It is expected that CoPd alloy thin film will undergo similar dewetting stages as its elements, as is confirmed by **Figure 4.7.** After annealing at 500 ℃ for 15 minutes, formation of holes was initiated on the CoPd thin film. Subsequently, the holes grew in number and size after longer annealing time of 2 hours. The hole grew via fractal-mode mechanism instead of capillary mode. When the sample was annealed at a higher temperature of 550 ℃ for 15 minutes, interconnected islands were formed. When annealed further, the interconnected islands broke up into irregular-shaped islands before going through a coarsening process, as can be seen in the transition from 600 ℃, 15 minutes to 800 ℃, 2 hours, as indicated by the arrow in **Figure 4.7**. Finally, the particles evolved into spherical or faceted shapes.
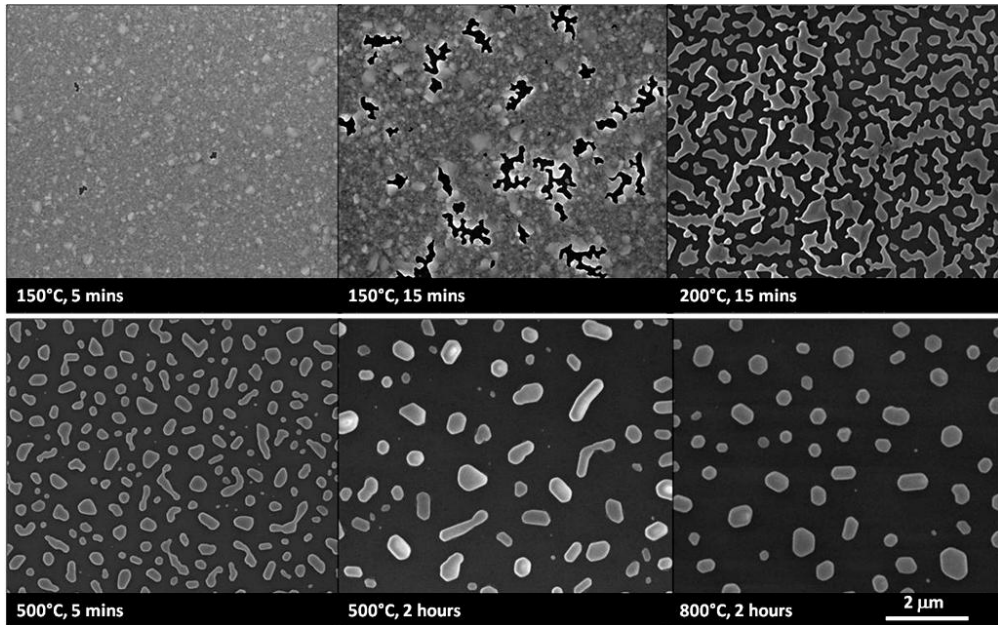
Figure 4.4: Stages of dewetting for 25-nm Au film.
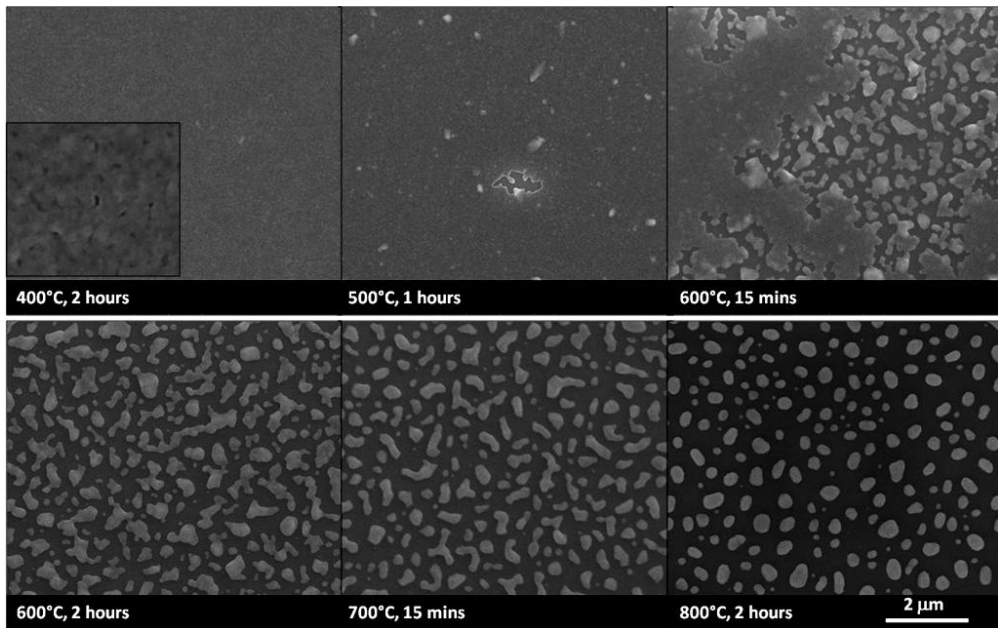
Figure 4.5: Stages of dewetting for 25-nm Co film.
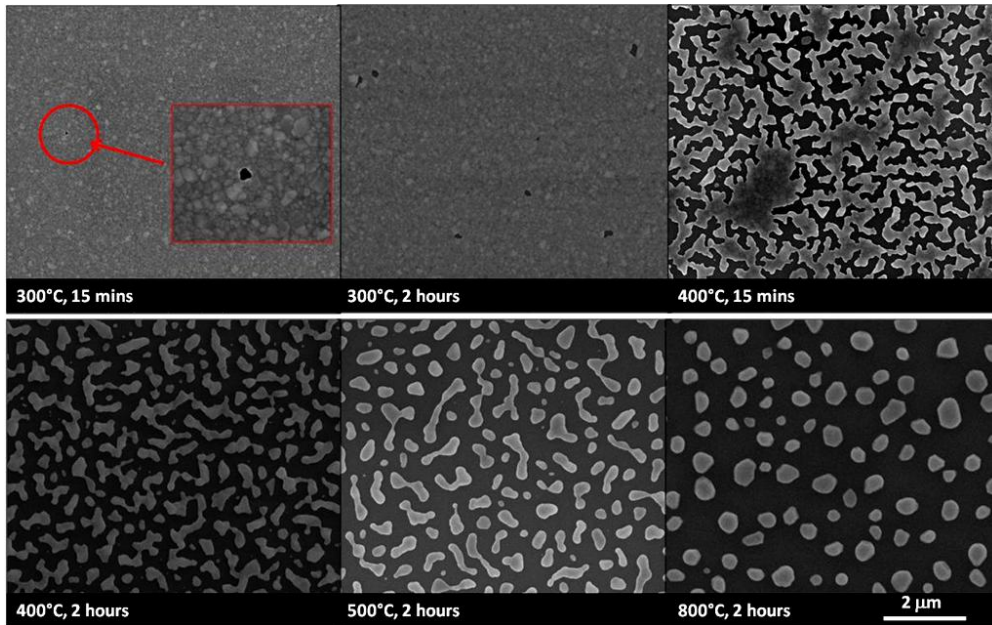
Figure 4.6: Stages of dewetting for 25-nm Pd film.
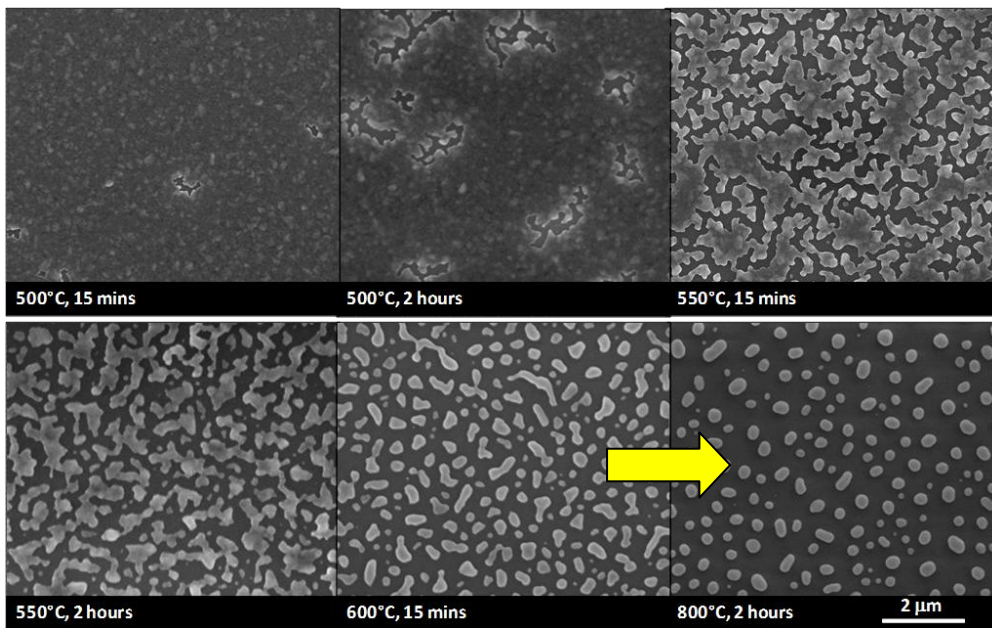
Figure 4.7: Stages of dewetting for 25-nm CoPd (66.7 at.% Co) film.

Table 4.1: Relevant surface and interfacial energies for Au, Pd, Co, and Alumina substrate. $\gamma_{SP} - \gamma_{SV}$ is obtained from subtracting the work of separation[87] from the particle surface energy[88,89] according to Eq. (1) in [87].

Surface / Interfacial Energy	Au (in J/m²)	Pd (in J/m²)	Co (in J/m²)	Ref.
γ_{111}	0.886	1.382	2.70	88,89
γ_{100}	1.083	1.661	2.78	88,89
γ_{110}	1.114	1.671	-	88
γ_{SP} - γ_{SV} **(Alumina)**	0.22	0.61	1.59	87,88,89

The equilibrium shape of a free-standing crystal is determined by the energy minima in the Wulff plot.[54] For fcc metals, {111} planes possess the lowest surface energy because the atoms on the surface are only deprived of three out of twelve neighbors.[54,90] It has been established earlier, however, that for particles sitting on a substrate, substrate surface energy and substrate-particle interfacial energy must also be taken into account to determine the equilibrium shape of the particles (Winterbottom construction). **Table 4.1** lists the relevant surface and interfacial energies for Winterbottom plot construction. **Figure 4.8a** shows the equilibrium particle shapes for Au, Pd, and Co constructed using Wulffmaker algorithm[91] run on Wolfram CDF Player platform.[92] The Winterbottom construction was based on the information that the three metals have fcc crystal structure and belong to $m\bar{3}m$ point group.[93] The equilibrium shape is obtained by minimizing:

$$\sum_{i=1}^{n} \gamma_i A_{fi}$$
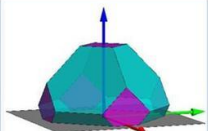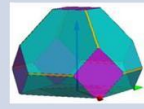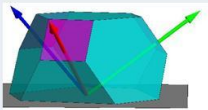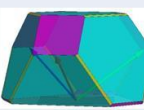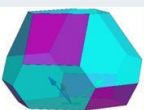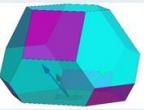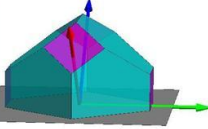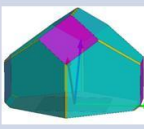
Equation 4.1

where γ is the surface/interfacial energy and A_f is the facet area.

Figure 4.8a and **b** display the predicted equilibrium shapes for Au, Pd, Co, and CoPd particles on Al_2O_3 substrate for various surface normal possibilities: [100], [111], and [110]. This prediction agrees well with observation, as shown in **Figure 4.8c**, in that Au and Pd particles are faceted.

61

In particular, they appear hexagonal from the top-view SEM images, suggesting that these particles have (110) surface normals (*c.f.* **Figure 4.8b**). Co particles, however, are found to be more spherical. These results agree with previous studies on dewetting of Au[27] and Co[29] on topographical template. It was found that after dewetting the Co particles surface appear roughened indicating surface-oxide formation[94] and have fcc structure[29].

There can be two possible reasons for the spherical shape of dewetted Co particles. First, Co has a low surface diffusivity compared to Pd and Au, as shown in **Table 4.2**. Thus, Co might need a longer time to reach its equilibrium shape. Secondly, Co has a high reactivity to any oxygen[95] residue present in the chamber and hence, the surface energy anisotropy can be altered. The bottom panels of **Figure 4.8c** show that CoPd particles are composed of both faceted and spherical shape particles, with less prominent faceting as compared to Pd. This suggests that surface energy anisotropy of CoPd lies in between that of Co and Pd. It can also be seen that the faceted CoPd particles do not have any preferred surface normal orientations. This observation will later be corroborated from TEM SAED results.

Surface Normal	Au	Pd	Co	CoPd
[100]				
[111]				
[110]				

(a)

(b)

(c)

Figure 4.8: (a)-(b) Tilted and top-view 3D Winterbottom construction for Au, Pd, Co, and CoPd particles on Al$_2$O$_3$ substrate for various surface normal possibilities. (c) High-magnification SEM images of Co, Pd, Au and CoPd nanoparticles.

Table 4.2: Bulk and surface diffusivities of Au, Pd and Co at 800 ℃.

Material	Bulk Diffusivity (m^2/s)	Ref.	Surface Diffusivity (m^2/s)	Ref.	Surface Diffusivity on Al$_2$O$_3$ (m^2/s)	Ref.
Au	3.01 x 10^{-14}	[96]	7.89 x 10^{-8}	[97]	3.89 x 10^{-17}	[98]
Pd	2.19 x 10^{-18}	[99]	9.62 x 10^{-11}	[100]	9.15 x 10^{-19}	[101]
Co	4.97 x 10^{-19}	[102]	2.15 x 10^{-12}	[103]	-	

4.5   Dewetting Rate

Although the dewetting stages are basically the same among Au, Co, Pd and CoPd, the interstage transition is material-dependent. It can be seen from **Figure 4.4** to **Figure 4.7** that the transition occurs at the lowest temperature in Au, followed by Pd, CoPd (66.7 at.% Co) and Co. As can be seen in **Figure 4.4**, Au has already formed interconnected islands after annealing for 15 minutes at a temperature as low as 200 ℃. In **Figure 4.6**, Pd thin film formed interconnected islands only at a higher annealing temperature of 400 ℃ for the same duration. Meanwhile, CoPd thin film after annealing at 500 ℃ for two hours was still in hole-growth stage and only formed interconnected islands after annealing at 550 ℃ for 15 minutes (**Figure 4.7**). Interstage transition of dewetting in Co occurs at the highest temperature among the four because even after annealing at 600 ℃ for 15 minutes, continuous film was still observed sporadically (**Figure 4.5**). **Table** 4.2 lists the bulk and surface diffusivities of Au, Pd, and Co at 800 ℃. It can be seen that Au has the highest diffusivity, followed by Pd and Co. Since solid-state dewetting is driven by surface diffusion process, the material with high surface diffusivity should undergo interstage transition at a lower temperature as confirmed by our finding in **Figure 4.4** to **Figure 4.6**.

Figure 4.9 compares the morphology of Co, CoPd (66.7 at.% Co) and Pd thin films after annealing at the same conditions, 500 ℃ for 15 minutes. While Co film was still continuous, CoPd was already in the stage of hole growth and Pd has already formed interconnected islands. This figure suggests that CoPd (66.7 at.% Co) thin film behaves in between Co and Pd thin films during the dewetting process. There is no published data for CoPd or other

alloy surface diffusivity. However, another miscible alloy, Cu-Ni has bulk interdiffusivity increasing monotonically as a function of Cu at. % concentration.[104] Thus, it may be reasonable to expect the surface diffusivity of other miscible alloys to lie in between those of its constituents as well.
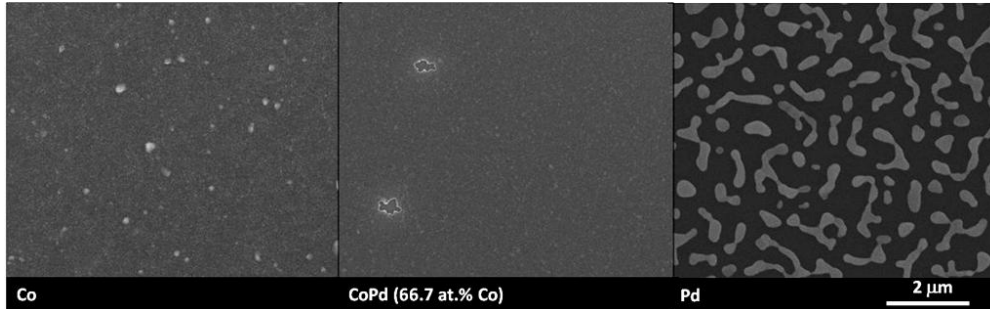
Figure 4.9: Morphologies of Co, CoPd and Pd thin films after annealing at 500 ℃ for 15 minutes.

Muller and Spolenak[36] modeled the dewetting characteristics of Au and AuPt alloy by monitoring the exposed substrate area as a function of annealing duration for the same annealing temperature. Similar to Jiran and Thompson[59], they utilized Johnson-Mehl-Avrami (JMA) equation to calculate the activation energies for void initiation and void growth in Au dewetting. However, they were not able to quantify the results on AuPt alloy. They proposed that Pt contributes in a complex manner to various kinetic processes during dewetting. Here, we tried to plot the CoPd isochronous dewetting behavior as a function of annealing temperature.

Figure 4.10 shows the fraction of exposed substrate area for Co, Pd, CoPd (66.7 at.% Co), and Au as a function of temperature. The exposed substrate area is calculated using ImageJ software.[105] As can be seen, there are two regimes in the substrate area evolution. The first is where the exposed area increases with temperature and the latter is where the exposed area saturates at about 80%. If the first regime is approximated linearly and extrapolated to the

65

x-axis, one can extract the hole incubation temperature (onset of dewetting) for the materials, as shown in **Table 4.3**.
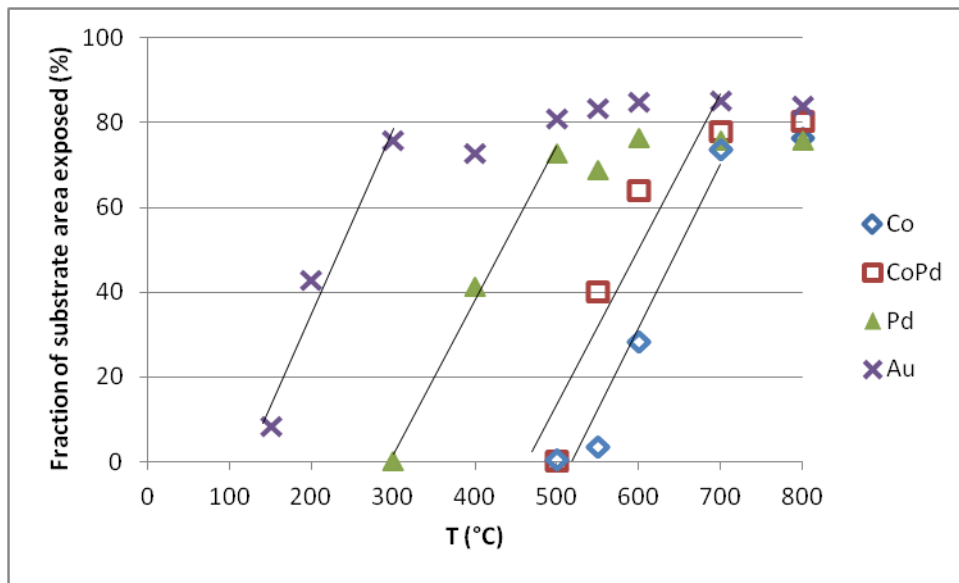
Figure 4.10: Fraction of exposed substrate area as a function of temperature for different materials. The samples were annealed for 15 minutes.

Table 4.3: Hole incubation temperature for different materials annealed for 15 minutes.

Material	Hole incubation temperature (°C)
Co	450 – 620
CoPd	360 – 660
Pd	280 – 320
Au	100 – 150

To better understand the underlying dewetting mechanism, **Figure 4.10** is re-plotted as a function of homologous temperature, as shown in **Figure 4.11**. As can be seen, there is now a profile match between Pd and Au. Pd and Au both have fcc crystal structures and thus, the diffusivity at the same fraction of their melting temperature, i.e. homologous temperature, will be approximately the same.[54,106] This further corroborates that the dewetting process is governed by surface diffusion. The deviation of Co from Au and Pd lines can also be explained in a similar manner. As will be shown from the

TEM studies later, the as-deposited Co has an hcp structure. Brown and Ashby[106] tabulated the melting-point diffusivities for various classes of crystalline solids and from their work, hcp and fcc were actually found to have comparable diffusivities. These data are applicable, however, for bulk or lattice diffusion, while dewetting is understood to be a surface-diffusion process. From the Ellingham diagram,[107] it can be seen that Co is more reactive to oxygen, compared to the noble metals, Au and Pd. For example, at 800 °C, only 10^{-11} atm of O_2 is required to convert Co to CoO. This information, coupled with the high surface-to-volume ratio in both pre-dewetting thin film and post-dewetting nanoparticles, could account for the reduction in surface diffusivity of Co atoms during dewetting. This translates into the smaller fraction of exposed area for Co at the same homologous temperature, compared to Au and Pd. Finally, from **Figure 4.11**, it can also be seen that the CoPd alloy behaves similarly to Co, probably because of high Co content (66.7 at.%).
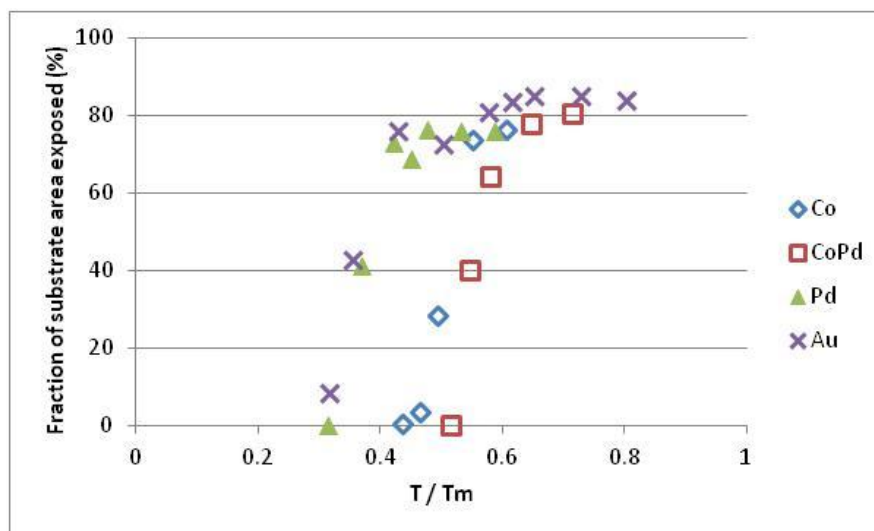
Figure 4.11: Fraction of exposed substrate area as a function of homologous temperature for different materials. The samples were annealed for 15 minutes.

In order to better understand the kinetics of the dewetting process and extract the relevant kinetic parameters, JMA analysis will be carried out on the data. Jiran and Thompson[59] derived the fraction of exposed substrate area as a function of time as follows,

$$A = 1 - exp[-N_h \pi v_h^2 (t - t_i)^2]$$

Equation 4.2
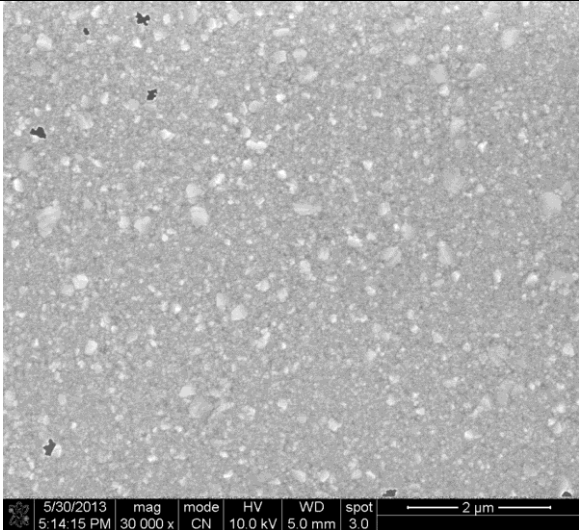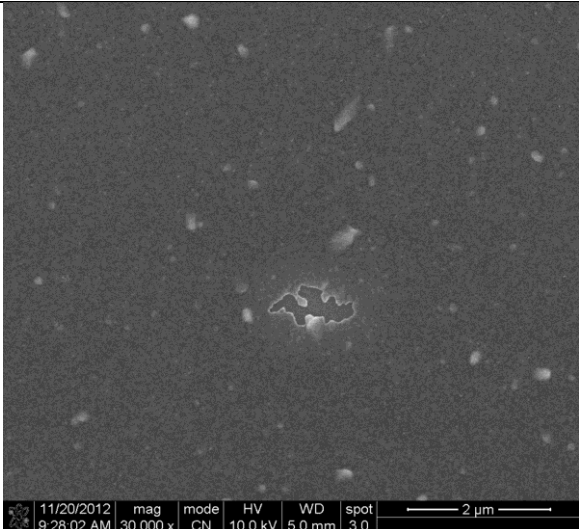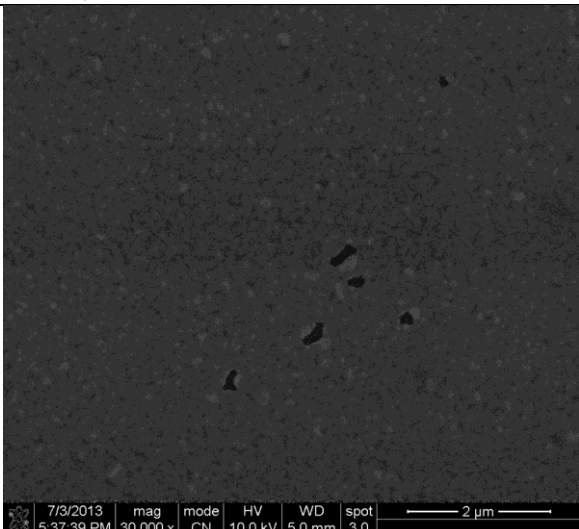
where A is the fraction of exposed substrate area, N_h is the number of void nuclei per unit area, v_h is the void growth rate, and t_i is the void incubation time. N_h is shown to be temperature-insensitive[59] and experimentally determined. Values of N_h for Au, Co, Pd, and CoPd are experimentally determined and tabulated in **Table 4.4**. The void growth rate, assuming time independence, can be expressed as, [43,59]

$$v_h = \frac{2D_s v_s \Omega^2 \gamma_{fv}}{\pi k T h^3}$$

Equation 4.3

where D_s is surface diffusivity, v_s is surface density of atoms, Ω is atomic volume, γ_{fv} is surface energy of the film, h is the film thickness, and kT carries the usual meaning. Values of surface diffusivity at different temperatures for Au, Co, and Pd can be calculated from the knowledge of relevant diffusion constant (D_{S0}) and activation energy (Q_S), as given in **Table 4.5**.

Table 4.4: Number of void nuclei per unit area for Au, Co, Pd, and CoPd as determined from SEM inspection.

Material	N_h (/m^2)	SEM
Au	1.29 x 10^{11}	 150 °C, 15 minutes
Co	1.85 x 10^{10}	 500 °C, 1 hour
Pd	1.11 x 10^{11}	 300 °C, 2 hours
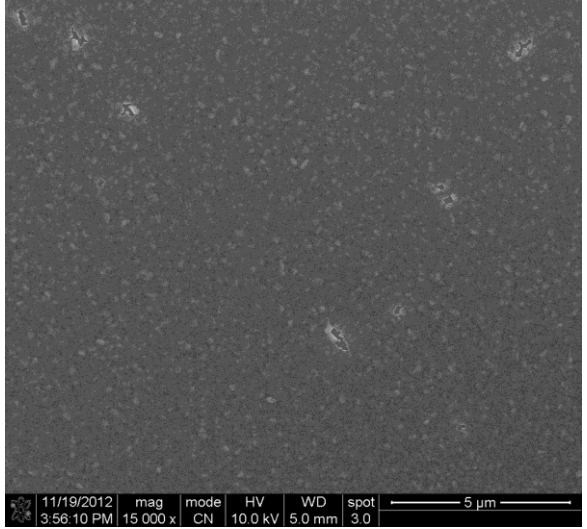
CoPd	5.80×10^{10}	
		500 °C, 15 minutes

Table 4.5: Diffusion constant and activation energy to calculate surface diffusivities of Au, Co, and Pd at different temperatures.

Material	D_{S0} (m^2/s)	Q_S (eV)	Ref.
Au	7.6×10^{-4}	0.68	97
Co	4.8×10^{-13}	0.14	108
Pd	1.4×10^{-5}	1.10	109

Equipped with **Equation 4.2**, **Equation 4.3**, **Table 4.4**, and **Table 4.5**, one can now plot the time evolution of the exposed substrate area for Au, Co, Pd, and CoPd. With appropriate values for the void incubation time (t_i), the generated curves agree with the experimental data, as shown in **Figure 4.12a**. Since t_i is a thermally-activated process, it obeys Arrhenius relationship,

$$t_i = t_{i0} exp \left(\frac{E_A}{kT} \right)$$

Equation 4.4

where E_A is dewetting activation energy. Plotting $\ln(t_i)$ as a function of $1/T$ should then result in a straight line, as shown in **Figure 4.12b**. Taking into account the error in predicting t_i, the kinetic parameter E_A for Au, Co, Pd, and CoPd can be extracted from the slope of each line and tabulated in **Table 4.6**.

70

As can be seen, E_A value for each material is significantly lower than bulk and GB diffusion, suggesting that void initiation is governed by surface diffusion.

(a)

(b)
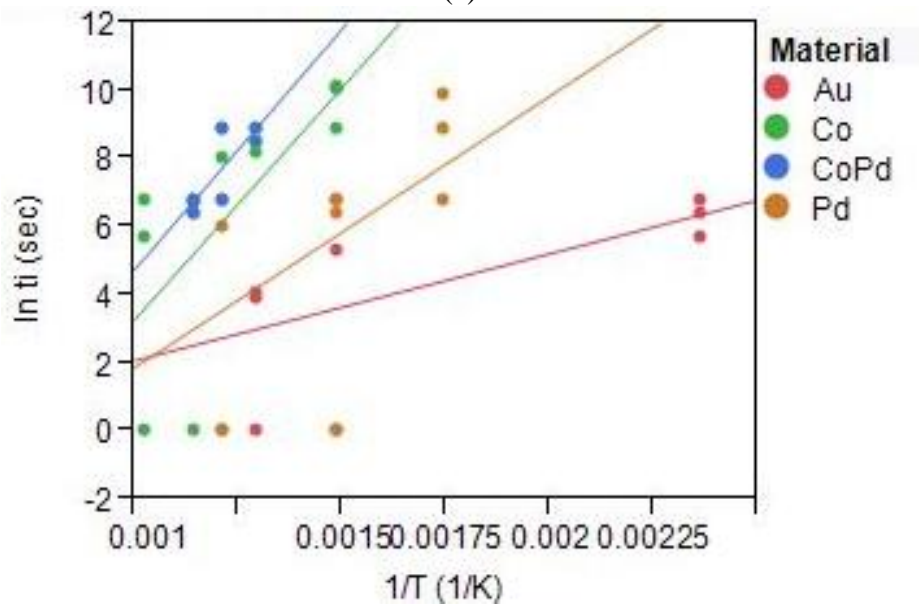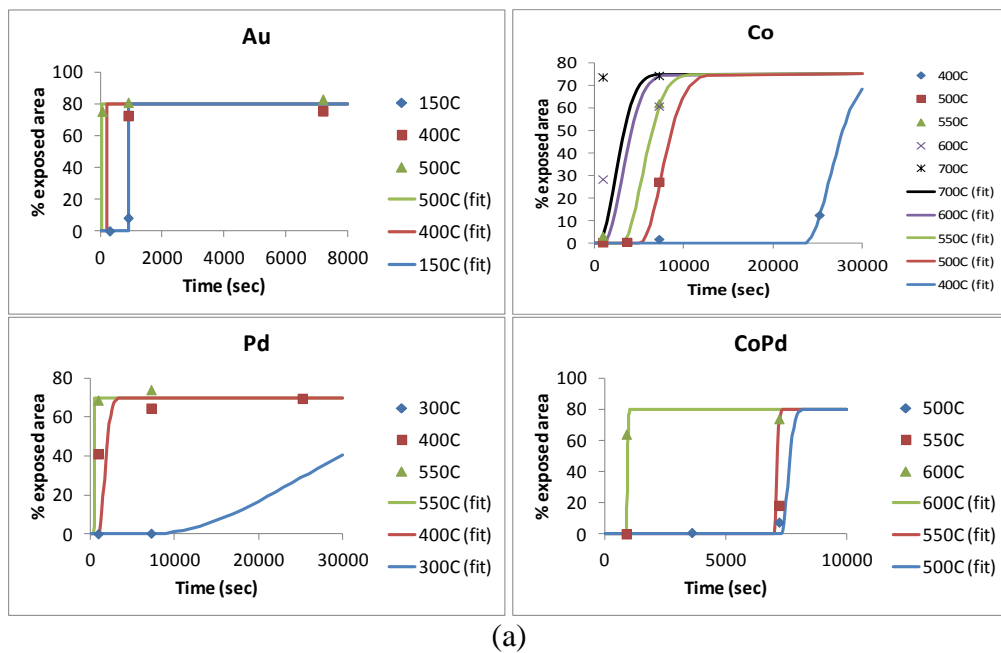
Figure 4.12: (a) Time evolution of the exposed substrate area during dewetting of Au, Co, Pd, and CoPd. Fitted lines were obtained from JMA analysis. (b) Arrhenius plots of the void incubation time for Au, Co, Pd, and CoPd.

Table 4.6: Extracted activation energy for Au, Co, Pd, and CoPd, in comparison with activation energies for surface, GB, and bulk diffusion.

Material	E_A (eV)	$E_{A,surface}$ (eV)	$E_{A,GB}$ (eV)	$E_{A,bulk}$ (eV)
Au	0.27 ± 0.14	$0.4 - 1.4$ [36,97]	$0.88 - 1.16$ [36]	1.84 [54]
Co	1.18 ± 0.43	0.14 [108]	1.68 [108]	2.94 [54]
Pd	0.69 ± 0.42	1.10 [109]	-	2.76 [54]
CoPd	1.22 ± 0.34	-	-	-

4.6 Interparticle Spacing, Particle Density and Particle Size

It has been shown that interparticle spacing of dewetted nanoparticles is proportional to the initial thin film thickness.[29,31] However, in our works, the film thickness was fixed to be 25 nm and we were more interested to study the effect of different material to the dewetted nanoparticles morphologies. As shown in **Figure 4.4** - **Figure 4.7**, the dewetting process starts with void initiation. According to Mulins,[39] when a polycrystalline film is heated, the surface grooves at grain boundaries will deepen owing to surface diffusion and evaporation – condensation processes. If there is sufficient energy, the grooves will expose the substrate. At the same time, during the annealing process, grain growth occurs. If there is no limitation to the growing grain size and grain boundary grooving is uniform, we might predict the interparticle spacing by estimating the grain size at the time void is formed. However, grain size in thin film is generally proportional to the film thickness and grain boundary grooving is not uniform, generally occurs at triple junction. Thus we cannot take this approach.

Figure 4.13 summarizes interparticle spacing, particle diameter and particle density of Co, CoPd (66.7 at. % Co), Pd and Au after annealing at 800 ℃ for two hours. For each material, interparticle spacing and particle diameter for each material were measured from 50 data points and particle

density was determined by dividing the total number of particles with the SEM imaging area with 30,000X magnification. As shown in the figure, interparticle spacing, particle diameter and particle density are material-dependent.

In **Figure 4.13a**, the average interparticle spacing increases in the following order: Co, CoPd, Pd, Au. As the interparticle spacing is also influenced by the diffusivity, the result shows an agreement with the diffusivity trend shown in **Table 4.2**. **Figure 4.13b** shows that the average particle diameter also increases in the same order as the interparticle spacing. This trend is expected following volume conservation argument in that sparser particles should have larger volumes. The experimentally determined particle density is presented in **Figure 4.13c**. The large scatter bar presented in **Figure 4.13a** and **b** is due to the fact that the film is not patterned.[10,27] **Figure 4.13d** shows that there is a correlation between particle density and hole density. Au has relatively high hole density but ends up with low particle density due to significant coarsening. Co, on the other hand, has relatively low hole density but ends up with high particle density due to limited coarsening. This trend can be explained in the diffusivity trend shown in **Table 4.2**. Initiated hole density and final particle density are determined by surface self-diffusivity and surface diffusivity on the substrate (Al_2O_3 in our case). High hole density in Au is caused by its high surface self-diffusivity, but due to its high surface diffusivity on Al_2O_3, significant coarsening ensues, resulting in a low particle density. Similar line of reasoning applies for Co.

From **Figure 4.13**, it can also be observed that the interparticle spacing, particle diameter and particle density of CoPd lie in between that of Co and

Pd. This is consistent with the observation of the dewetting rate of CoPd as described in **Section 4.5**, in that CoPd dewets faster than Co but slower than Pd.
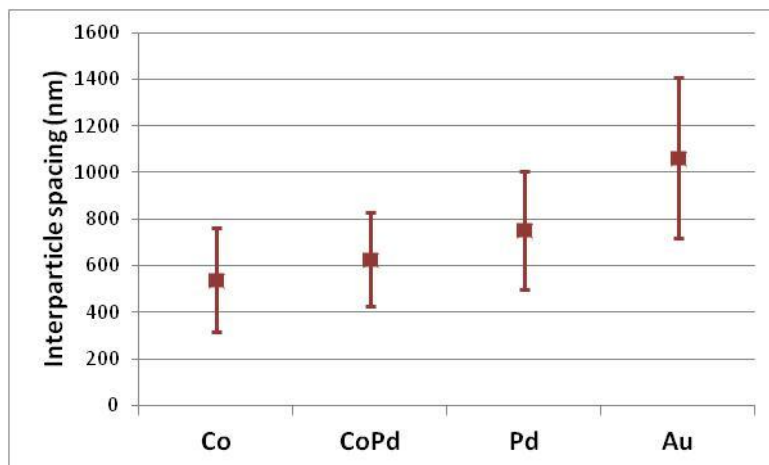
(a)
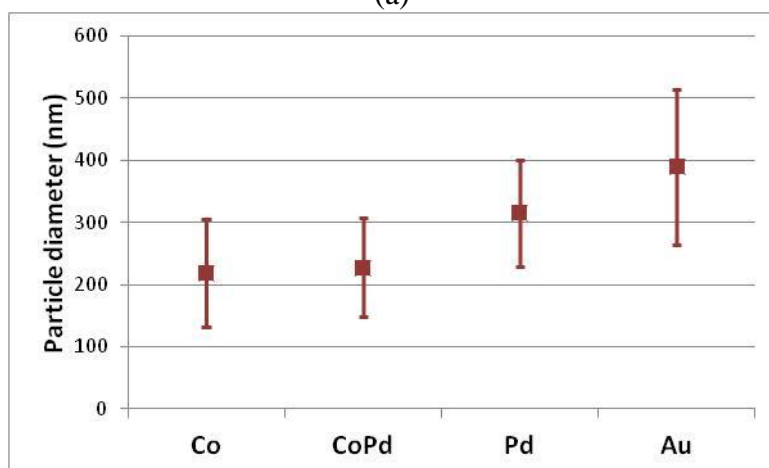
(b)
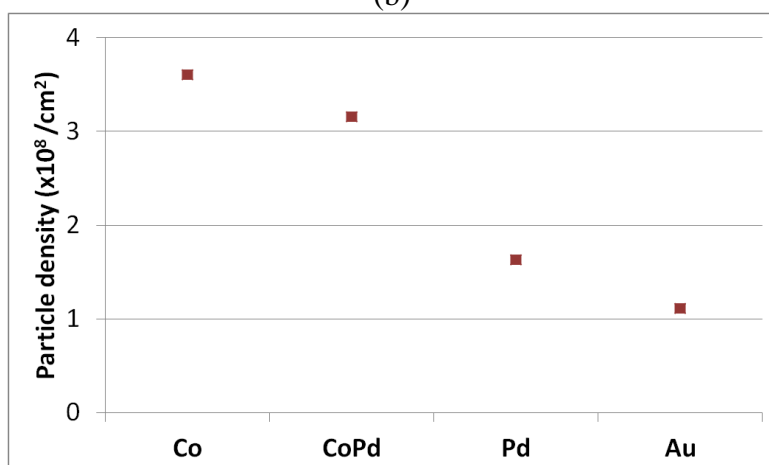
(c)
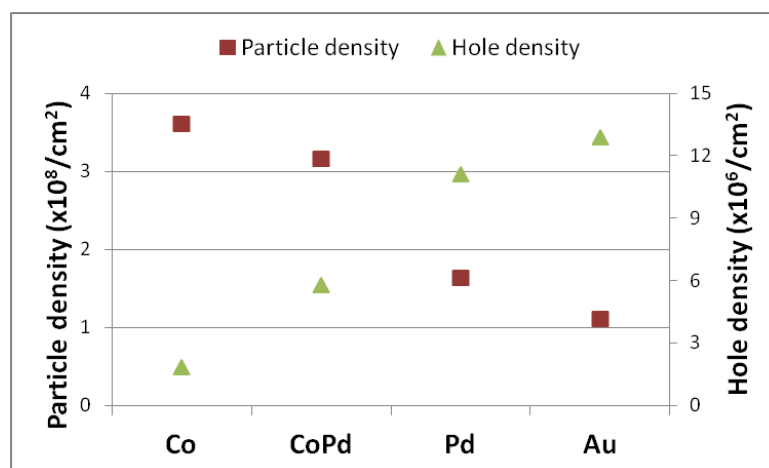
(d)

Figure 4.13: (a) Average interparticle spacings, (b) average particle diameter, (c) particle density, and (d) particle vs. hole density, for different materials after annealing at 800 ℃ for two hours.

4.7 TEM Studies

TEM study was performed to examine the microstructure of the films and the nanoparticles at a higher magnification than SEM as well as to do compositional EDX analysis. **Figure 4.14a** and **b** show the TEM images of as-deposited CoPd thin film and CoPd thin film after annealing at 500 ℃ for 15 minutes. Under this annealing condition, the film remains mostly continuous. As can be seen, annealing causes grain growth in the film from ~10 nm to ~40 nm.

Figure 4.14c and **d** show the respective Selected-Area Electron Diffraction (SAED) patterns of samples shown in **Figure 4.14a** and **b**, respectively. As-deposited film shows planes from both Co and Pd. This is expected because the layers are deposited sequentially. As can be seen in **Figure 4.14c**, we can identify hcp Co $<10\bar{1}0>$, $<0002>$, $<10\bar{1}1>$, $<10\bar{1}2>$ planes, which indicate that as-deposited Co has an hcp structure. The SAED pattern after annealing shows that hcp Co planes have disappeared. The

resulting CoPd alloy has an fcc structure with random texture (no missing plane).
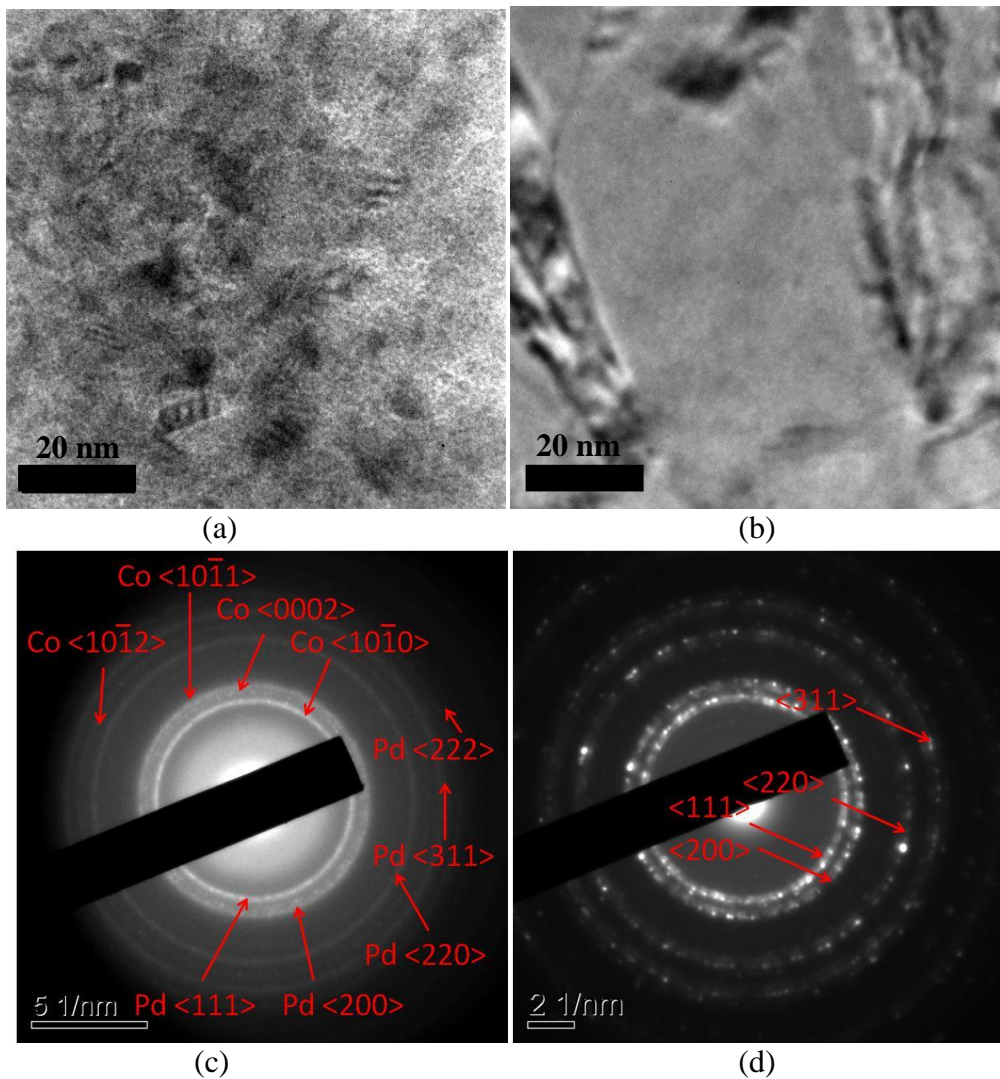
Figure 4.14: TEM images of CoPd thin film: (a) as-deposited and (b) after annealing at 500 ℃ for 15 minutes. (c) and (d) are SAED patterns from (a) and (b), respectively.

When annealed at 800 ℃ for 2-hours, the film has dewetted into an array of particles. The particles can be single-crystalline or polycrystalline. **Figure 4.15** shows a single-crystalline and a polycrystalline particle with their respective SAED patterns. As can be seen in **Figure 4.15c**, the single-crystalline particles do not have preferred texturing, i.e. all (111), (100), and (110) orientations are present in the array of particles. **Figure 4.16** shows

more examples of polycrystalline particles. It can be seen that when the particle was imaged with a different tilt-angle, a change in contrast is observed, indicating the presence of multiple crystal orientations in a single particle. Besides the high angle grain boundaries, some twinnings can also be observed as shown in **Figure 4.16b.**

(a)

(b)

(c)

(d)
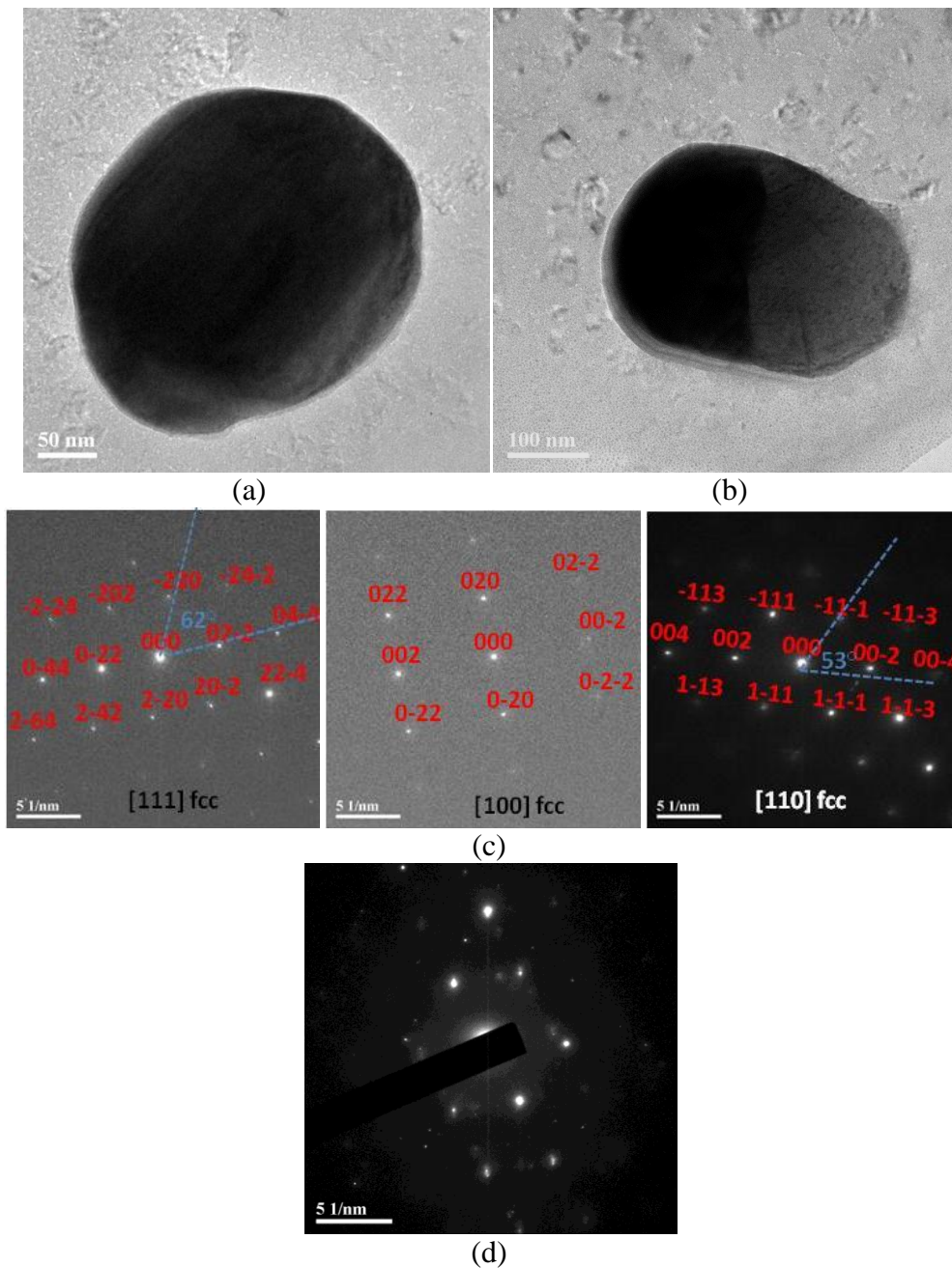
Figure 4.15: TEM images showing (a) single-crystalline and (b) polycrystalline CoPd particles after annealing at 800 ℃ for 2 hours. (c) and (d) are the SAED patterns for single-crystalline and polycrystalline particles, respectively.
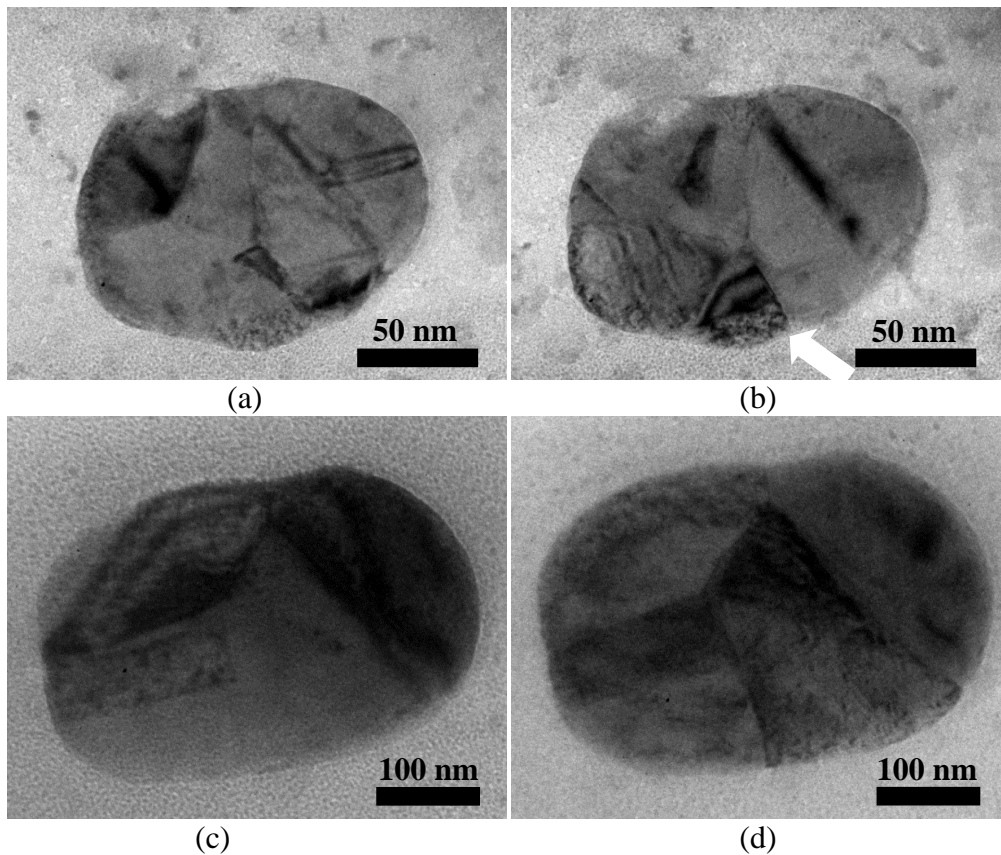
Figure 4.16: (a) and (c) are TEM images of CoPd particles after annealing at 800 °C for 2 hours. (b) and (d) are 10°-tilted images of (a) and (c) respectively. Arrow in (b) indicates twins.

We performed EDX measurement on the particles dewetted from different layer configurations to investigate the influence of number of layers and layer sequence on material segregation among the particles. The results reveal that at 800 °C and 2-hour annealing time, there is little variation in the elemental composition among the particles, indicating that Co and Pd have mixed well prior to forming the particles.

We observed thickness variation in some of particles with different contrast. **Figure 4.17** shows the EDX line-scan and EDX mapping results of such particle. As can be seen from the EDX line-scan some region has more Co and more Pd than the other region, indicating thickness variation. The Co at. % in this region is ~8% higher. **Figure 4.18** shows that the profile of the

EDX line scan does not change with a change in the tilt angle (0 and 10 °). This shows that EDX signal yield is independent of crystallographic orientation. Particles with thickness variation can be observed in the tilted view SEM image of the particle (**Figure 4.19**)
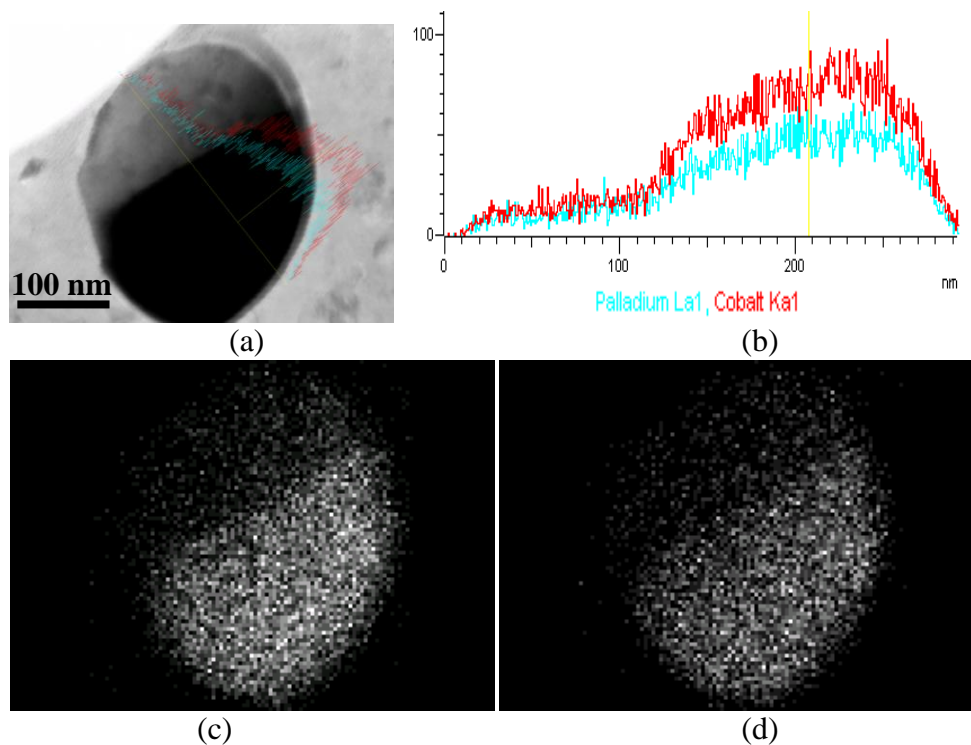
Figure 4.17: (a) Polycrystalline CoPd nanoparticle, (b) the corresponding EDX line-scan, (c) Co-element EDX mapping, and (d) Pd-element EDX mapping.
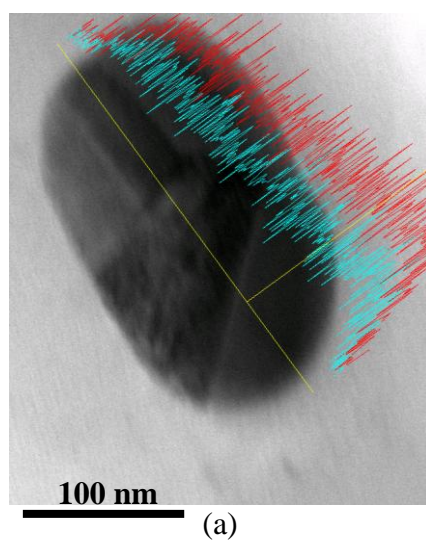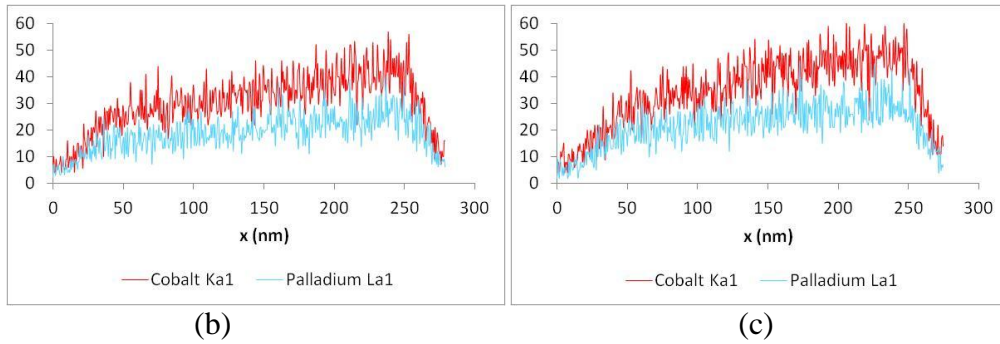
Figure 4.18: (a) TEM image of polycrystalline CoPd nanoparticle. (b) and (c) are the corresponding EDX line-scan for tilt angle of 0 ° and 10 °, respectively.
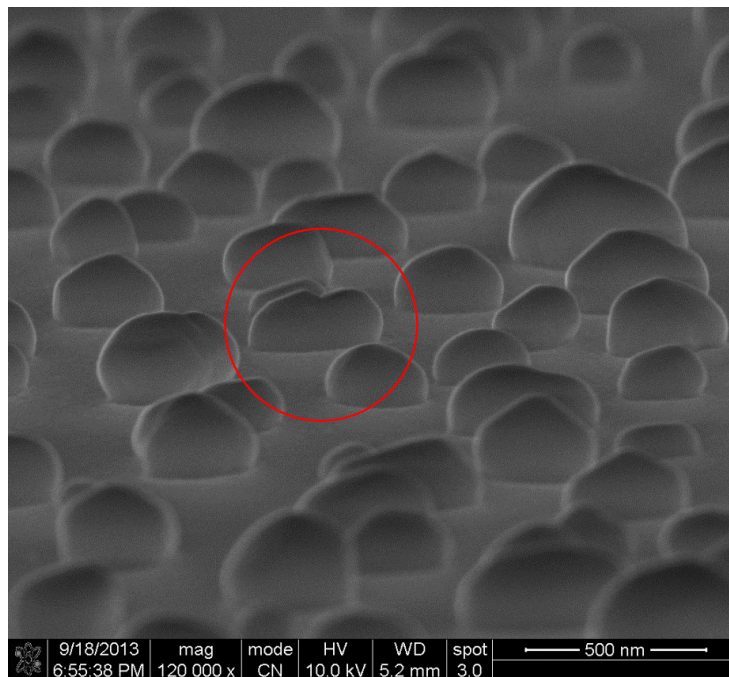
Figure 4.19: 80 °-tilted view of CoPd nanoparticles.

4.8 Summary

This study has provided a better understanding of the dewetting mechanism of CoPd alloy, which is a miscible system. We establish that CoPd alloy undergoes similar stages of dewetting as elemental materials. We found that interstage transition and interparticle spacing are material-dependent, particularly determined by surface diffusivity. CoPd interstage transition was found to be in between Co and Pd. Equilibrium particle shape was predicted

using Winterbottom construction and the results were compared with experimental finding. CoPd particle shape was found to adopt a combination of its Co and Pd constituents. We characterized the CoPd dewetting behavior as a function of annealing temperature. Hole incubation temperature was found to be material-dependent, that is lower for material with higher surface diffusivity. Plotting the area fraction transformed as a function of homologous temperature allows one to distinguish the effect of crystal structure. Fcc materials (Au and Pd) exhibit unique characteristics as compared to hcp material (Co). JMA analysis was used to predict the fraction of area transformed for each material and agrees with the experimental data. Void incubation time and its dewetting activation energy were extracted for Au, Co, Pd, and CoPd, and it was concluded that surface diffusion is the dominant mechanism.

Chapter 5. Solid-State Dewetting of Cobalt Gold

5.1 Introduction

In Chapter 4, we have presented a systematic study on the solid-state dewetting of a miscible system, namely the CoPd system. In this chapter, we investigate the dewetting characteristics of CoAu which forms immiscible alloy in its whole range of composition at room temperature,[110] as shown by the phase diagram for Co-Au system in **Figure 5.1**.
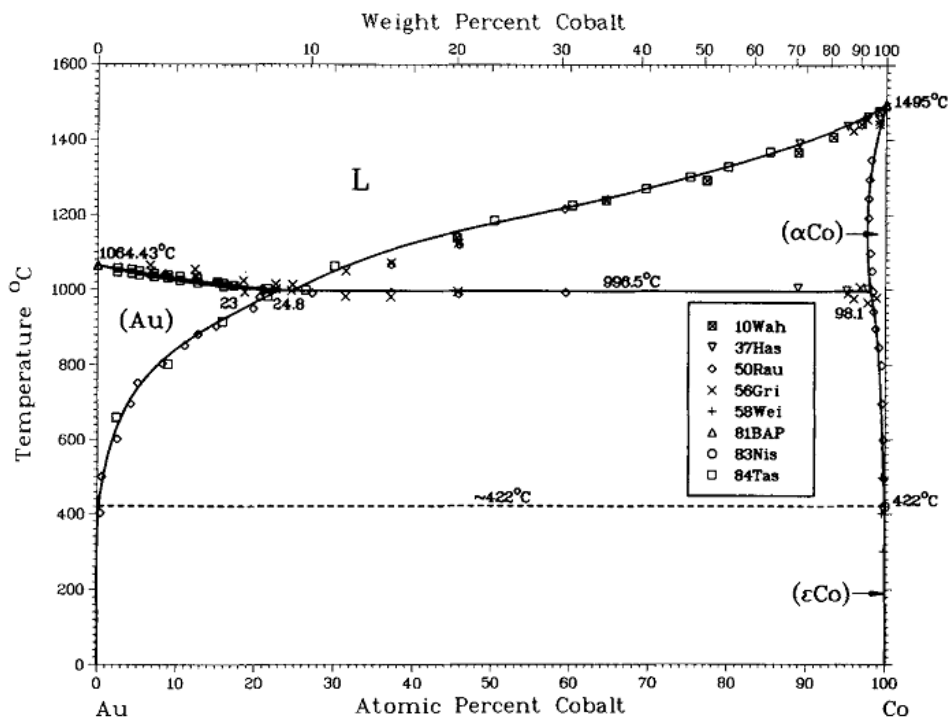
Figure 5.1: Co-Au phase diagram.[110]

Most immiscible alloy dewetting studies focused on its liquid-state dewetting mechanism.[16,17,111,112] However, for some applications, solid-state dewetting is preferred, for example to maintain magnetic properties.[18] Solid-state dewetting is a surface diffusion process which is significantly different from bulk diffusion in liquid-state dewetting. So far, studies on solid-state dewetting of immiscible alloy has mainly focused on the synthesis of unique

nanostructures, such as composite nanoparticles.[70,72] Interestingly, several miscible systems were found to exhibit phase separation and has been utilized to fabricate porous nanostructures using selective chemical etching.[65,66] In this work, we focus on CoAu solid-state dewetting mechanism. As in Chapter 4, we discuss dewetting stages, dewetting characteristics, morphologies and compositional study of CoAu alloy.

5.2 Experimental Details

p-type Si (100) wafers were used as substrate for the dewetting experiments. The wafers were covered with resist and cut into 0.5 cm $\times$ 0.5 cm chips. The resist serves to protect the substrate from debris generated during dicing. The samples were then cleaned in acetone for 30 minutes to remove the resist followed by immersing in IPA for 5 minutes and rinsing with DI water. For the next step, 100-nm Al_2O_3 layer was sputter-deposited on the Si wafer, serving as a silicidation barrier. Afterwards, 25-nm CoAu films with different composition were sputter-deposited as follows:

- Composition 1: 3-nm Co/22-nm Au
- Composition 2: 15-nm Co/10-nm Au
- Composition 3: 22-nm Co/3-nm Au
- Composition 4: 3-nm Au/22-nm Co
- Composition 5: 10-nm Au/15-nm Co
- Composition 6: 22-nm Au/3-nm Co
- Composition 7: 10-nm Co/15-nm Au

25-nm Co film and 25-nm Au film were also deposited to study the behavior of the alloy material constituents.

83

The samples were loaded into a furnace in forming gas ambient (10% H_2) with 1800 sccm flow rate. The furnace was then heated up with a ramp rate of about 20 °C/minute to the setpoint temperature. It takes 1-2 minutes before the temperature stabilizes. After maintaining the setpoint temperature for the desired duration, the furnace was subsequently cooled down to room temperature, which takes approximately 4 hours, before the samples were retrieved. The sample morphology after annealing was characterized using SEM (FEI Nova NanoSEM 230) and TEM (JEOL 2010F and JEOL3010). Composition analysis was carried out using EDX (INCA x-sight detector).

5.3   Stages of Dewetting

As discussed in **Section 4.4**, metal thin films, including CoPd alloy which is a miscible system, undergoes specific dewetting stages, which consist of hole initiation, hole growth, interconnected islands, isolated islands, island coarsening, and particles. In this section, we investigate if CoAu alloy as an immiscible system also undergoes the same dewetting stages.

Figure 5.2 shows CoAu alloy thin films which consist of 15-nm Co and 10-nm Au (69.8 at. % Co) annealed at various temperatures for different durations. As can be seen, the CoAu dewetting stages are similar to those of CoPd. After annealing at 500 °C for 15 minutes, formation of holes were initiated on the CoAu thin film. Subsequently, the holes grew in number and size after longer annealing time of 2 hours. When the sample was annealed at a higher temperature of 550 °C for 15 minutes, interconnected islands were formed. When annealed further, the interconnected islands broke up into irregular-shaped islands before going through coarsening process, as can be

seen in the sample that was annealed at 600 ℃ for 2 hours. Finally, after annealing at 800 ℃ for 2 hours, the particles evolved into mostly faceted shape.
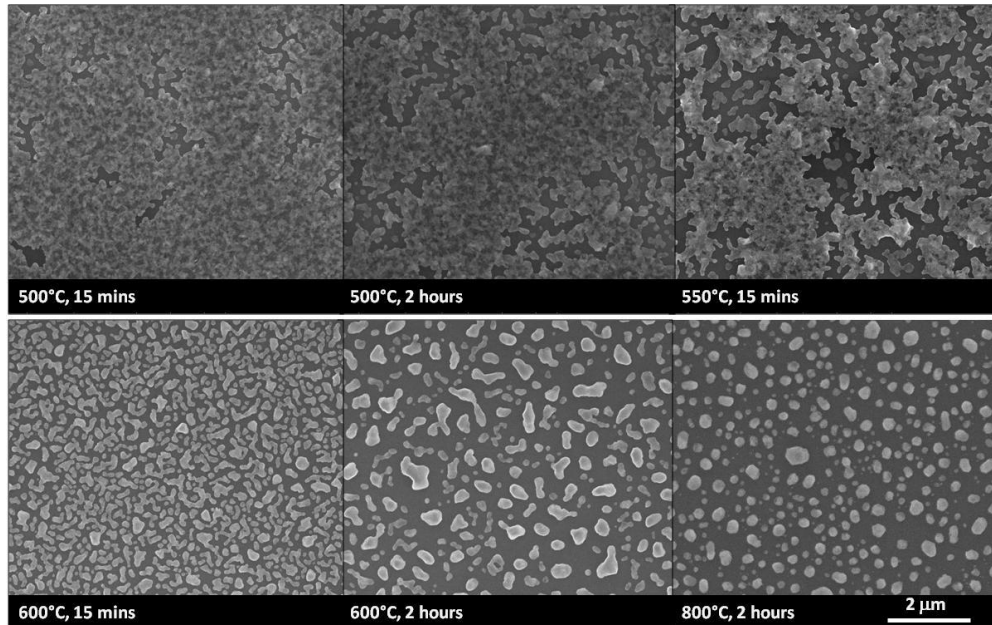
Figure 5.2: Stages of dewetting for 25-nm CoAu (69.8 at.% Co) film.

As discussed previously in **Section 4.4**, particles adopt faceted or spherical shape depending on its surface energy anisotropy. Au has low ratio of γ_{min} / γ_{max} and thus prefers faceted shape while Co has relatively isotropic surface energy and thus forms more spherical particles. In CoAu alloy, the dewetted particles can consist of Au-rich and Co-rich regions. **Figure 5.3** shows high magnification images of CoAu alloy (69.8 at. % Co) after annealing at 800 ℃ for 2 hours. The sharp contrast in BSE image is caused by the strong dependence of backscattered electron yield on atomic number.[81] In this case, Au has much greater atomic number than Co, i.e. $Z_{Au} = 79$ and $Z_{Co} = 27$, respectively. Therefore, we can clearly distinguish the bright region as Au-rich (Region A) and the dark region as Co-rich (Region B). Other studies on the dewetting of immiscible alloy have also reported that a single particle can

85

contain two different phases.[70,72] **Figure 5.3** also revealed that the Au-rich (bright) region is generally faceted while the Co-rich (dark) region can be either faceted or spherical.
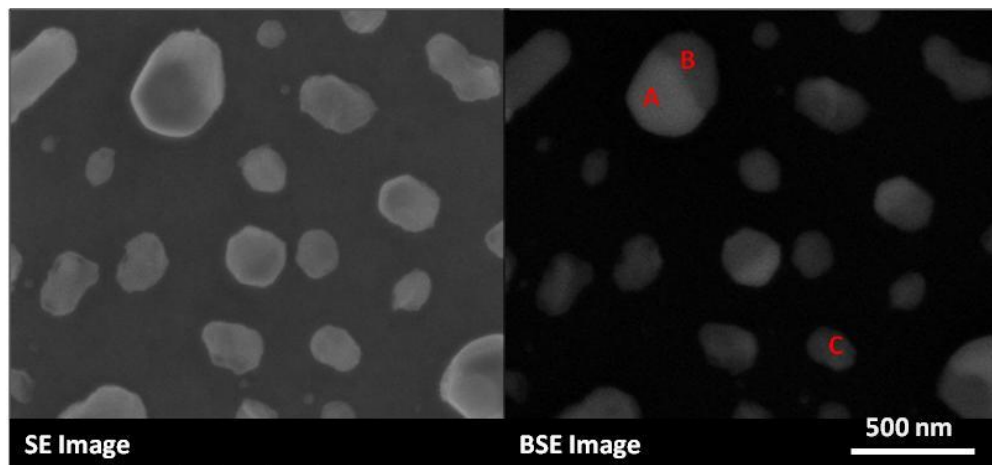
Figure 5.3: High magnification images of CoAu alloy (69.8 at.% Co) after annealing at 800 ℃ for 2 hours. A: faceted Au region, B: faceted Co region, C: spherical Co particle.

5.4   Dewetting Characteristics

Interstage transition in CoAu alloy is determined by its composition as well as its layer sequence. **Figure 5.4** shows morphologies of 25 nm CoAu thin films with three different Co layer thicknesses (3 nm, 15 nm and 22 nm) and different layer sequence after annealing at 500 ℃ for 15 minutes. **Figure 5.5** shows corresponding BSE images of **Figure 5.4**. As can be seen, as the Co content increases, the interstage transition becomes slower. CoAu with 3 nm Co already formed mostly isolated islands while CoAu with 15 nm Co were still in interconnected islands stage and CoAu with 22 nm Co were in hole initiation growth. As a comparison, 25 nm Au film annealed under the same condition has formed isolated islands and 25 nm Co film annealed under the same condition was still continuous (**Figure 5.6**). This is due to the difference in surface diffusivity, as listed in **Table 4.2 (Chapter 4)**. From **Figure 5.4**, it

can also be seen that the alloy set with Au underlayer (bottom row) dewets faster than that with Co underlayer (top row). Since CoAu is an immiscible sytem, the two layers can be assumed to dewet separately. It is thus expected that if the underlayer dewets earlier, the topography will be an additional driving force for the top film to dewet. In this case, Au dewets earlier than Co as shown in **Figure 5.6**.
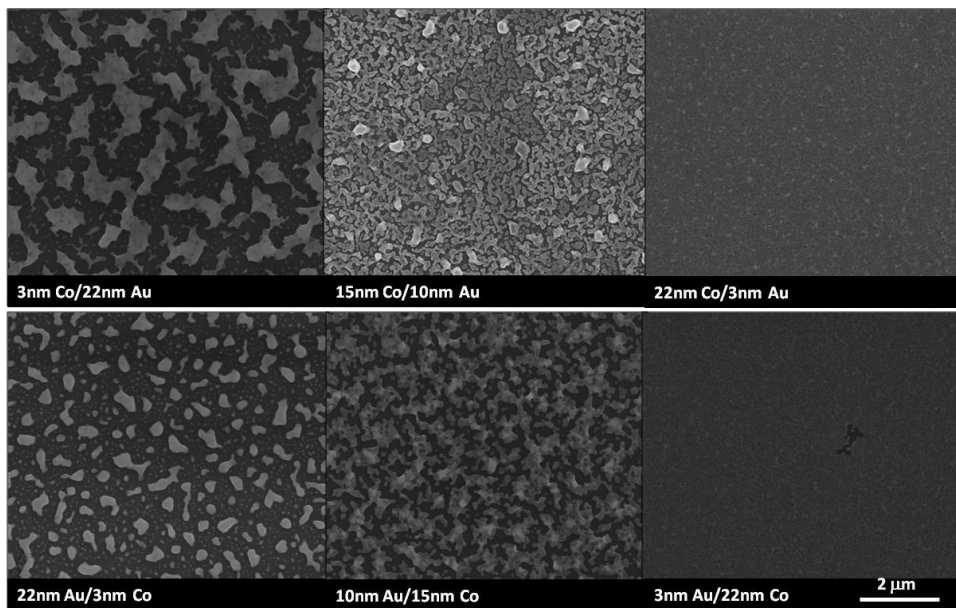
Figure 5.4: Morphologies of CoAu thin films after annealing at 500 ℃ for 15 minutes.
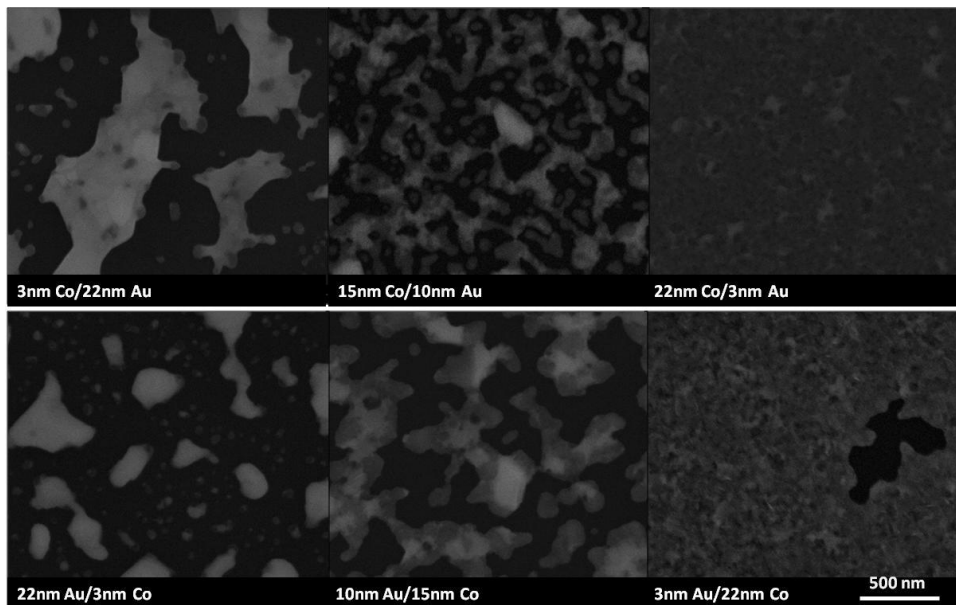
Figure 5.5: BSE images of CoAu thin films after annealing at 500 ℃ for 15 minutes.

Figure 5.5 shows corresponding BSE images of **Figure 5.4**. The bright part in the figure is Au and the darker part is Co. Under this annealing condition (500 ℃ for 15 minutes), the CoAu films with 22 nm Co were still in the hole initiation stage, and require higher temperature of 600 ℃ to form interconnected islands, as shown in **Figure 5.7.**

When the film starts to break, the larger islands can be Au or Co rich depending on its composition. For example, CoAu with 22 nm Au (**Figure 5.5**) produced Au-rich main islands while CoAu with 22 nm Co (**Figure 5.7**) yielded Co-rich main islands. However, independent of the composition, the smaller islands are generally always Co rich, as evident from the dark contrast in the BSE images (**Figure 5.5** and **Figure 5.7**).
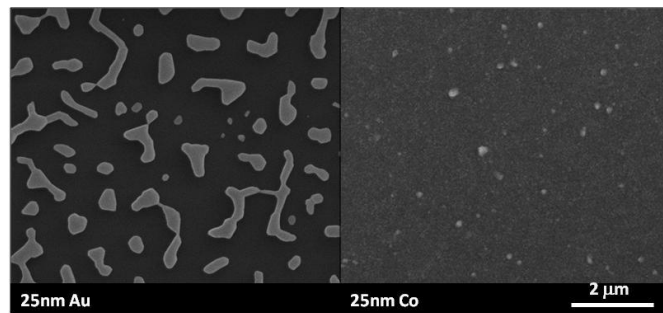
Figure 5.6: Morphologies of Au and Co thin films after annealing at 500 ℃ for 15 minutes.
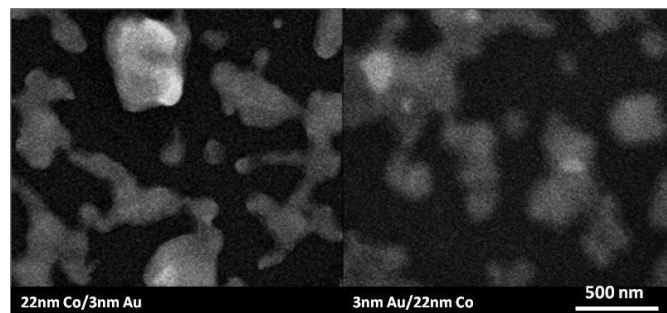
Figure 5.7: BSE images of 22nm Co/3nm Au and 3nm Au/22nm Co after annealing at 600 ℃ for 15 minutes.

The formation of two-phase particles as shown in **Figure 5.3** and **Figure 5.7** is noteworthy because of immiscibility between Au and Co, as shown in the phase diagram (**Figure 5.1**). At dewetting temperature, e.g. 800 ℃, solid solubility limit of Au in Co is ~ 1% and that of Co in Au is ~ 9%. However, as the temperature is brought back to room temperature, solid solubility will drop and the alloying can be weakened. However, the as-deposited films can already be readily bonded due to two possible reasons. First, both Au and Co are deposited in a high-vacuum environment so that adhesion between two clean surfaces is established.[113] Au and Co are polycrystalline in their as-deposited state. As a result, despite their high lattice mismatch, bonding between dangling bonds of the two is still possible with an associated semicoherent interfacial energy.[54] Second, any solid body within a small separation establishes an attractive force due to dipole-dipole interaction or VdW force.

Consider two materials A and B with surface energies γ_A and γ_B. If the two materials are joined, there will be a creation of new interface with energy γ_{AB}. Adhesion is favored if there is an energy benefit from destroying the two free surfaces of A and B. The energy difference is called work of separation according to,[87]

$$W_{sep} = \gamma_A + \gamma_B - \gamma_{AB}$$

Equation 5.1

W_{sep} for Au and Co on Al_2O_3 substrate have been calculated to be 0.86 and 1.19 J/m^2, respectively.[87] For the case of no adhesion, the Winterbottom construction will be reduced to Wulff construction for a free particle.[55] Despite their immiscibility, if we assume Au and Co form a semicoherent interface,

the interfacial energy is approximately 0.5 J/m^2. [54,114] In other words, there exists an adhesion energy between the two materials, which can be calculated using **Equation 5.1** to be 3.36 J/m^2 (assuming (100) planes of Au and Co form the joined interface). This means that even though Au and Co dewet separately, both materials are still attached to each other during dewetting, resulting in two-phase particles, as shown in **Figure 5.3b**.

5.5   Interparticle Spacing, Particle Density and Particle Size

Figure 5.8 summarizes interparticle spacing, particle diameter and particle density of Co, CoAu (69.8 at. % Co) and Au after annealing at 800 °C for two hours. As shown in the figure, interparticle spacing, particle diameter and particle density are material-dependent.

Unlike CoPd alloy which is a miscible system and behaves in between Co and Pd, CoAu alloy behavior is more difficult to predict. In **Figure 5.8a**, the average interparticle spacing of CoAu (15 nm Co and 10 nm Au or 69.8 at.% Co) is the smallest compared to that of Co and Au. **Figure 5.8b** shows that the average particle diameter follows the same trend as the interparticle spacing. This is expected due to volume conservation argument in that sparser particles should have larger volumes. The experimentally determined particle density is presented in **Figure 5.8c**. The large scatter bar presented in **Figure 5.8a** and **b** is due to the fact that the film is not patterned. [10,27]
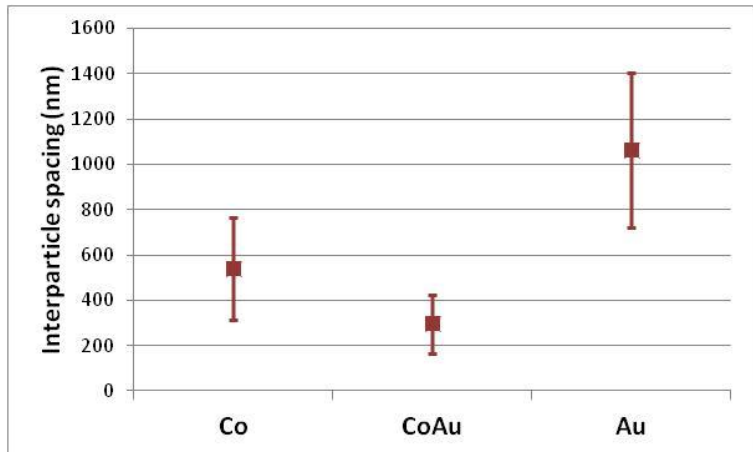
(a)
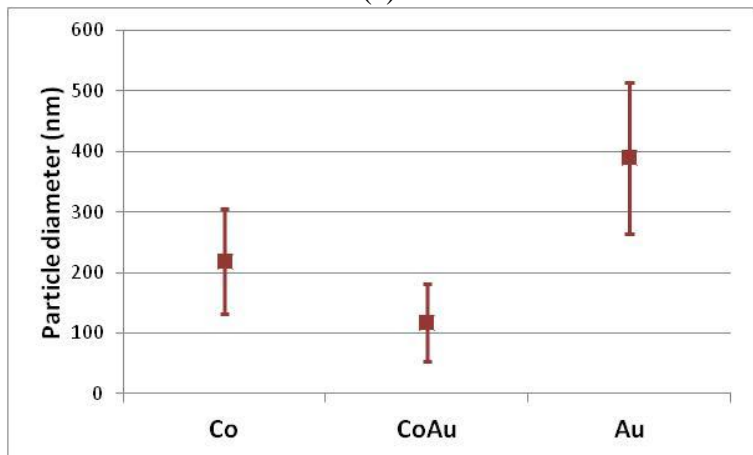
(b)
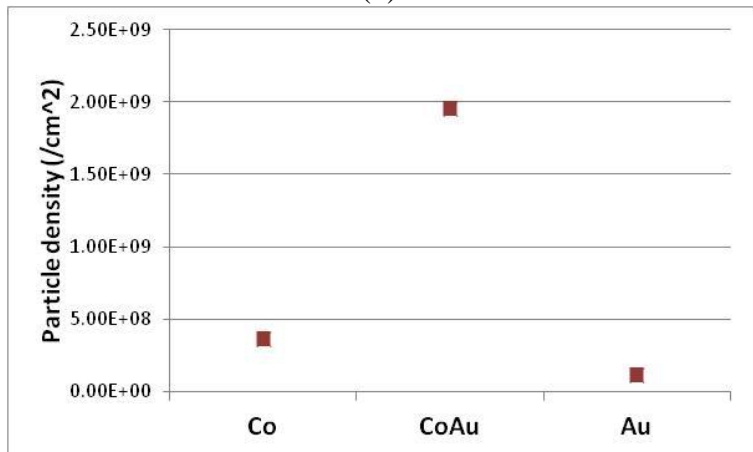
(c)

Figure 5.8: (a) Average interparticle spacings, (b) average particle diameter and (c) particle density for Co, CoAu (69.8 at.% Co) and Au after annealing at 800 ℃ for two hours.

Layer Configuration	Dewetting Scenario → time
3-nm Co/ 22-nm Au	
22-nm Au/ 3-nm Co	
15-nm Co/ 10-nm Au	
10-nm Au/ 15-nm Co	
22-nm Co/ 3-nm Au	
3-nm Au/ 22-nm Co	
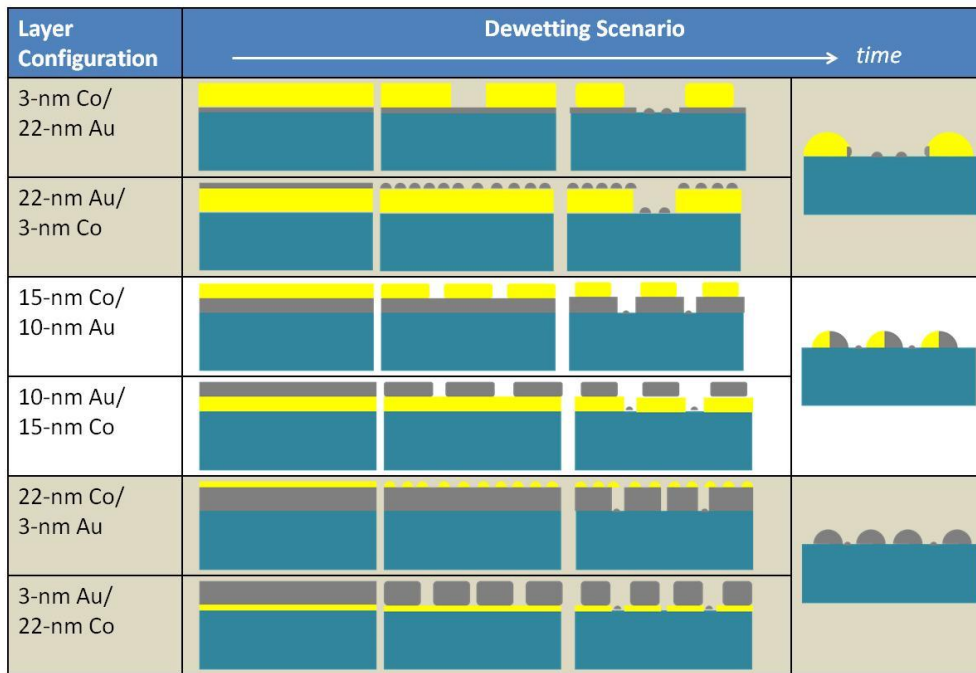
LEGEND Al$_2$O$_3$ Co Au

Figure 5.9: Schematics of different dewetting schemes for various CoAu thicknesses and layer configurations.

(a)

(b)
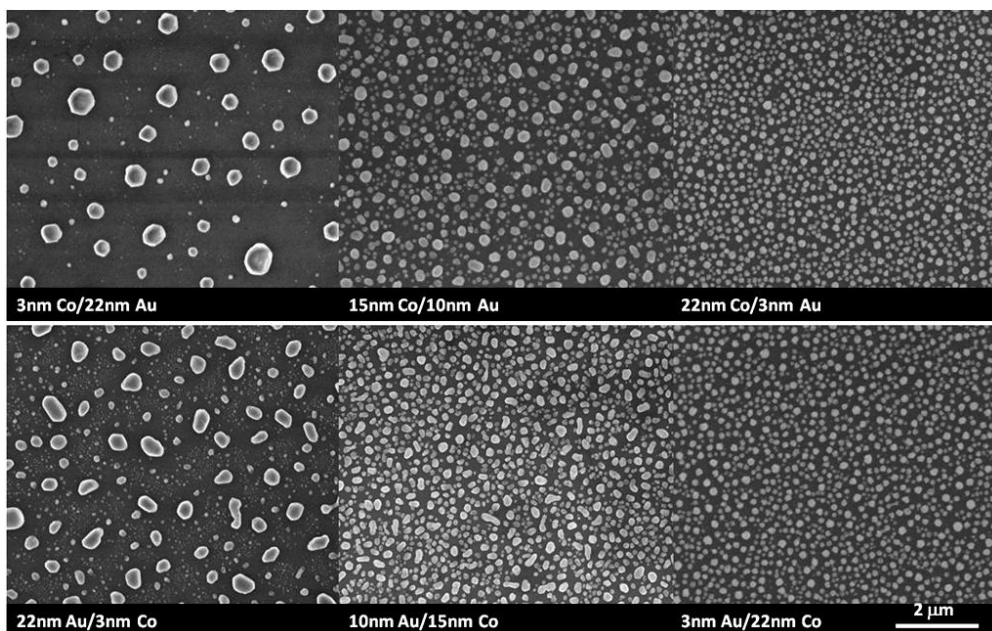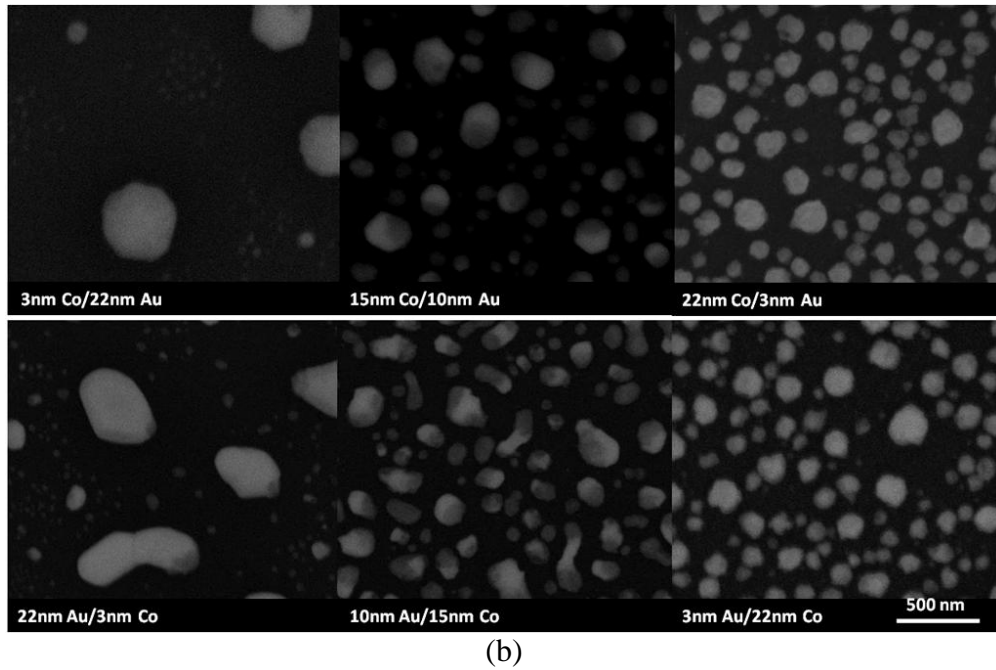
Figure 5.10: (a) Morphologies of CoAu thin films after annealing at 800 ℃ for 2 hours. (b) BSE images of CoAu thin films after annealing at 800 ℃ for 2 hours.

Figure 5.9 illustrates the different dewetting scenarios for different thicknesses and layer configurations of the CoAu system. At this point, the following three distinct morphologies can be made, namely A (predominantly Au-rich with Co-rich segment), B (Co-rich), and C (balanced Au-rich and Co-rich segments). Three possible scenarios can then be classified as follows:

1. A and small B particles.

   For thin Co/thick Au, Au starts to dewet until the Co surface is exposed, after which the Co film will begin to dewet as well. Treated separately, Au and Co dewet into particles with a range of sizes due to their not being patterned. Au, being thicker, will form particles with a broader range of sizes, comprising small and large ones. Meanwhile, Co will form mainly small particles with a narrower size distribution. When combined, the larger Au particle and the small Co particle will form particle A. On the

other hand, the small Au particles will join the small Co particles, but will evaporate during the annealing, leaving behind particle B. Similar argument applies for thick Au/thin Co layer configuration. The final result for both is a mixture of A and small B particles.

2. C and small B particles.

   This occurs for the case of comparable Co and Au thickness. Each layer dewets separately while maintaining good bonding due to adhesive energy and VdW interaction between them, as explained earlier. As before, the particle size will be in a range of sizes. The larger particles are of type C while the smaller ones are of type B due to enhanced evaporation of the Au portion. The final result is a mixture of C and small B particles.

3. Large and small B particles.

   This occurs for the case of thick Co/thin Au and thin Au/thick Co. Each layer dewets separately forming large and small Au/Co particles. The Au portion evaporates, leaving behind small and large B particles.

It can be seen that the final morphology of the CoAu film is dependent on thickness, but independent of layer configuration.

The SEM images for different compositions of CoAu alloy after annealing at 800 °C for two hours are shown in **Figure 5.10a**. Overall trend for interparticle spacings, particle size and particle density is difficult to observe. The SEM images of Co and Au annealed at the same conditions are shown in **Figure 5.11** as a comparison. **Figure 5.10b** shows corresponding BSE images of **Figure 5.10a.** The bright area shows Au-rich region while the darker area shows Co-rich region. For 3 nm Co/22 nm Au and 22 nm Au/3 nm Co, the dewetted particles can be grouped into large Au-rich particles and small Co-

94

rich particles. For 15 nm Co/10 nm Au and 10 nm Au/15 nm Co, there are two phases in a single particle. However, for 22 nm Co/3 nm Au and 3 nm Au/ 22 nm Co, there is no observable contrast, indicating that during the annealing process the Au-rich part were evaporated and left with Co-rich particles. These observations in **Figure 5.10** agree well with the dewetting scenarios proposed in **Figure 5.9**.
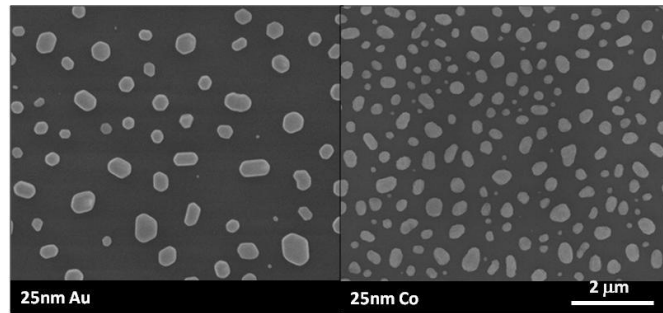
Figure 5.11: Morphologies of Au and Co thin films after annealing at 800 ℃ for 2 hours.

Table 5.1: Calculation of atoms evaporated during annealing at 800 ℃ for 2 hours for 3 nm Au and 3 nm Co. Sample size is 0.5 cm x 0.5 cm.

Material	ρ (g/cm³)	M_W (g/mol)	P_{eq} (Torr)	R_e (atoms/cm².s)	# Atoms evaporated	# Atoms available	% Volume remaining
Au	19.3	197	3 x 10⁻⁸	2.3 x 10¹²	4.1 x 10¹⁵	4.4 x 10¹⁵	6.8
Co	8.9	59	~ 1 x 10⁻⁹	1.4 x 10¹¹	2.5 x 10¹⁴	6.8 x 10¹⁵	96.3

A very thin Au film (3 nm) is expected to form only small part of the dewetted CoAu particles. As the desorption of Au is significant at elevated temperature,[10] a very thin Au film (3 nm) is expected to desorb completely. The evaporation rate (R_e) of atoms can be estimated by Langmuir equation[115]:

$$R_e = (3.513 \times 10^{22})(M_W T)^{-\frac{1}{2}} P_{eq,T}$$

Equation 5.2

where M_W is the molar mass of the atom (g/mol), T is the annealing temperature (K) and $P_{eq,T}$ is the equilibrium vapor pressure at T. Data for $P_{eq,T}$ is taken from the work of Honig.[116] **Table 5.1** shows the calculation for the

95

atoms evaporation process during annealing at 800 ℃ for 2 hours. As can be seen, significant amount of Au atoms has evaporated from 3 nm Au with only 6.8 % volume left while for the same thickness, the % volume remaining for Co is still as high as 96.8. It is therefore expected that in the case of CoAu alloy with 3 nm Au, the Au component has almost completely evaporated after the annealing. This is supported by the observation in **Figure 5.10b** where all the particles seem to be composed mainly of Co. While for the case of CoAu alloy with 3 nm Co, small Co nanoparticles are still observable after annealing due to the nominal amount of evaporated Co atoms.

Since Co and Au are immiscible, we may treat Co-rich and Au-rich particles separately. This is clearly illustrated in the case of 3 nm Co/22 nm Au and 22 nm Au/3 nm Co, where the particle distribution consists of small particles which are Co-rich and larger particles which are Au-rich. **Figure 5.12** shows that the large particles are faceted and are surrounded by smaller Co-rich particles with the dotted line indicating the trace of a dewetted Au patch. This suggests that during dewetting, separation of Co-rich material and Au-rich material already took place before particle formation. Thus, we may estimate the interparticle spacing and particle density for Au-rich particles and Co-rich particles separately.

From **Figure 5.11**, average interparticle spacings for 25 nm Au thin film and 25 nm Co thin film after annealing at 800 ℃ for 2 hours are ~1060 nm and ~540 nm respectively. Interparticle spacing is proportional to initial film thickness.[31] Thus, interparticle spacings for other thicknesses of Au and Co thin films can be predicted as given in **Table 5.2**. **Figure 5.12a**, **b** and **c** show

that the measured interparticle spacings for 22 nm Au/3 nm Co, 3 nm Co/ 22 nm Au and 10 nm Co/15 nm Au match the estimated values.

Table 5.2: Estimated interparticle spacings of Au and Co for various thicknesses.

Film thickness (nm)	Estimated spacing – Au (nm)	Estimated spacing – Co (nm)
3	130 ± 40	70 ± 30
10	430 ± 140	220 ± 90
15	630 ± 210	320 ± 130
22	940 ± 300	470 ± 200
25	1060 ± 340	540 ± 220
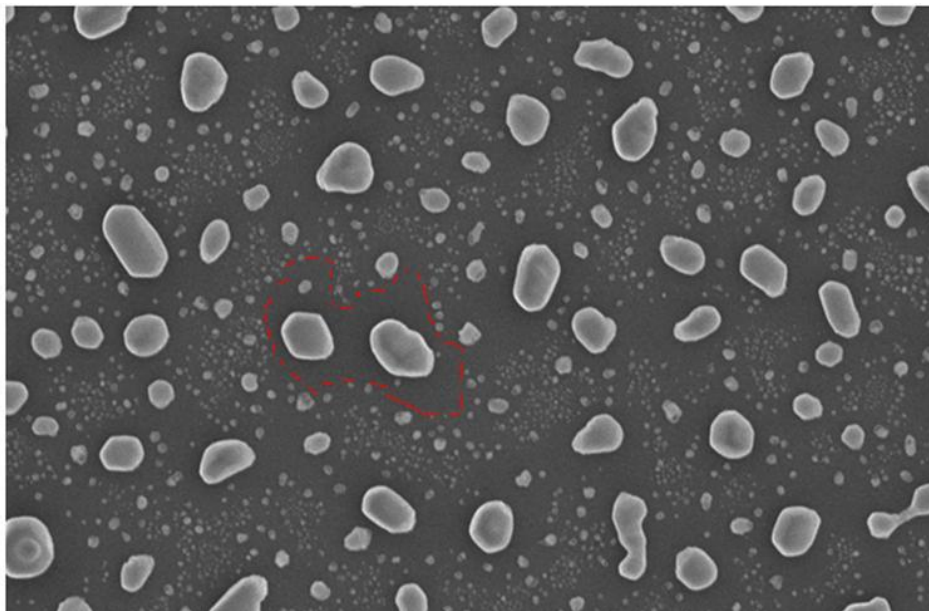
Material	Predicted (nm)	Measured (nm)
Co	70 ± 30	60 ± 20
Au	940 ± 300	850 ± 260

22nm Au/3nm Co   2 μm

(a)

Material	Predicted (nm)	Measured (nm)
Co	70 ± 30	70 ± 30
Au	940 ± 300	910 ± 400

3nm Co/22nm Au   2 μm

(b)

Material	Predicted (nm)	Measured (nm)
Co	220 ± 90	120 ± 30
Au	630 ± 210	530 ± 190

10nm Co/15nm Au   2 μm
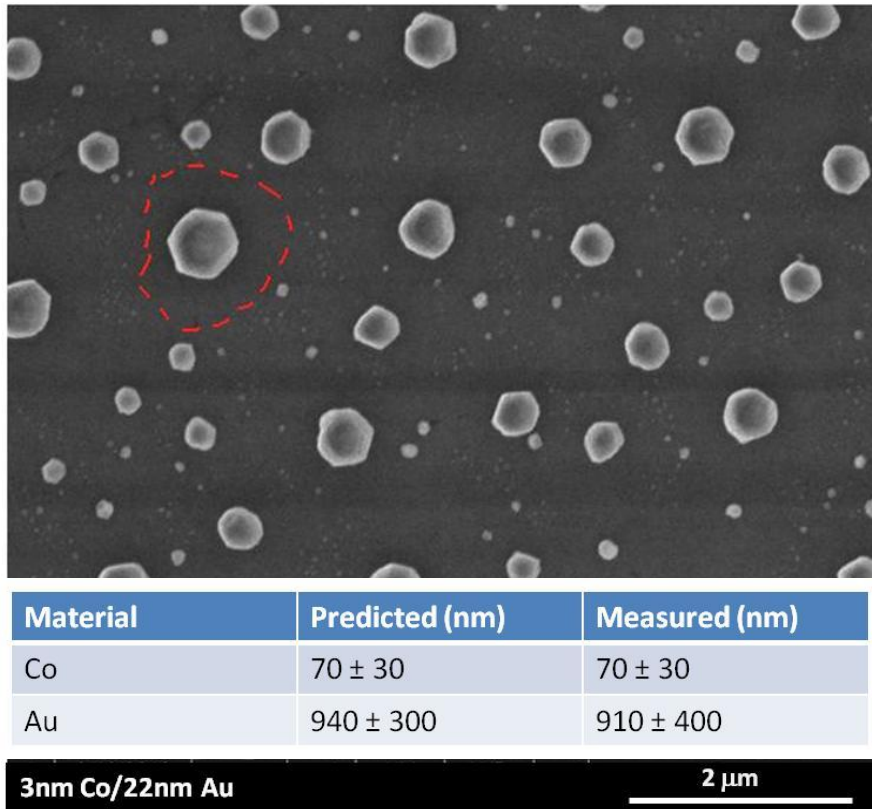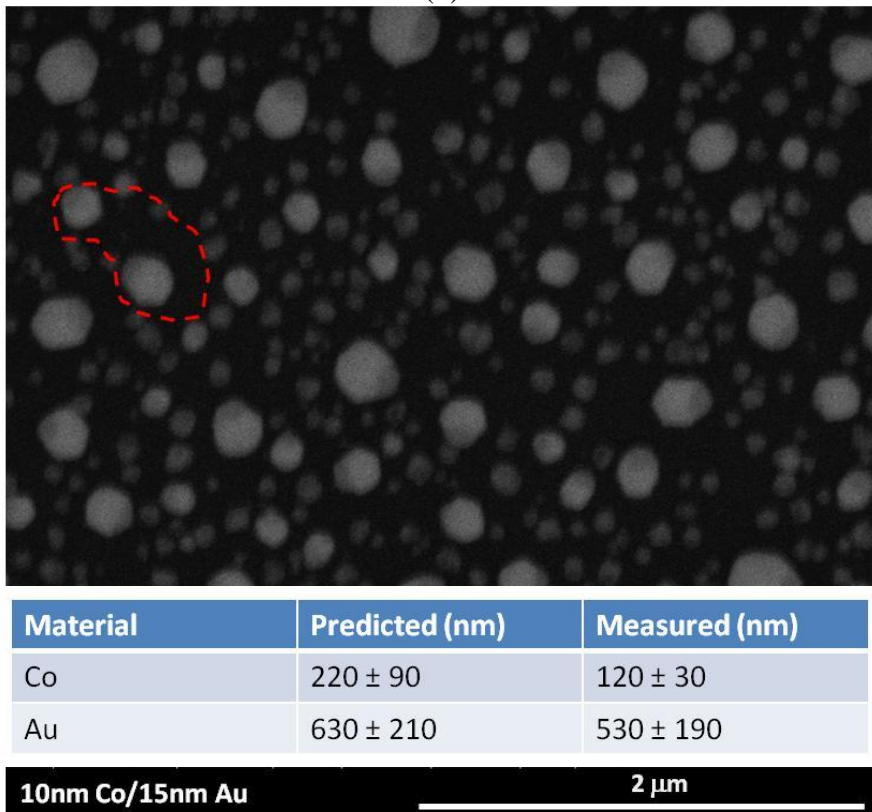
(c)

Figure 5.12: (a) 22 nm Au/3 nm Co and (b) 3nm Co/ 2 nm Au after annealing at 800 ℃ for 2 hours. The dotted line demarcates the trace of dewetted Au patch. The scale bar is 2 μm.

Figure 5.12a, **b** and **c** also show that the small Co-rich particles are separated in clusters by the Au-rich particles. Thus, it is possible to create clusters of nanoparticles array without resorting to lithography. We may be able to further tune the spacing and size of clusters by varying the thickness of each layers of the CoAu film. These clusters of nanoparticles may find application in Raman imaging[117,118] or as sensors for DNA, heavy metal ions and proteins.[119]

For 15 nm Co/10 nm Au and 22nm Co/3 nm Au, it is difficult to differentiate between Co-rich particles and Au-rich particles. Clear difference between Co-rich and Au-rich particles can only be observed in CoAu alloy with high Au composition (Au-to-Co volume ratio $\geq$ 1.5) as shown in **Figure 5.12**. For these figures, the predicted interparticle spacings match the measurement.

We can also estimate the particle density as:

$$D = \frac{1}{a^2}$$

where $a \propto h$ [29], so that we can write,

$$D \propto \frac{1}{h^2}$$

$$D = \left(\frac{25}{h}\right)^2 D_0$$

Equation 5.3

where D is particle density, a is average interparticle spacing, h is initial film thickness, and D_0 is particle density for film thickness of 25 nm, which is determined from our experiment. The estimated particle density of Au and Co for different initial film thicknesses is listed in **Table 5.3**.

Table 5.3: Estimated particle density of Au and Co for different initial film thickness.

Film thickness (nm)	Estimated density – Au (cm^{-2})	Estimated density – Co (cm^{-2})
3	7.7×10^9	2.5×10^{10}
10	6.9×10^8	2.3×10^9
15	3.1×10^8	1.0×10^9
22	1.4×10^8	4.7×10^8

Table 5.4 shows the calculated particle densities of CoAu alloy, which roughly match the estimated values. For CoAu alloy with distinguishable Co-rich and Au-rich particles, the particle density can be calculated separately. For CoAu alloy with larger Co composition (22 nm Co and 15 nm Co), the particle density is calculated by taking the overall particles and the estimation value is obtained by adding up the particle density of Co and Au for the respective thicknesses.

Table 5.4: Measured particle density of CoAu alloy. Estimated value is given for comparison.

Film	Density (cm^{-2})	Estimated Density (cm^{-2})
3 nm Co/ 22 nm Au	Au = 1.4×10^8 Co = 1.2×10^{10}	Au = 1.4×10^8 Co = 2.5×10^{10}
10 nm Co/ 15 nm Au	Au = 1.4×10^8 Co = 4.7×10^9	Au = 3.1×10^8 Co = 2.3×10^9
15 nm Co/ 10 nm Au	2.0×10^9	1.7×10^9
22 nm Co/ 3 nm Au	3.6×10^9	8.2×10^9
22 nm Au/3 nm Co	Au = 2.3×10^8 Co = 5.6×10^{10}	Au = 1.43×10^8 Co = 2.51×10^{10}
10 nm Au/15 nm Co	3.9×10^9	1.7×10^9
22 nm Co/ 3 nm Au	4.4×10^9	8.2×10^9

5.6 TEM Studies

TEM study was performed to examine the microstructure of the films and the nanoparticles at a higher magnification than SEM as well as to do

compositional EDX analysis. **Figure 5.13a** and **b** show TEM images of CoAu alloy (69.8 at.% Co) after annealing at 800 ℃ for 2 hours. As can be seen, the larger particles commonly consist of bright and dark areas. The dark area here corresponds to Au and the bright area corresponds to Co as opposed to the contrast in BSE images. In the bright field imaging, lighter material (small Z) scatters the incoming electrons to smaller angle.[82] Consequently, more electrons will reach the detector resulting in the bright image. Most of the particles are faceted. Besides the high angle grain boundaries, some twinnings can also be observed.

It is interesting to note that the smaller particles are rich in Co. As shown earlier in **Figure 5.8b**, Co particles are smaller in size compared to Au particles dewetted from the same film thickness. Since each layer dewets independently for the CoAu system, the smaller particles are expected to come from the Co counterpart. Since solid solubility limit of Au in Co is very limited (~1% at 800 ℃) compared to Co in Au (~9 % at 800 ℃), as dictated by the Co-Au phase diagram[110], these small particles are expected to be rich in Co and no significant 'alloying' was observed. EDX measurement confirms that the small bright particles are Co-rich with Co concentration ~99%.

EDX measurement was also performed on the particles which show different contrast. **Figure 5.14** shows the EDX line-scan and EDX mapping results of such particle. As can be seen from the EDX line-scan, the region with darker contrast is Au-rich with Au concentration ~ 87% and the region with brighter contrast is Co-rich with Co concentration ~ 99%. Co is incorporated more into the Au-rich region and not the opposite, because of

larger solid solubility limit of Co in Au compared to Au in Co, as explained earlier.
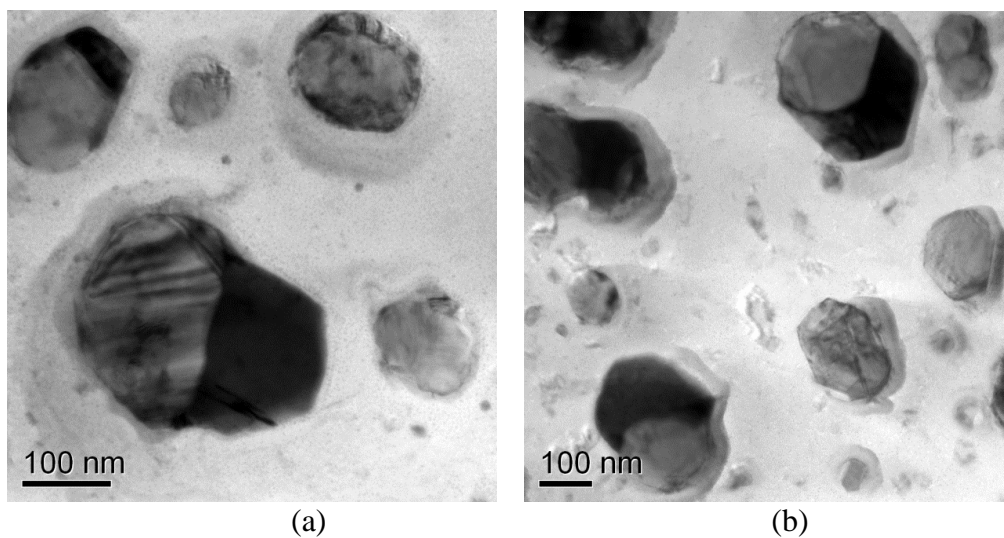
Figure 5.13: (a) and (b) CoAu (69.8 at.% Co) alloy after annealing at 800°C for 2 hours.
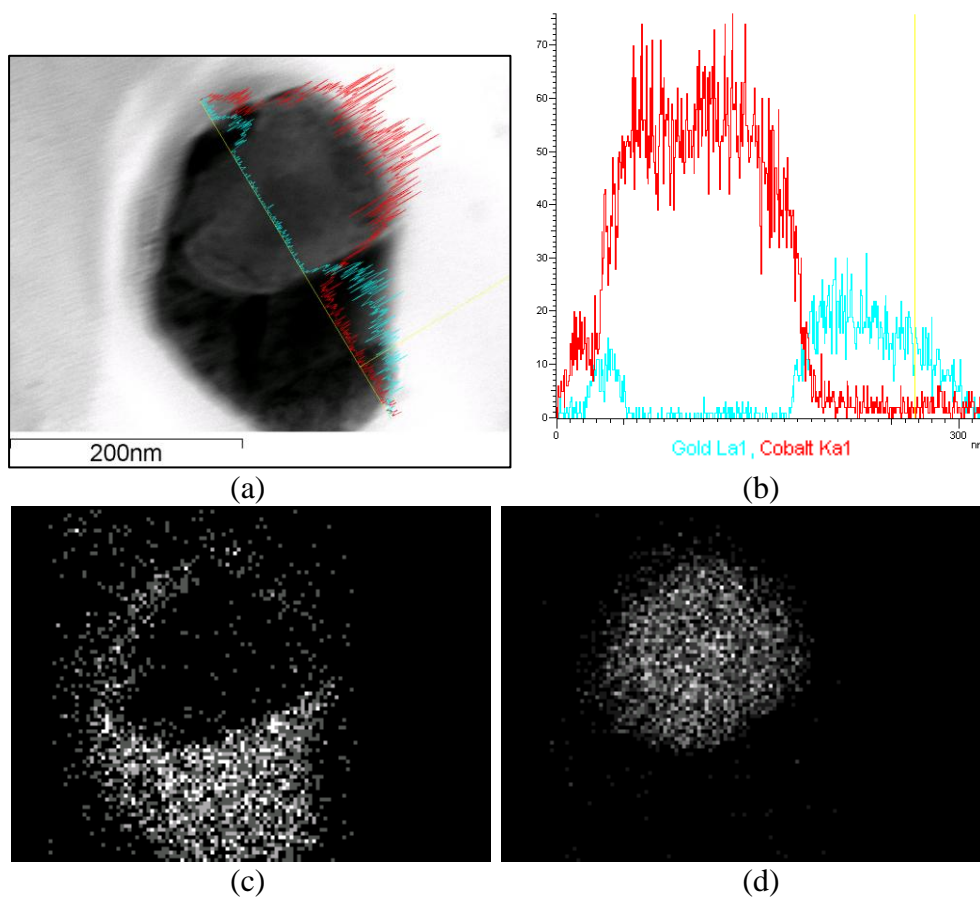
Figure 5.14: (a) CoAu nanoparticle, (b) the corresponding EDX line-scan, (c) Au-element EDX mapping, and (d) Co-element EDX mapping. Scale bar for (a) is 100 nm.

102

5.7 Summary

This work has provided a better understanding of solid-state dewetting mechanism of CoAu alloy, which is an immiscible system. We have established that CoAu alloy undergoes similar stages of dewetting as miscible alloy and elemental materials. We found that interstage transition and dewetting morphology depend on alloy composition. For the same composition, Au underlayer will give faster dewetting rate compared to Co underlayer. We have characterized the morphology of dewetted particles in terms of interparticle spacing, particle density, and particle size, and for CoAu, they were found not to lie between its parent materials. Dewetted CoAu flm forms two separate phases. Three possible scenarios were proposed to distinguish the dewetting morphologies for different Au/Co thickness ratio. For CoAu alloy with high Au composition (Au-to-Co volume ratio $\geq$ 1.5), Au-rich particles and Co-rich particles are distinguishable and thus, they can be treated separately. We are able to predict the interparticle spacings and particle densities for both Au-rich and Co-rich particles. For this range of composition, we demonstrated the possibility to create clusters of nanoparticles array without resorting to lithography. We may be able to further tune the spacing and size of clusters by varying the thickness of each layers of the CoAu film. These clusters of nanoparticles may find application in Raman imaging[117,118] or as sensors for DNA, heavy metal ions and proteins.[119] The EDX results show that Au incorporation into Co-rich region is only about ~1% and Co incorporation into Au-rich region is about ~ 13% which is close to the value predicted by the Co-Au phase diagram.

Chapter 6. Magnetic Properties of CoPd and CoAu

Nanoparticles

6.1 Introduction

Magnetic metal nanoparticles arrays have gained considerable interest for applications in high density information storage,[120,121] sensor technology[122,123] and as catalysts for carbon nanotube growth[124,125]. Cobalt is one of the widely used materials in information storage industry due to its uniaxial anisotropy (7×10^6 erg/cm^3) at room temperature.[126] Crystallographic structures of Co at room temperature is hexagonal close-packed (hcp) which changes at 450 ℃ to a face-centered cubic (fcc) form.[127] Fcc Co is approximately ten times lower in anisotropy compared to hcp Co.[128]

In Chapter 4 and Chapter 5, we have presented systematic studies on CoPd and CoAu nanoparticles formation by solid-state dewetting. This low-cost method produces arrays of nanoparticles with a range of sizes and spacings. Alloying of Co with other materials is common to improve the properties. For example, Oh et al. demonstrated that CoPt alloy can produce L1$_0$ particles with strong magnetocrystalline anisotropy and out-of-plane (OOP) easy axis.[18] In comparison, Co nanoparticles array by solid-state dewetting have mostly fcc phase with little anisotropy.[29]

During the dewetting process, crystallographic structures and magnetic properties changes with temperature. In this chapter, we investigate the magnetic properties of the CoPd and CoAu nanoparticles after dewetting at 800 ℃ in terms of the geometry, phase transformations, and crystal structure

of the CoPd and CoAu nanoparticles, and compared them to as-deposited films.

6.2 Experimental Details

p-type Si (100) wafers were used as substrate for the dewetting experiments. The wafers were covered with resist and cut into 0.5×0.5 cm^2 chips. The resist protected the substrate from debris generated during dicing. The samples were then cleaned in acetone for 30 minutes to remove the resist followed by immersing in IPA for 5 minutes and rinsing with DI water. For the next step, 100-nm Al_2O_3 layer was sputter-deposited on the Si wafer, serving as a silicidation barrier. Afterwards, 25-nm of Co, CoPd (15 nm Co/10 nm Pd) and CoAu thin films (15 nm Co/10 nm Au) were sputter-deposited.

The samples were loaded into a furnace in forming gas ambient (10% H_2) with 1800 sccm flow rate. The furnace was then heated up with a ramp rate of about 20 ℃/minute to the setpoint temperature. It takes 1-2 minutes before the temperature stabilizes. After maintaining the setpoint temperature for the desired duration, the furnace was subsequently cooled down to room temperature, which takes approximately 4 hours, before the samples were retrieved. The sample morphology after annealing was characterized using SEM (FEI Nova NanoSEM 230) and TEM (JEOL 2010F and JEOL3010). Composition analysis was carried out using EDX (INCA x-sight detector). Magnetic measurements were made with a vibrating sample magnetometer LakeShore 7404 (up to 10 kOe).

6.3   Magnetic Properties of Deposited Films

In a thin film, shape anisotropy generally dominates, leading to an easy plane of magnetization along the plane of the film and a hard plane of magnetization along the growth direction of the film, as can be seen in **Figure 6.1**.[128,129] Magnetostatic energy (E_{MS}) is stored in the magnetic field according to,[130]

$$E_{MS} = \frac{1}{2\mu_0} \int_{all\ space} B^2 dV$$

Equation 6.1

This equation implies that the left configuration in **Figure 6.1** resulted in a high magnetostatic energy due to the dense field lines. The right configuration only has the magnetic field mostly confined at the edges of the thin film and results in low magnetostatic energy.

Magnetic anisotropy total energy, for a film with uniaxial anisotropy oriented perpendicular to the plane, can be expressed in its simplest form as[128]:

$$E_{tot} = (-2\pi M_s^2 + K_1)sin^2\theta_M$$

Equation 6.2

where the quantity $-2\pi M_s^2$ is the macroscopic shape anisotropy term that strongly favors in-plane (IP) magnetization, K_1 is the first-order magnetocrystalline anisotropy parameter and θ_M is the angle between the magnetization and the sample surface normal. Only when the magnetocrystalline anisotropy is stronger than the shape anisotropy, the easy plane of magnetization will be perpendicular to the film plane.

High Energy   Low Energy
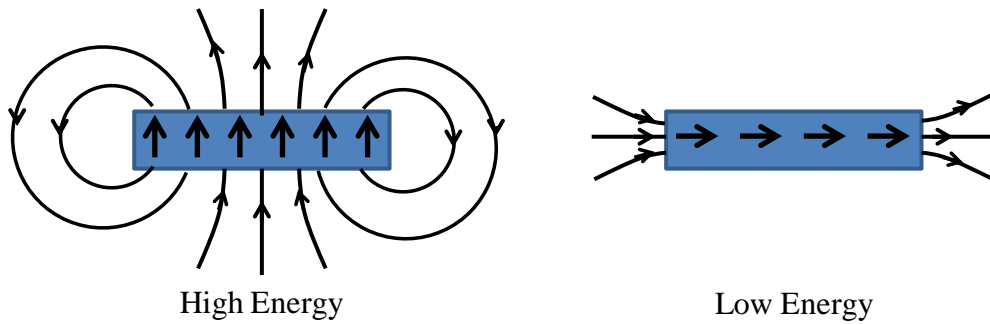
Figure 6.1: Magnetostatic field lines in a thin film for high-energy and low-energy configurations. Shape anisotropy in thin film always favors an in-plane magnetization (arrow=magnetization).

Figure 6.2 shows the in-plane magnetic hysteresis loop measured at ambient temperature for as-deposited 25-nm-thick films of Co, CoPd and CoAu on a smooth Al_2O_3 substrate. The as-deposited film shows the expected strong in-plane magnetic anisotropy which is expected due to the shape of thin film (hard axis saturation field > 10 kOe as shown in **Figure 6.3**). The in-plane loop shows that the saturation magnetization M_s is close to that of bulk Co (1400 emu cm^{-3}). The in-plane coercivity is ~100 Oe, which means we need to apply this value of magnetic field to totally demagnetize the material, with remanence close to 1100 emu cm^{-3}.
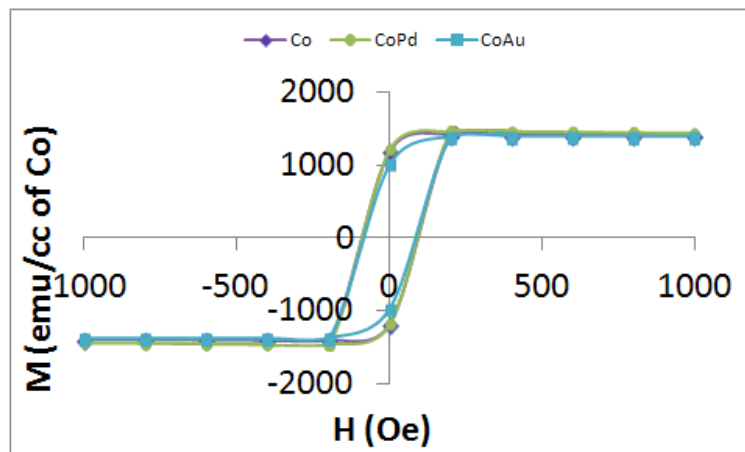
Figure 6.2: In-plane magnetic hysteresis loops from as deposited 25-nm-thick Co, CoPd and CoAu films.
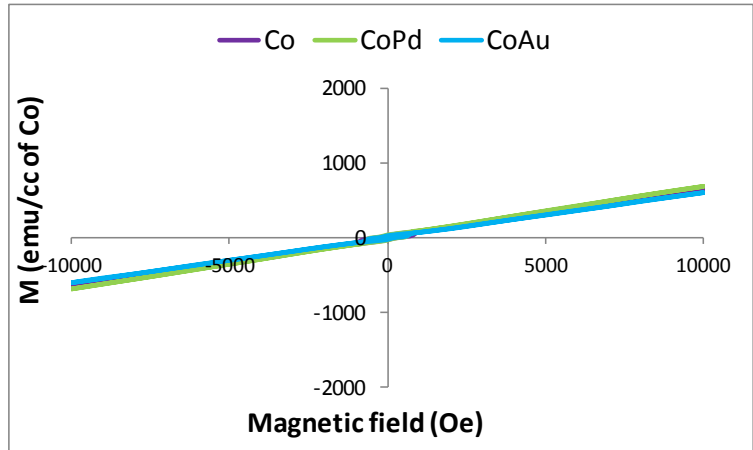
Figure 6.3: Out-of-plane magnetic hysteresis loops from as deposited 25-nm-thick Co, CoPd and CoAu films.

It is also observed that for both in-plane (**Figure 6.2**) and out-of-plane (**Figure 6.3**) directions, the magnetic hysteresis loops are identical for Co, CoPd, and CoAu, indicating that only Co contributes to the magnetic signal. CoPd and CoAu films are deposited sequentially and there is no intermixing between the two dissimilar materials at room temperature.

6.4   Magnetic Properties of CoPd Nanoparticles

To create CoPd nanoparticles, the thin film was annealed at 800 °C for 2 hours in forming gas ambient (10% H_2). The SEM image of CoPd nanoparticles is shown in **Figure 6.4**. The SEM image of Co nanoparticles is also shown for comparison. **Figure 6.5** shows the in-plane and out-of-plane magnetic hysteresis loops for both nanoparticles.
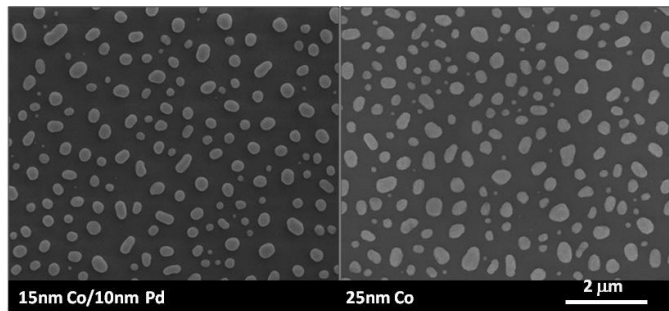
Figure 6.4: SEM images of CoPd and Co thin films after annealing at 800 °C for 2 hours in forming gas ambient.

As can be seen from **Figure 6.4**, the dewetted nanoparticles have nearly spherical shapes and vary in size and distribution. The SAED result of CoPd thin film after annealing in **Section 4.7**, also shows the presence of fcc phase. Furthermore, TEM results show that not all of the particles are single crystalline and some twinnings are observed. As a result, the magnetic hysteresis loops of dewetted Co and CoPd nanoparticles show reduced anisotropy (**Figure 6.5**). This result is consistent with the work of Oh et al.[29] which shows low anisotropy fcc phase in Co particles after annealing. Both CoPd and Co show vanishing coercivity after annealing. This is expected because after annealing, the particles adopt spherical shape and fcc crystal structure so that the magnetization is easy to change, i.e. they become soft ferromagnets. Superparamagnetic effect is not expected because the particle size is larger than 100 nm, while the superparamagnetic limit is generally below 10 nm.[131,132]

As can be seen in **Figure 6.5**, after annealing, CoPd nanoparticles exhibit smaller saturation field as compared to Co. Magnetic response of a material is determined by three dominant anisotropies, namely shape, magnetocrystalline, and magnetoelastic. Since both CoPd and Co nanoparticles are spherical in shape and adopt fcc crystal structure, the difference in the magnetic response should be caused by the magnetoelastic effect. Magnetoelastic energy is given by,[133]

$$E_\sigma = \frac{3}{2} \lambda_{MS} \sigma sin^2 \theta_{MS}$$

Equation 6.3

where λ_{MS} is the magnetostriction constant, σ is the uniaxial stress applied along a certain direction, and θ_{MS} is the angle between the magnetization and the stress direction. Comparing the lattice constants of Pd (3.889 Å)[134] and Co (5.057 Å)[135], it can be seen that compressive stress is applied to the Co atoms in the CoPd alloy system. Since Co has negative magnetostriction constant,[136] the magnetoelastic energy as given in **Equation 6.3** is minimized in the direction of applied compressive stress (because the product of λ_{MS} σ is positive). Consequently, it is easier to saturate the magnetization along this direction. **Figure 6.5** indeed shows that the required magnetic field to saturate the magnetization decreases (from 4 kOe to 3 kOe for IP direction and from 9 kOe to 6 kOe for OOP direction) for CoPd as compared to Co.

For Co after annealing, the saturation magnetization is reduced to ~ 1250 emu cm^{-3}, which is about 10% reduction as compared to that of as-deposited Co film. This decrease can be attributed to post-annealing oxidation. For 25-nm Co film, the nanoparticles formed through dewetting process have an average diameter of ~ 200 nm. Assuming the particle shape is hemispherical with radius r, the grown oxide thickness (δ) to account for the 10% reduction in M_s can be calculated as follows,

$$\frac{\Delta Volume}{Volume} = 0.10$$

$$\frac{2\pi r^2 \delta}{\frac{2}{3}\pi r^3} = 0.10$$

$$\delta = \frac{0.10r}{3} \sim 3nm$$

At room temperature, oxidation of bulk Co saturates at an oxide thickness of ~ 1 nm.[137] However, enhanced room-temperature oxidation in nanoparticles has been reported with the oxide thickness reaching ~ 3 nm.[138]
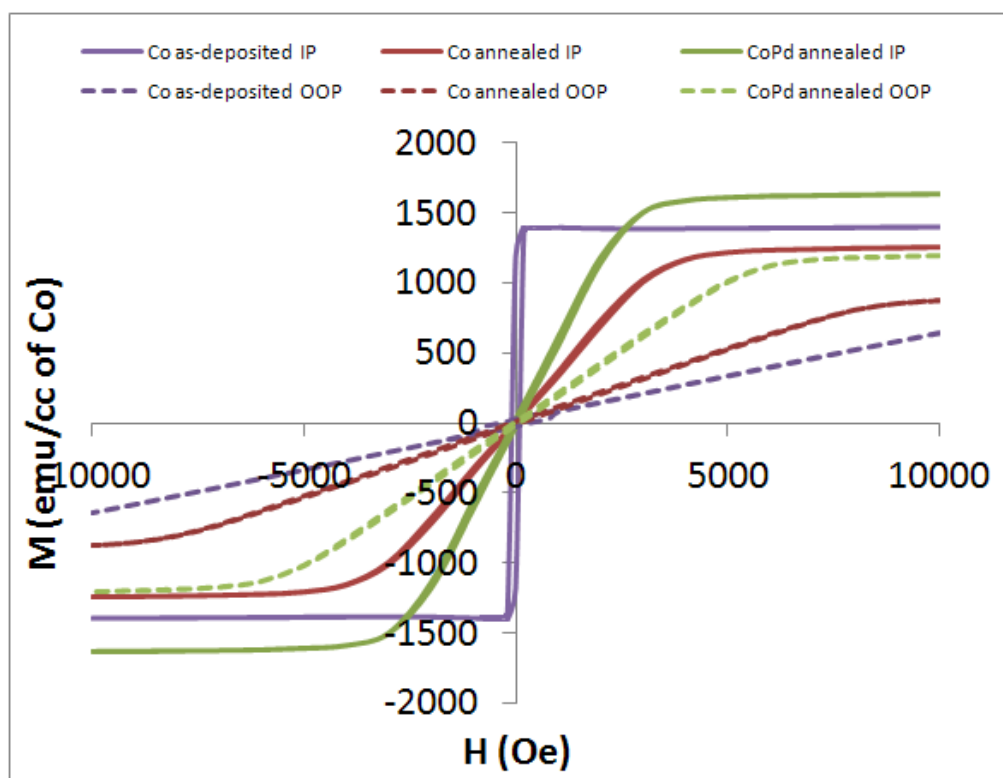
Figure 6.5: In-plane and out-of-plane magnetic hysteresis loops from CoPd and Co nanoparticles. The magnetic hysteresis loop from as-deposited Co is also shown as a comparison.

For CoPd alloy, M_s value is consistent with other reports which found that the M_s per volume of the alloy decreases as compared to pure Co case.[139,140] However, the M_s value actually increases if calculated per Co atom only[139,141-143], as can be seen in **Figure 6.5**. The inclusion of Pd seems to improve the resistance to oxidation. However, this alone cannot explain the increase in M_s. It was argued that strong exchange interaction between the 4d electrons of Pd and the localized 3d electrons on the Co polarizes the Pd atoms. Thus, the Pd atoms also contribute to the total M_s.[108,139]

Table 6.1: Comparison of saturation moment of CoPd alloy from our experiment and Bozorth *et al.*'s work.[139]

Reference	Ms of Co (emu/cc)	Ms of 66.7 at.% CoPd per CoPd atom (emu/cc)	Ms of 66.7 at.% CoPd per Co atom (emu/cc)	% Increase in Ms per atom Co
Our work	1400	1000	1650	18
Bozorth *et al.*	1430	1180	1690	18

6.5   Magnetic Properties of CoAu Nanoparticles

To create CoAu nanoparticles, the thin film was annealed at 800 °C for 2 hours in forming gas ambient (10% H_2). The SEM image of CoAu nanoparticles is shown in **Figure 6.6**. The SEM image of Co nanoparticles is also shown for comparison. **Figure 6.7** shows the in-plane magnetic hysteresis loops for both nanoparticles.

15nm Co/10nm Au   25nm Co   2 µm
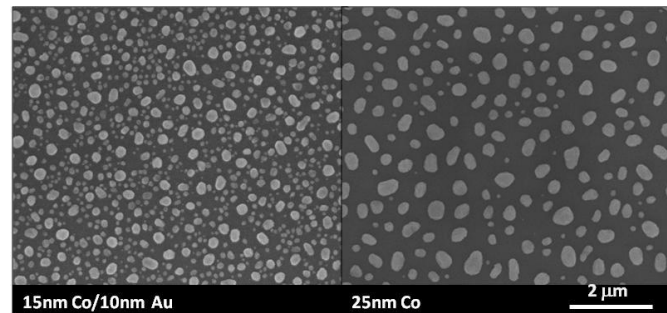
Figure 6.6: SEM images of CoAu and Co thin films after annealing at 800 °C for 2 hours in forming gas ambient.

As can be seen from **Figure 6.6**, the dewetted nanoparticles have nearly spherical shapes and vary in size and distribution. Magnetic hysteresis loops of CoAu nanoparticles show low anisotropy and vanishing coercivity with similar shape to Co nanoparticles loop (**Figure 6.7**). This is expected because Co-Au is an immiscible system and Co is transformed into fcc phase after annealing and is consistent with the work of Oh et al.[29]

The only difference from Co and CoAu nanoparticles loops is that for CoAu, the saturation magnetization is further reduced to ~ 1100 emu cm^{-3}. This is about 20% reduction from the as-deposited film signal, compared to only 10% reduction for Co nanoparticles. As explained in **Section 6.4**, this decrease can be attributed to post-annealing oxidation. Average diameter of CoAu nanoparticles is ~100 nm. Thus, it is expected that larger volume fraction of the nanoparticles was oxidized compared to Co which has diameter of ~200 nm. Similar as before, the grown oxide thickness can be calculated as,

$$\frac{\Delta Volume}{Volume} = 0.20$$

$$\frac{2\pi r^2 \delta}{\frac{2}{3}\pi r^3} = 0.20$$

$$\delta = \frac{0.20r}{3} \sim 3nm$$

which is consistent with our obtained δ value earlier.
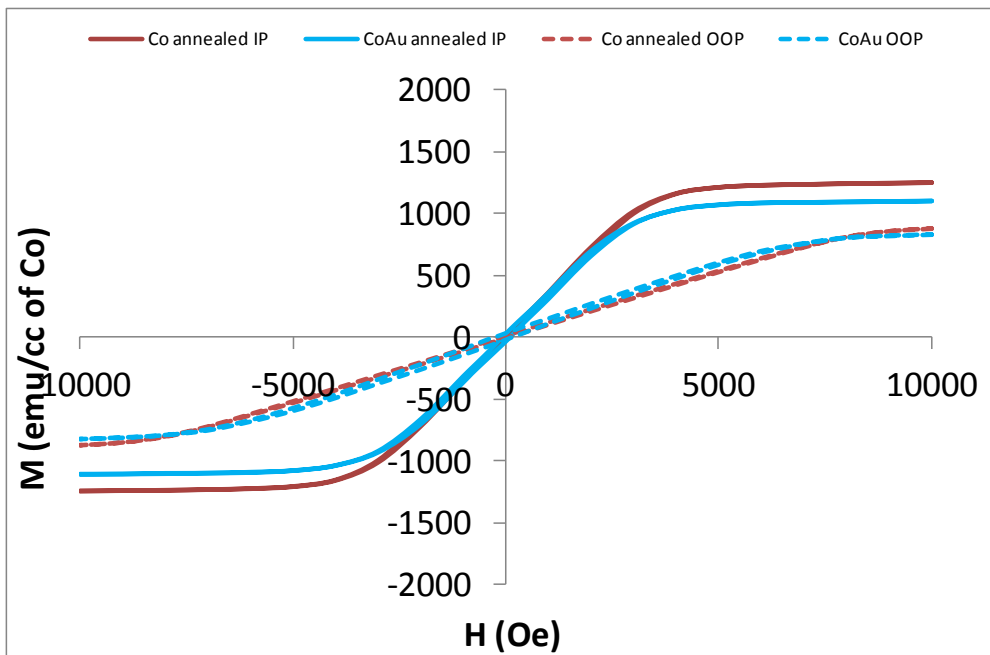
Figure 6.7: In-plane and out-of-plane magnetic hysteresis loops from CoAu and Co nanoparticles.

6.6   Summary

This study has provided a better understanding of the magnetic properties of miscible and immiscible alloy particles, in particular CoPd and CoAu systems. The as-deposited films show the expected in-plane magnetic shape anisotropy. After annealing, the magnetic behavior of dewetted Co, CoPd and CoAu nanoparticles show little anisotropy due to low magnetocrystalline and shape anisotropy of the nearly spherical fcc particles. Furthermore, the dewetted particles vary in size and distribution due to the absence of templating. In addition, strong exchange interaction between Pd and Co resulted in an increase in the total M_s. For CoAu system, the magnetic hysteresis loops are similar to those of Co. This is expected because Co-Au is an immiscible system and the magnetic contribution comes solely from Co. The M_s of Co and CoAu nanoparticles slightly decreased due to post-annealing oxidation. For a possible application as information storage, an ordered array of nanoparticles with uniform size and distribution is necessary, which is possible with proper templating. We might also explore other type of alloy that will form particles with strong magnetocrystalline anisotropy.

Chapter 7. Synthesis of Silicon Oxide Nanowires and Nanotubes with CoPd or Pd Catalysts

7.1 Introduction

A phenomenal amount of interest has been devoted to the exploration of the potential of one-dimensional nanostructures for future electronic, sensing and energy generating devices and systems. For example, silicon nanowires have been successfully implemented as field effect transistors,[144] chemical sensors,[145] and solar cells,[146] and carbon nanofibers have been investigated for field emitting applications.[147,148] Silicon-based nanowires have been synthesized by VLS[149-152] and SLS mechanisms[153,154] using a gas or solid precursor. There are also reports on growth of silicon-based nanowires by the same mechanisms without using an external silicon source, in which the source of silicon is the substrate itself.[155-160]

Au is the most common metal catalyst used to grow Si nanowires. There are several reports that used Pd[155,160] or Co[161-163] as catalyst for Si or silicon oxide nanowires or nanotubes. Pd is sometimes used in form of Pd/Au alloy. The growth mechanism of the Si-based nanowires or nanotubes using Pd or Co catalyst can be distinguished as follow: if the growth uses external Si supply (e.g. silane), the growth temperature can be lower than the eutectic temperature of the metal-Si and the catalyst remains solid during the growth process; if the supply of the Si comes from the substrate/wafer itself (either in solid, liquid, or vapor phase), the temperature is usually high and the catalyst will generally be in liquid state during the growth process. Other metals such

115

as Sn,[164,165] molten Ga,[166] In,[154] Ni, Fe$_2$O$_3$, CuS, Mn, Ir, MnPt$_3$[161] have also been tried. Recently, the VSS mechanism has also been employed to grow Si-based nanowires[167-173] and nanotubes[163,172,173] using metal catalysts such as Au, Al, Co silicide, and Pd silicide by chemical vapor deposition.

When the VSS mechanism is operational, a gas precursor needs to be supplied to grow the nanowires or nanotubes but the growth temperature is significantly lower than that required for the VLS and SLS mechanisms, namely lower than the eutectic temperature of the metal catalyst–Si.

After exploring the dewetting of CoPd in Chapter 4, in this chapter, we explore its use as a catalyst for growth of silicon nanowires and nanotubes without an external silicon source and compare the results with Co and Pd catalysts. These Si nanowires and nanotubes were oxidized in-situ during growth so the resulting nanowires and tubes consisted of silicon oxide. We first studied the dewetting characteristics of Co, Pd, and CoPd thin films on top of a silicon oxide layer in order to obtain suitable metal catalysts for the synthesis of silicon oxide nanowires and nanotubes. We examine the influences of ambient atmosphere, annealing temperature, catalyst and choice of substrate on the structural properties of the silicon oxide nanostructures and propose a growth mechanism for the nanostructures.

7.2 Experimental Details

Si wafers of (100) orientation were cleaned in acetone for 30 minutes and isopropanol for 5 minutes, followed by rinsing in de-ionized water. Two types of diffusion barrier were used: (i) silicon oxide (85 nm and 500 nm thick layers) and (ii) aluminum oxide (10 nm and 100 nm thick). The silicon oxide

116

layer was grown by wet oxidation. The aluminum oxide layers were sputter-deposited at a deposition rate of ~ 1 nm/min in a system with a base pressure of ~ 1 x 10^{-6} Torr. Co, Pd and CoPd films with thicknesses of 19 nm and 57 nm were deposited on the Si substrate by magnetron sputtering with a base pressure of 5 x 10^{-8} Torr. The deposition rate of Co was 0.24 Å/s and the deposition rate of Pd was 0.33Å/s. The 19 nm CoPd layer stack consisted of a 5 nm Pd underlayer then four bilayers of 0.5 nm Co/3 nm Pd. The 57 nm CoPd film was obtained by repeating the stack three times.

For the samples with a pre-patterned catalyst, a hole-array was first defined in a photoresist layer using interference lithography followed by metal deposition and lift-off. For pattern transfer into the aluminium oxide layer, the sample was etched in 7:1 buffered hydrofluoric acid (BHF) for ~ 1 minute. All the samples were annealed at annealing temperatures in the range of 650-1050 ^{0}C in N_2 or forming gas (90% N_2 + 10% H_2) ambient (99.995% purity). The structure and composition of the catalysts, nanowires and nanotubes were characterized using field emission scanning electron microscopy (FESEM), high-resolution transmission electron microscopy (HRTEM) and the energy dispersive X-ray spectroscopy (EDX) was performed using a JEOL 2010F system.

7.3 Catalyst Dewetting

Si wafers with an oxide layer of 85 nm were coated with Co, Pd, and CoPd films, each of 19 nm thicknesses. **Table 7.1** summarizes the annealing results of Co, Pd, and CoPd films annealed at 650, 750, and 950 ℃ for 30 minutes in N_2 and forming gas ambient. **Figure 7.1** shows some representative

117

SEM images of Co, Pd, and CoPd annealing results in forming gas ambient. Other annealing results with different parameters can be found in **Figure 7.2** - **Figure 7.4**.

Table 7.1: Summary of annealing results of Co, CoPd and Pd thin films.

	ambient	temperature	annealing results	crater
Co	**N₂**	650 °C	continuous film with voids (~100nm)	no
		750 °C	continuous film with large number of smaller voids (~30nm)	no
		950 °C	continuous film	no
	forming gas	650 °C	mixture of separated islands and networks	no
		750 °C	separated islands (average size ~350nm; average interparticle distance ~750nm)	no
		950 °C	separated islands (average size ~200nm; average interparticle distance ~400nm)	no
Pd	**N₂**	650 °C	interconnected islands	no
		750 °C	interconnected islands	no
		950 °C	elongated islands with neckings	no
	forming gas	650 °C	separated islands (average size ~300nm; average interparticle distance ~ 550nm)	no
		750 °C	short nanowires (length ~ 150 nm; average diameter of spherical metal particles ~ 300nm)	yes
		950 °C	short nanowires (length ~ 200 nm; average diameter of spherical metal particles ~ 200nm)	yes
CoPd	**N₂**	650 °C	continuous film with some voids of irregular shapes	no
		750 °C	interconnected islands with cobalt oxide underlayer	no
		950 °C	separated islands with cobalt oxide underlayer	no
	forming gas	650 °C	elongated islands with neckings	no
		750 °C	spherical metal particles (average size ~ 400nm), a few have short nanowires (< 50nm)	yes
		950 °C	few deep pits (length ~ 2-3 µm; width ~ 700nm-1µm) with long wires (~800nm - 5µm) surrounding them and short wires (~200nm) away from the pits	yes
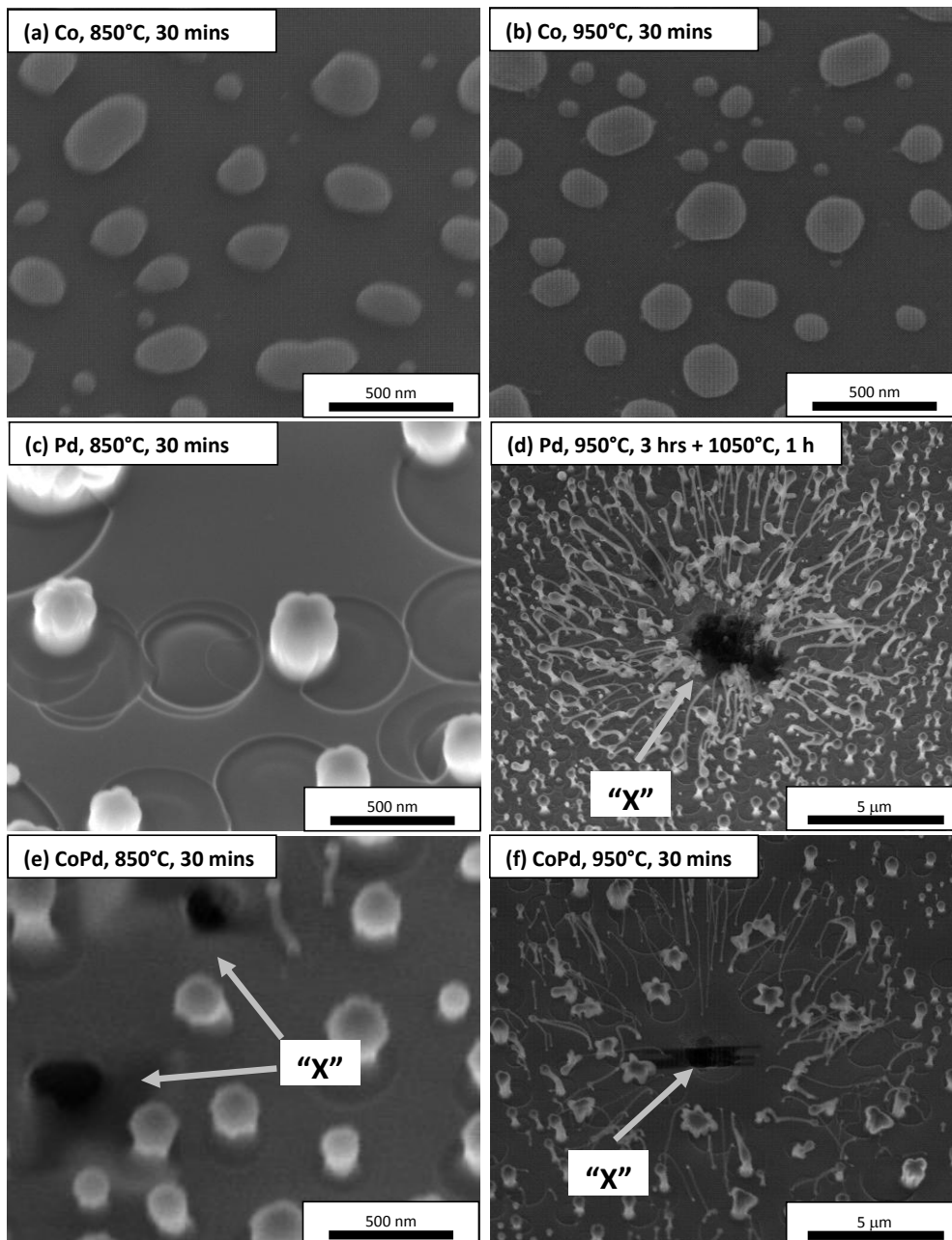
Figure 7.1: SEM images of Co, Pd, and CoPd films annealed at different annealing temperatures and durations in forming gas ambient (as indicated in the inset).
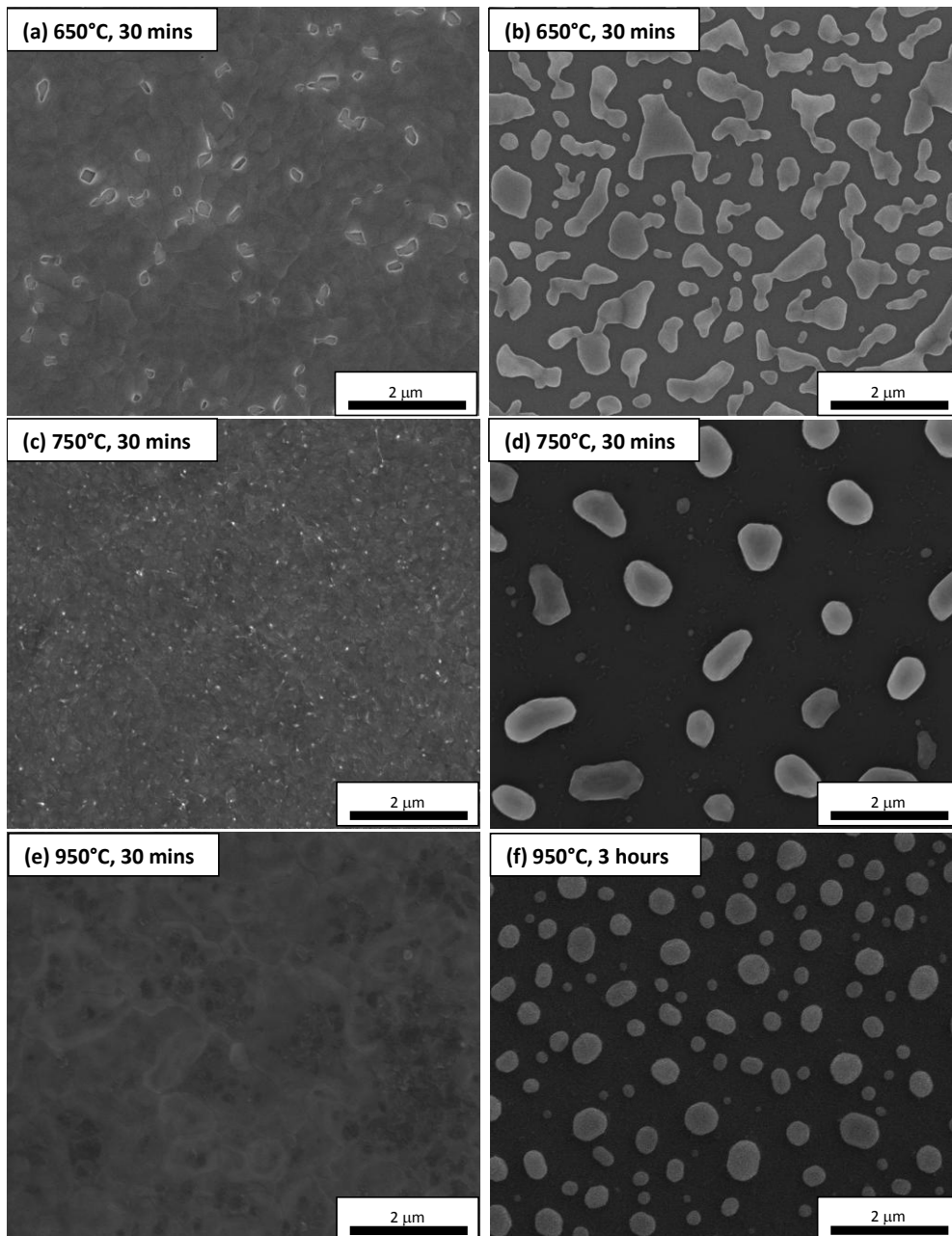
Figure 7.2: SEM images of Co films annealed at different annealing temperatures and durations in N_2 ambient (a, c, e) and forming gas ambient (b, d, f).
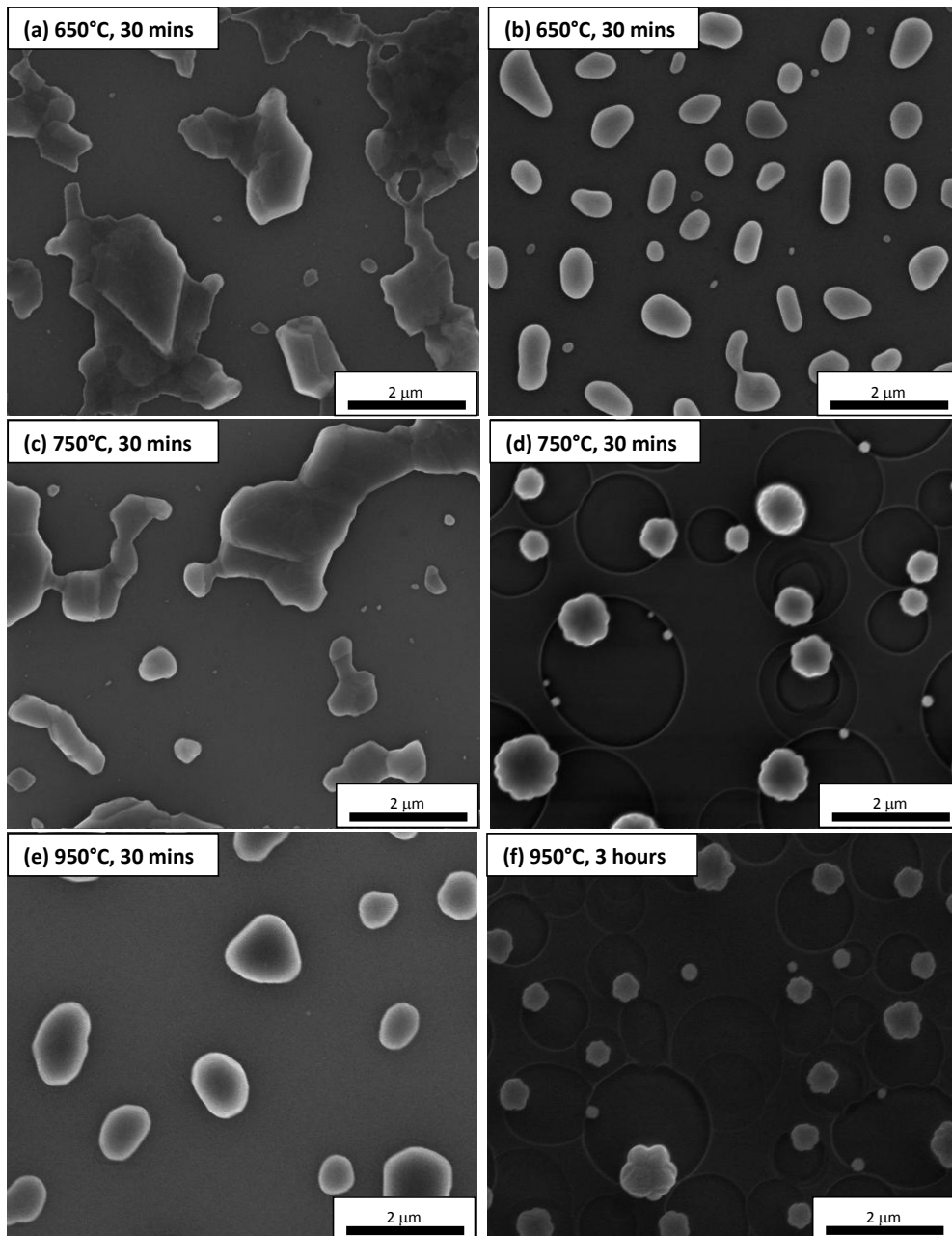
Figure 7.3: SEM images of Pd films annealed at different annealing temperatures and durations in N_2 ambient (a, c, e) and forming gas ambient (b, d, f).
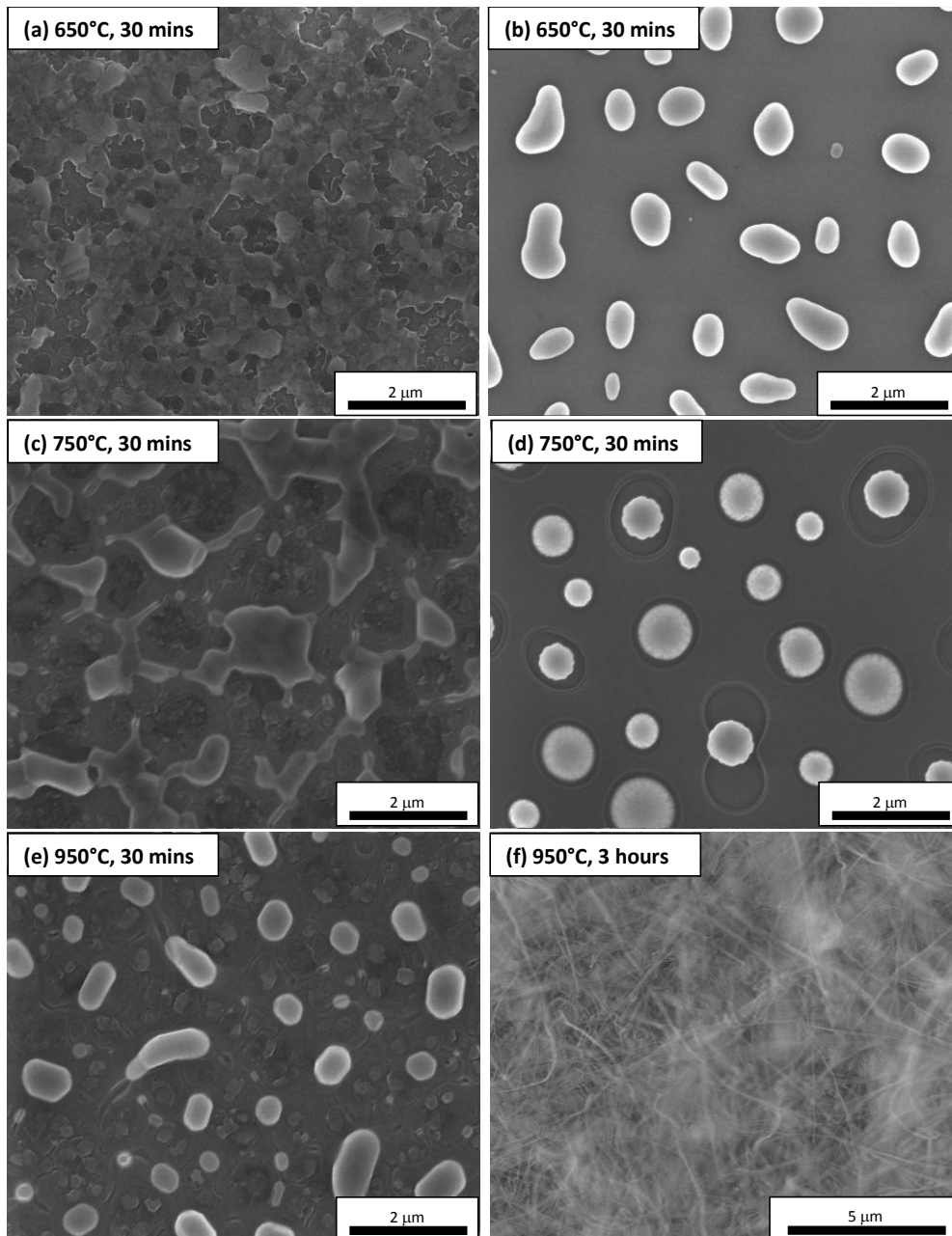
Figure 7.4: SEM images of CoPd films annealed at different annealing temperatures and durations in N_2 ambient (a, c, e) and forming gas ambient (b, d, f).

Figure 7.1a and **b** and **Figure 7.2b**, **d** and **f** show dewetted Co particles annealed in forming gas ambient. Co films started to dewet at 650°C in the forming gas. For Co films annealed in N_2 ambient, the film started to dewet and developed voids of diameter ~100nm at 650°C. At 750°C, however, the voids were smaller and at 950°C, the film remained continuous. We suggest

that during annealing of Co films in forming gas ambient, the H_2 in the forming gas prevents formation of cobalt oxide, enabling the film to dewet.[107] It appears likely that annealing in the N_2 ambient caused partial oxidation of the Co film and this hindered the dewetting process. With N_2 gas of 99.995% purity and assuming the rest of the composition is comprised of oxygen, an O_2 partial pressure of 10^{-5} atm is obtained. From the Ellingham diagram[107], the equilibrium O_2 pressure for the formation of cobalt oxide ($2Co + O_2 \rightarrow 2CoO$) at 650 ℃ - 950 ℃ is about $10^{-16} - 10^{-10}$ atm. This implies that the CoO formation is always favored in our experimental conditions.

Palladium oxide is not expected to form at 650 to 1050 ℃ in forming gas ambient because the Gibbs free energy for palladium oxide formation is always larger than the water vapor formation.[107] Even in N_2 ambient with a purity of 99.995%, assuming all the rest of the residue gases is oxygen, this will give an oxygen partial pressure ~10^{-5} atm. However, the oxygen partial pressure needed to form palladium oxide at this temperature must be greater than 4×10^{-3} atm.[174] Therefore, no palladium oxide formation is expected in N_2 ambient as well.

The Pd films partly dewetted in N_2 at 650 ℃ but formed well separated islands at 950 ℃ (**Figure 7.3a, c, e**). In forming gas, however, the morphology was very different (**Figure 7.1c, d** and **Figure 7.3b, d, f**). Well defined islands formed at 650˚C, but after 30 min at 750 - 950 ℃, short nanowires were observed with metal catalyst particles at the top of the nanowires, and reaction of the substrate was evident, forming shallow circular pits. The catalyst size reduced from 300 to 200 nm as the annealing temperature increased. After an anneal at 950 ℃ for 3 hours followed by 1050 ℃ for 1 hour, **Figure 7.1e**,

inverted pyramidal pits (marked as "X") were evident, surrounded by significantly longer nanowires.

In the case of CoPd, the Pd content was 86 atomic %. From the CoPd phase diagram,[86] the alloy should be single phase with Co miscible in Pd at all the annealing temperatures used in this work. For the samples annealed in N_2 (**Figure 7.4a, c, e**), the CoPd film showed partial dewetting at 650 – 750˚C and well developed islands, with some substrate roughening, at 950 ˚C, but no nanowire growth was observed. In contrast, when annealed in forming gas (**Figure 7.1e, f** and **Figure 7.4b, d, f**) , the CoPd films dewetted into islands at 650 ℃ and above and these served as catalysts for nanowire growth, producing morphologies similar to those observed for Pd. The nanowires were short at 750 ℃ and 850 ℃, but at 950 ℃ longer wires were formed in the vicinity of substrate pits. Pitting occurred at lower temperatures for CoPd compared with Pd, i.e. at 850 ℃, and nanowires formed more abundantly on CoPd at 950 ℃ (compare **Figure 7.4f** and **Figure 7.1d**).

The formation of the nanowires and the craters in the Si substrate is therefore correlated with the presence of hydrogen and palladium during high temperature annealing. Pd and CoPd can both be used as catalysts for nanowire growth above 750 ℃ in forming gas.

7.4   Structural Characterization of As-Grown Nanowires and Nanotubes

Figure 7.5 shows a SEM image of the as-grown nanostructures formed using CoPd at 950 ℃ in forming gas for 30 min. Three types of structures can be observed: (i) silicon oxide nanowires with catalysts at the top; (ii) silicon oxide nanotubes with embedded metal catalysts; (iii) metal catalysts covered

124

by a silicon oxide shell which do not grow into wires or tubes. The ratio of Pd:Co for the top catalysts for all the nanowires remained fairly similar to the original film composition of 6:1. The identification of the wires/tubes as silicon oxide instead of silicon is based on TEM, described below.
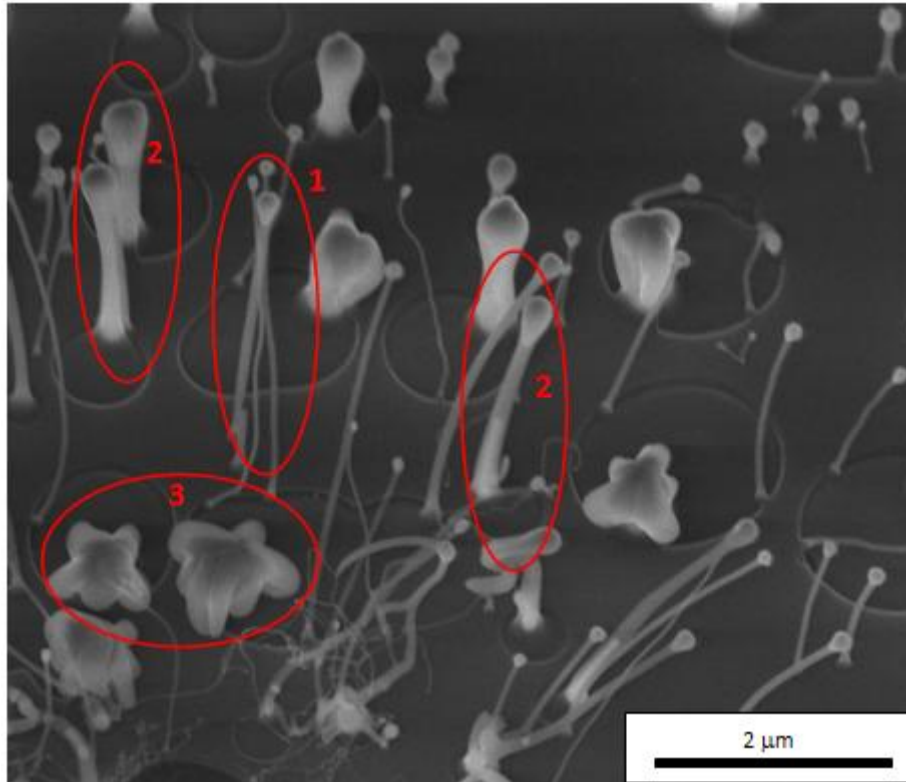
Figure 7.5: SEM images of CoPd sample annealed at 950C for 30 minutes in forming gas; (1) nanowires with single catalyst at the top; (2) nanotubes with embedded catalysts; (3) large catalyst particle covered with oxide shells.

Table 7.2 summarizes the morphology of the nanostructures and the approximate size of the catalyst particles from the samples. The majority of the as-grown structures are nanowires with a single catalyst at the tip. From the images it appears that the smaller catalyst particles produce nanowires with the catalyst at the top, the intermediate-size catalysts produce nanotubes with either cylindrical or split catalysts, and the larger catalysts do not form either wires or tubes.

125

Table 7.2: Different morphologies of the nanostructures grown with CoPd or Pd catalyst.
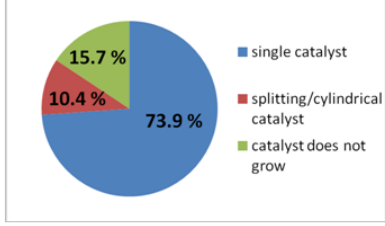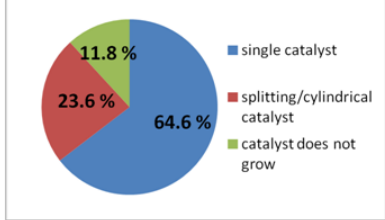
	size of catalysts ($\times 10^{-4} \mu m^3$)	structure	percentage
Pd	3 – 1500	nanowires with single catalysts	single catalyst 73.9 %, splitting/cylindrical catalyst 10.4 %, catalyst does not grow 15.7 %
	190 – 1000	nanotubes with cylindrical or splitting catalysts	
	190 – 5000	large catalysts that do not grow	
CoPd	3 – 190	nanowires with single catalysts	single catalyst 64.6 %, splitting/cylindrical catalyst 23.6 %, catalyst does not grow 11.8 %
	370 – 1000	nanotubes with cylindrical or splitting catalysts	
	1500 – 12000	large catalysts that do not grow	

Figure 7.6a shows a TEM image of a nanowire obtained from the Pd film in forming gas ambient at 950 ℃ for 3 hours and then further annealed at 1050 ℃ for 1 hour. **Figure 7.6b** and **c** show higher resolution TEM of the nanowire and the catalyst. The data suggest that after growth the catalyst was transformed to palladium silicide which is crystalline with atomic ratio of Pd:Si from EDX close to 8:1. From the Pd-Si phase diagram,[175] this corresponds to $(Pd) + Pd_{21}Si_4$ phases at room temperature. The nanowire itself is amorphous and consists of silicon oxide. A split palladium silicide catalyst covered with a SiO_2 shell is shown in **Figure 7.6d**.

A TEM image of a nanowire obtained from the CoPd film in forming gas ambient at 950 ℃ for 30 minutes is shown in **Figure 7.6e**. Similar EDX analysis was also carried out for the catalyst and the body. The catalyst was crystalline and contains Pd, Co, Si and O. The presence of O attributed to the SiO_2 shell. The ratio of Pd:Co varied between region "2" (5.5:1), region "3" (17:1), and region "4" (31.5:1), while the initial film composition was close to

126

6:1. This suggests that as the catalyst splits, the fragment closer to the growing end of the wire is richer in Pd, which is the active catalyst. The wire or tube is amorphous and consists of silicon oxide.
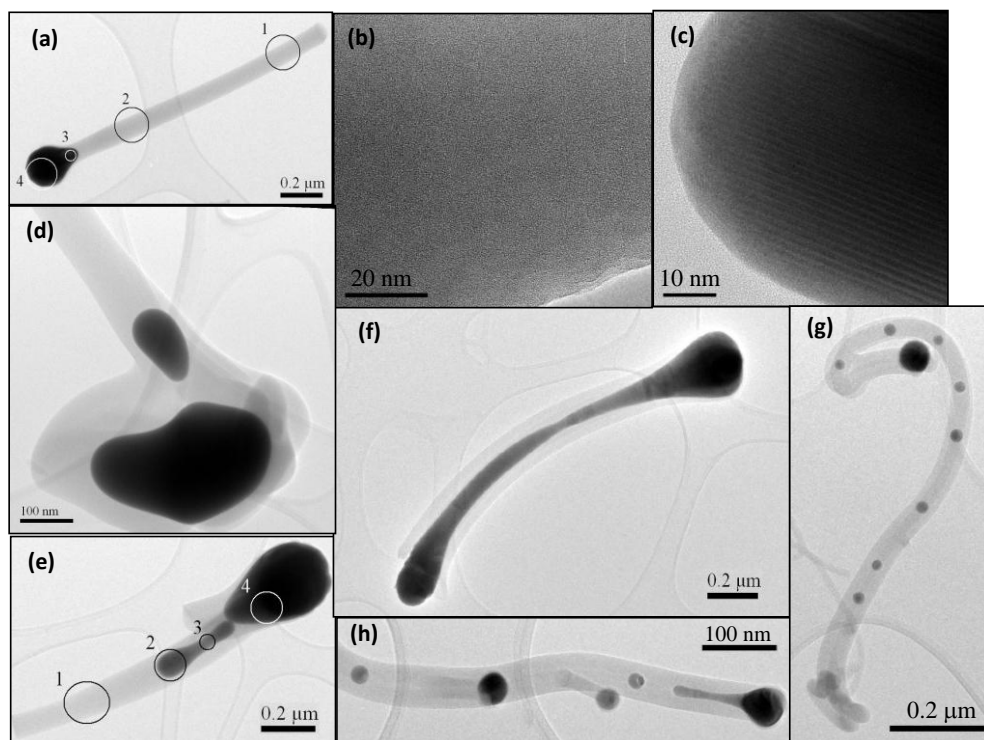
Figure 7.6: (a) TEM images of Pd sample annealed at 950 ℃ for 3 hours followed by 1050 ℃ for 1 hour in forming gas with the numbers indicating the area of EDX measurement; (b) HRTEM of the body; (c) HRTEM of the Pd catalyst; (d) TEM images of Pd catalyst covered with SiO2 shell; (e) a nanowire grown by CoPd catalyst at 950 ℃ for 30 minutes with the numbers indicating the area of EDX measurement; (f) a single nanotube grown by CoPd catalyst with elongated catalyst before splitting; (g) A nanotube with multiple catalyst splitting grown by CoPd catalyst at 950 ℃ for 3 hours; (h) A branching nanotube.

Figure 7.6f shows a nanotube within which the catalyst exhibits necking, obtained from CoPd at 950 ℃ for 30 mins. **Figure 7.6g** shows an instance of multiple splitting of a CoPd catalyst into sub-catalysts (950 ℃ for 3 hours). The catalyst particles are much rounder in shape compared to the catalysts that were annealed for 30 minutes. Branches were observed in some nanotubes with split catalyst particles (**Figure 7.6h**). For the CoPd samples

127

annealed at 950 ℃ for 3 hours, much longer nanowires and nanotubes (>10 μm) were observed than those seen in the sample annealed for 30 min.

7.5   Growth Mechanism

Figure 7.7 illustrates the proposed mechanism of nanowire and nanotube growth. **Figure 7.7a** shows the initial stage at which the metal film has dewetted into particles of different sizes. As mentioned above, the growth of the nanowires and nanotubes is associated with the formation of craters (shown schematically in **Figure 7.7b**) on the silicon oxide surface. We suggest that the formation of the craters is due to the Pd (in Pd or CoPd films) that reduces the SiO_2 layer to Si and forms palladium silicide during the anneal in forming gas ambient at temperatures >750 ℃.[73] While Ellingham diagram tells us that SiO_2 is practically irreducible in H_2 environment, it has been found that Pd has an enormous capacity to absorb H_2 gas, up to more than 0.6 of H-to-Pd atomic ratio.[176] The incorporation of H_2 in large amount forces Pd, which is originally fcc structure, to adopt another phase α, β, or a mixture of both with larger lattice constant, transforming it into a quasi-liquid state.[177,178] This transforms Pd into a quasi-liquid state which might render the material more reactive to its surrounding material, e.g. reaction with silicon oxide to form palladium silicide, in this case. This process of silicon oxide reduction occurs concurrently with the agglomeration process of the metal catalyst. The silicide formed is expected to be Pd-rich because the Si is only supplied from the reduction of SiO_2.
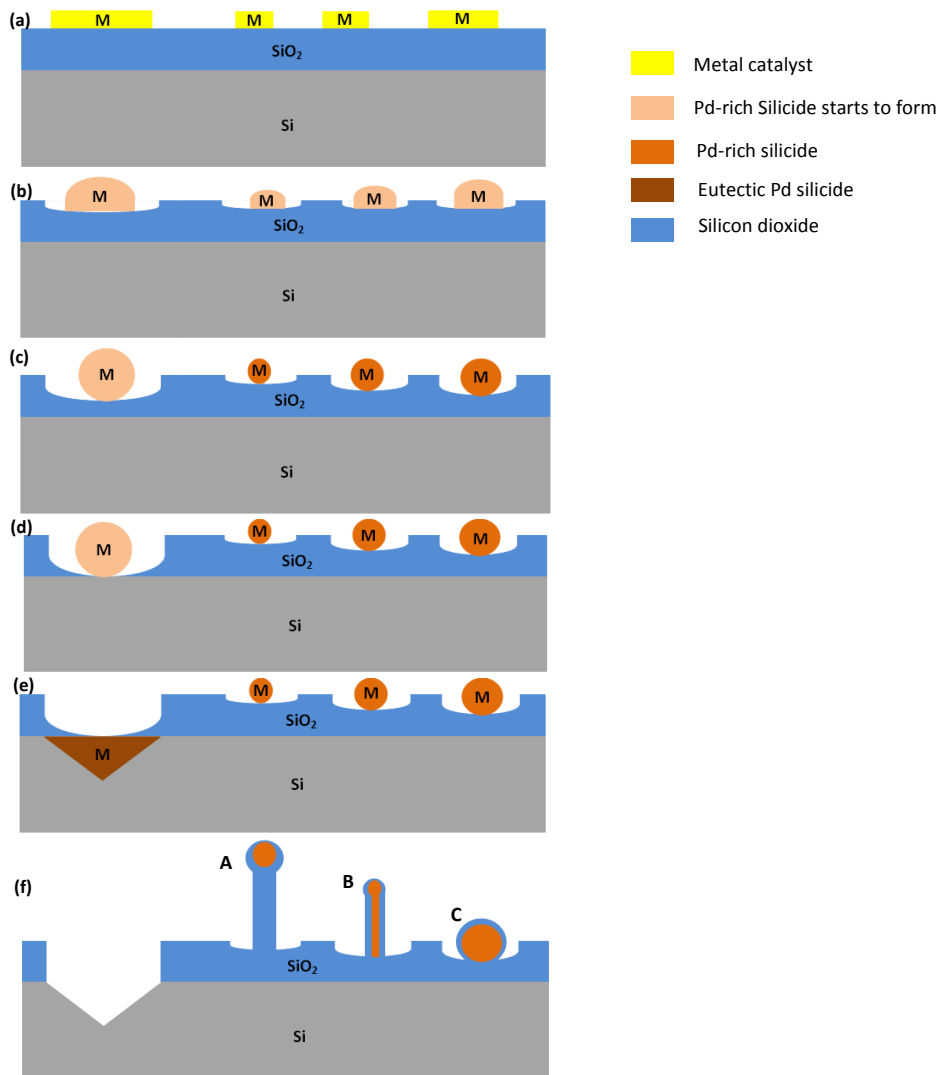
Figure 7.7: Schematic diagram of the nanowire and nanotube growth.

As illustrated in **Figure 7.7c** to **e**, the smaller metal particles will form a silicide without penetrating the oxide layer, while the larger particles will consume sufficient SiO_2 to come into contact with the Si substrate. Once the metal particles are in contact with the Si substrate, the supply of Si is abundant. The silicide formed will then have the eutectic composition and be in a liquid state because the annealing temperature is higher than the eutectic temperature. The high flow rate of forming gas promotes evaporation of the silicide to form inverted pyramidal pits (the "X" region in Fig. 1). These pits become a source of Si vapor to promote growth of nanowires around the pits.

The pit formation is due to diffusion of Si and leaves (111)-facetted surfaces. Similar pit formation at the Si surface due to aluminum spiking has also been reported during the fabrication of metal-oxide-silicon devices.[74] **Figure 7.7f** summarizes all possible grown structures that resulted in nanowires (A), nanotubes (B) and metal catalysts that do not grow into wires or tubes (C).
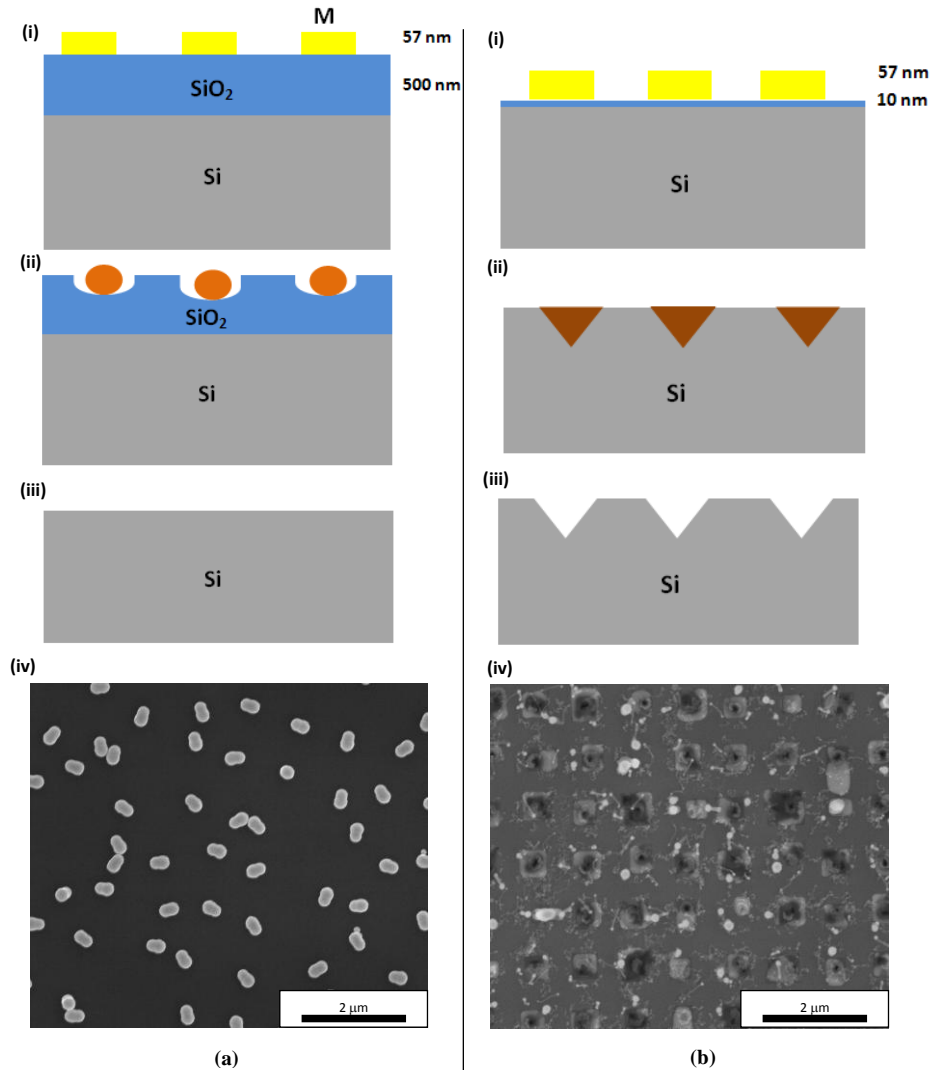
Figure 7.8: (a) Schematic diagram of the dewetting process of CoPd or Pd film on 500nm-silicon oxide. (i) the patterned metal on silicon oxide; (ii) the formation of craters; (iii) Flat silicon substrate after HF dip; (iv) SEM images of CoPd samples on 500nm-silicon oxide after annealing at 950C for 30 minutes in forming gas ambient. (b) Schematic diagram of the dewetting process of CoPd or Pd film on 10nm-silicon oxide. (i) the patterned metal on silicon oxide; (ii) the formation of inverted pyramid pits; (iii) Inverted pyramid pits on silicon substrate after the metal catalyst evaporated away; (iv) SEM images of CoPd samples on 10nm-silicon oxide after annealing at 950C for 30 minutes in forming gas ambient.

We examined the critical role of the SiO_2 layer thickness in pit formation by depositing CoPd and Pd films (57nm) on two samples with a thicker (500 nm) and a thinner (10 nm) silicon oxide layer. By using interference lithography, we obtained CoPd and Pd dots (diameter ~ 850 nm) on top of the thick and thin silicon oxide layer. The samples were then annealed at 950 ℃ for 30 minutes in forming gas ambient, as shown in **Figure 7.8**. The samples with thicker oxide underlayer are expected to form craters but no inverted pyramid pits because the thick oxide provides sufficient Si for complete silicidation of the Pd, as shown schematically in **Figure 7.8a(i)-(iii)**. A SEM image of such a sample with CoPd catalyst after the thick oxide underlayer was removed by HF is shown in **Figure 7.8a(iv)**. A smooth Si surface is evident, covered with CoPd particles which have presumably also been modified by the etch process. For the samples with the thinner oxide underlayer (**Figure 7.8b(i)-(iii)**), the CoPd and Pd catalysts will consume all the oxide underlayer upon annealing and form inverted pyramidal pits in the silicon substrate, as shown in the SEM image of annealed samples with CoPd catalysts (**Figure 7.8b(iv)**).

As shown in **Figure 7.1**, the nanowires and nanotubes only grow significantly in the area near the exposed silicon substrate, i.e. the inverted pyramid pits. Furthermore, all the nanowires and nanotubes are a few microns long and have the metal catalyst particles at the tip. If the source of the Si atoms is from the solid Si substrate, surface diffusion would limit the growth, unless the catalyst particles were at the base of the nanowires. These are strong indications that the silicon source is vapor.

There are three possible sources for the Si in the vapor phase. The first is SiO vapor from the dissociation of the oxide layer at high temperature in forming gas ambient.[179,180] It has been reported that silicon oxide at high temperature in the presence of hydrogen will release SiO vapor, according to the reaction $SiO_2(s) + H_2(g) \rightarrow SiO(g) + H_2O(g)$. The SiO is then transported to the surface of the CoPd or Pd catalyst particles and releases Si atoms.[157] The annealing temperatures that have been reported in the literature for this reaction are, however, 1200 °C and higher. As can be seen from **Figure 7.1c**, even when there is no pyramidal pit formed, an oxide layer formed to cover the metal catalyst. This indicates that even in the range of 750 – 1050 °C, there exists a small amount of Si-containing vapor from the reaction of silicon oxide layer and the hydrogen in the chamber. However, it is insufficient to grow long wires/tubes.

The second possible source is SiO vapor from the dissociation of SiO_2 at the Si/SiO_2 interface at high temperature and low oxygen partial pressure by the reaction: $Si + SiO_2 \rightarrow 2SiO$.[181] This might lead to the irregular shapes of the pits (see for example, **Figure 7.1d**) during wire growth. The SiO vapor from the Si/SiO_2 interface can also diffuse through the oxide layer,[182] but this would be slow for samples with a thick oxide layer.

The third possible source is Si vapor evaporating from the substrate once the Si is exposed.[155] To examine this, a sample was annealed consisting of Pd circular dots, 800 nm diameter and 57 nm thick, on an alumina-coated Si substrate, but no nanowires formed because alumina does not react with the metal catalyst under given annealing condition. Then the parts of the alumina not coated with metal were dissolved, exposing the Si substrate around the Pd

132

catalyst (**Figure 7.9a**) and the sample was annealed at 950 ℃ for 30 minutes in forming gas ambient. **Figure 7.9b** shows that a large nanowire with a catalyst at its tip formed at each patch of metal, accompanied by erosion of the regions of the Si surface uncoated with alumina. Nanowires formation is expected for this size of catalyst (2.9×10^{-2} μm^3) as shown in **Table 7.2.**
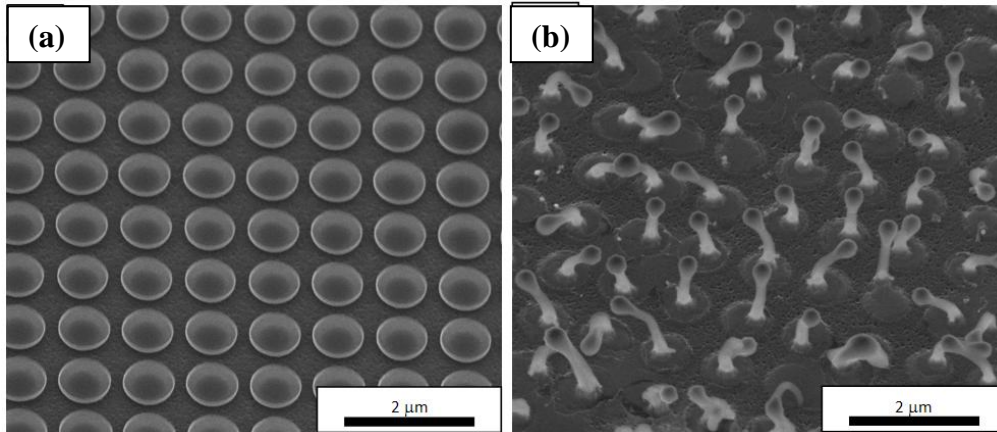
Figure 7.9: (a) Pd catalyst on alumina layer after BHF dip; (b) After annealing at 950C for 30 minutes in forming gas ambient.

The Si vapor pressure (P) above a silicon substrate can be estimated as $P = A_P \exp(-\Delta H_{vap} / R_G T)$ where A_P is an empirically determined constant, ΔH_{vap} is the enthalpy of Si evaporation, R_G is the gas constant and T is the temperature. Values[183] of $A_P = 2.24 \times 10^6$ atm and $\Delta H_{vap}/R_G = 49.70$ K yielded Si vapor pressures for various annealing temperatures as listed in **Table 7.3**.

Table 7.3: Silicon vapor pressure at various temperatures.

T (℃)	P (atm)
650	9.27×10^{-18}
750	1.79×10^{-15}
850	1.35×10^{-13}
950	5.05×10^{-12}
1050	1.09×10^{-10}

Using the geometry of the alumina-coated sample, each nanowire is supplied by the Si flux from an area of 1 μm $\times$ 1 μm minus the fraction coated

by the alumina disc. The flux of Si escaping from the exposed Si surface is estimated as[184,185]

$$J_{Si} = 3.51 \times 10^{22} \frac{P(in\ Torr)}{\sqrt{M_W T}} = 7.26 \times \frac{10^{11} atoms}{cm^2.sec}$$

Equation 7.1

For annealing at 950 ℃ (P_{Si} = 5 x 10^{-12} atm) for t = 30 minutes, the flux of Si is 8.0 x 10^6 atoms ($J_{Si} \times A_{sor} \times t$). This can be compared with the number of Si atoms in each nanowire, which has a diameter of approximately 150 nm and height of 500 nm, corresponding to 1.9×10^8 atoms. The evaporated flux is 25 times too small to supply the nanowire based on this simple estimate, but the difference could be resolved if the wire is hollow as suggested by the TEM images of **Figure 7.6**, or if the evaporation rate is enhanced by the flow of forming gas.[186-188]

The Si nanowires and tubes which form are assumed to be oxidized by residual oxygen present in the annealing chamber to form SiO_2. From the Ellingham diagram[107], the equilibrium O_2 partial pressure for the formation of SiO_2 at temperatures of 650 ℃ - 1050 ℃ is about 10^{-34} - 10^{-20} atm. From the same diagram, the equilibrium O_2 partial pressure in the forming gas (10% H_2) at these temperatures is much higher at a range of 10^{-19} – 10^{-12} atm. This means the formation of SiO_2 is always favored in our experiments. Furthermore, as the Si atoms were deposited on the catalyst in a layer-by-layer fashion, it is possible for the whole body of the nanowires or nanotubes to be fully oxidized. The possibility of Si nanowires being oxidized after removal from the chamber is ruled out because the samples were cooled down to room

temperature before they were taken out from the furnace, and the oxidation process at room temperature is too slow to account for the depth of the oxide with nanowires as thick as ~175 nm in diameter.

7.6 Catalyst Morphology

In Section 6.4, the atomic ratio of Pd:Si in the Pd catalyst was determined to be 8:1. At a growth temperature of 950 °C, this corresponds to 21% solid (Pd) + 79% liquid (L) phases from the equilibrium phase diagram, with the L phase containing 14% Pd. This suggests the catalyst was at least partly liquid at the growth temperature. The phases present in the CoPd catalyst are not known, but the morphology was broadly similar to that of Pd particles. The catalyst particles showed smooth contours without obvious faceting, and were covered with a thin layer of silica shell. For certain size ranges (0.019-0.1 μm^3 for Pd catalyst and 0.037-0.1 μm^3 for CoPd catalyst), some of the metal catalysts underwent elongation from nanoparticles to nanorods. Recently, reshaping of catalyst particles was reported for carbon nanotube growth but with the Ni catalyst remaining solid during growth.[189] As the source of the Si atoms is vapor and the catalyst particles are partly solid during the growth process, the growth mechanism of the silicon oxide nanowires and nanotubes is VSS, VLS or a combination. There have been several studies of the VSS mechanism in silicon-based nanowires or nanotubes but generally, this occurs at a growth temperature lower than the eutectic temperature of the metal – Si and uses gas precursors.

135

7.7 Summary

We have demonstrated a simple technique to fabricate SiO_2 nanowires and nanotubes on oxidized Si substrate using CoPd and Pd catalyst via VLS or VSS mechanism without using external Si source. The growth occurred when the catalysts are annealed in forming gas which will induce the formation of craters in the oxide layer and lead to the formation of pits in the Si substrate which supplied Si for the nanowire growth. We demonstrated that the thermal budget can be reduced by using CoPd alloy as catalyst compared to Pd. This suggests the possibility to further tune the thermal budget for this growth technique by exploring different CoPd compositions. Some of the nanotubes had a series of embedded sub-catalysts that formed branches from the primary nanotube. Our discovery of splitting catalysts and branches formation indicate that more complex nanostructures can be grown using this technique. We also showed that the resulted morphologies depend on the catalyst size, i.e. smaller catalysts give nanowires and larger catalysts give nanotubes. This allows us to tune the type of grown nanostructures provided that precise control of catalyst size is available. Based on this finding, we have fabricated an array of nanowires using interference lithography patterning technique.

Chapter 8. Conclusion

8.1   Summary

The main objectives of this thesis were to investigate the solid-state dewetting behavior of CoPd and CoAu thin films and explore their possible applications.

First, we established that CoPd alloy undergoes similar stages of dewetting as elemental materials. Stages of dewetting were identified and grouped into six distinct stages, namely hole initiation, hole growth, interconnected islands, isolated islands, island coarsening, and particles. Interstage transition was found to be material-dependent, particularly determined by the surface diffusivity. We experimentally determined that the transition for CoPd lies between that of Co and Pd. Equilibrium particle shape was predicted using Winterbottom construction and the results were compared with experimental data. CoPd particle shape was found to adopt a combination of its Co and Pd constituents. We characterized the CoPd dewetting behavior as a function of annealing temperature. Hole incubation temperature was found to be material-dependent, that is lower for material with higher surface diffusivity. Plotting the area fraction transformed as a function of homologous temperature allows one to distinguish the effect of crystal structure. Fcc materials (Au and Pd) exhibit unique characteristics as compared to hcp material (Co). JMA analysis was used to predict the fraction of area transformed for each material and agrees with the experimental data. Void incubation time and its dewetting activation energy were extracted for Au, Co, Pd, and CoPd, and it was concluded that surface diffusion is the dominant mechanism. Morphology of the dewetted particles was characterized in terms

137

of interparticle spacing, particle density, and particle size, all of which are found to be material dependent. Structural and compositional studies were carried out using TEM and EDX.

Next, we have also established that CoAu alloy undergoes similar stages of dewetting as miscible alloy and elemental materials. We found that interstage transition and dewetting morphology depend on alloy composition. We have characterized the morphology of dewetted particles in terms of interparticle spacing, particle density, and particle size, and for CoAu, they were found not to lie between its parent materials. Three possible scenarios were proposed to distinguish the dewetting morphologies for different Au/Co thickness ratio. For CoAu alloy with high Au composition (Au-to-Co volume ratio $\geq$ 1.5), Au-rich particles and Co-rich particles are distinguishable and thus, they can be treated separately. We are able to predict the interparticle spacings and particle densities for both Au-rich and Co-rich particles. For this range of composition, we demonstrated the possibility to create clusters of nanoparticles array without resorting to lithography. For CoAu alloy with lower Au composition (Au-to-Co volume ratio < 1.5), both Co-rich and Au-rich phases can be found in a single particle. In this case, we can still predict the overall particle densities by adding up the density of each material. Structural and compositional studies were carried out using TEM and EDX.

We also characterized the magnetic properties of CoPd and CoAu alloy nanoparticles. We have shown that as-deposited Co, CoPd and CoAu thin films have similar in-plane and out-of-plane magnetic hysteresis loops with M_s close to that of bulk Co. The as-deposited films show strong in-plane anisotropy due to the shape of the film. After annealing, the magnetic behavior

138

of dewetted Co, CoPd and CoAu nanoparticles show little anisotropy due to low magnetocrystalline and shape anisotropy of the nearly spherical fcc particles. Furthermore, the dewetted particles vary in size and distribution due to the absence of templating. In addition, strong exchange interaction between Pd and Co resulted in an increase in the total M_s. For CoAu system, the magnetic hysteresis loops are similar to those of Co. This is expected because Co-Au is an immiscible system and the magnetic contribution comes solely from Co. The M_s of Co and CoAu nanoparticles slightly decreased due to post-annealing oxidation. For a possible application as information storage, an ordered array of nanoparticles with uniform size and distribution is necessary, which is possible with proper templating. We might also explore other type of alloy that will form particles with strong magnetocrystalline anisotropy.

Finally, we explored the application of CoPd and Pd nanoparticles for synthesis of SiO_2 nanowires and nanotubes via VLS or VSS mechanism without using external Si source on oxidized Si substrate. In contrast to general nanotubes fabrication scheme, which uses gas precursors,[163,172,173] our method offers a simple alternative because no dedicated gas line is required. The growth of silica nanowires and nanotubes occurred when the catalysts are annealed in forming gas. This wire growth was associated with the formation of craters in the oxide layer which, for larger catalyst particles and thinner oxide, led to the formation of pits in the Si substrate which supplied Si for the nanowire growth. We demonstrated that the thermal budget can be reduced by using CoPd alloy as catalyst compared to Pd. The resulting SiO_2 nanowires and nanotubes were amorphous and the length reached several μm depending on the annealing parameters. Some of the nanotubes had a series of embedded

sub-catalysts that formed branches from the primary nanotube. Our discovery of splitting catalysts and branches formation indicate that more complex nanostructures can be grown using this technique. We discovered that only certain type of oxide facilitates the nanowires and nanotubes growth. In this case, alumina was found not to induce craters formation which is essential for the growth. We also showed that the resulted morphologies depend on the catalyst size, i.e. smaller catalysts give nanowires and larger catalysts give nanotubes. This allows us to tune the type of grown nanostructures provided that precise control of catalyst size is available. Based on this finding, we have fabricated an array of nanowires using interference lithography patterning technique.

8.2   Recommendations

In this thesis, various promising findings related to dewetting of CoPd and CoAu alloys have been reported. There are still several potential avenues which can be further explored for future works.

There are still a lot to be understood about miscible and immiscible alloy dewetting. It might be useful to vary the parameters such as film thickness and layer configuration. For example, thicker film can be used to slow down the dewetting process and capture the dewetting stages in more details. It will be very beneficial given that in-situ observation is challenging. It might also be interesting to see the morphology of dewetted particles for co-sputtered alloy.

We have explored binary alloy systems for both miscible and immiscible cases. It might be worthwhile to extend the studies to ternary or even quaternary systems to provide more knobs to further engineer the dewetted

140

particles morphology and to improve the properties of the particles. It is also of fundamental interest to explore dewetting behavior, material properties and possible applications of hybrid miscible − immiscible alloy, for example Co-Pd-Au system. In this system, both Co-Pd and Pd-Au are miscible while Co-Au is immiscible and thus they are expected to exhibit complex and perhaps fascinating interactions.

We have explored the application of dewetting to fabricate nanowires and nanotubes. We can try to explore other applications such as plasmon waveguide or bit-patterned media recording. Plasmon waveguide can overcome the limitations of conventional dielectric waveguides such as diffraction limit of light. It has been demonstrated that well-ordered metal nanoparticle arrays such as gold and silver can guide electromagnetic energy in a coherent fashion.[190,191] It might be interesting to combine multiple metals such as Ag-Au or Ag-Cu. Dewetted particles can also be used as a low-cost approach to fabricate bit-patterned media which can overcome the thermal limitations of perpendicular recording. We have studied the magnetic properties of dewetted CoPd and CoAu, but for this application we will need to template the dewetting to produce nanoparticles with uniform size and distribution. We also need to explore other type of alloy that will form particles with strong magnetocrystalline anisotropy.

References

1. Feynman, R. P. There's Plenty of Room at the Bottom. *Eng. Sci.* **23,** 22–36 (1960).

2. Terris, B. D. & Thomson, T. Nanofabricated and self-assembled magnetic structures as data storage media. *J. Phys. Appl. Phys.* **38,** R199 (2005).

3. Ross, C. Patterned Magnetic Recording Media. *Annu. Rev. Mater. Res.* **31,** 203–235 (2001).

4. Zhang, L. *et al.* Nanoparticles in Medicine: Therapeutic Applications and Developments. *Clin. Pharmacol. Ther.* **83,** 761–769 (2007).

5. Huang, X. & El-Sayed, M. A. Gold nanoparticles: Optical properties and implementations in cancer diagnosis and photothermal therapy. *J. Adv. Res.* **1,** 13–28 (2010).

6. Choi, H. *et al.* Multipositional Silica-Coated Silver Nanoparticles for High-Performance Polymer Solar Cells. *Nano Lett.* **13,** 2204–2208 (2013).

7. Chen, X. *et al.* Broadband Enhancement in Thin-Film Amorphous Silicon Solar Cells Enabled by Nucleated Silver Nanoparticles. *Nano Lett.* **12,** 2187–2192 (2012).

8. Terrones, M. *et al.* Controlled production of aligned-nanotube bundles. *Nature* **388,** 52–55 (1997).

9. Chhowalla, M. *et al.* Growth process conditions of vertically aligned carbon nanotubes using plasma enhanced chemical vapor deposition. *J. Appl. Phys.* **90,** 5308–5317 (2001).

10. Choi, W. K. *et al.* A Combined Top-Down and Bottom-Up Approach for Precise Placement of Metal Nanoparticles on Silicon. *Small* **4,** 330–333 (2008).

11. Young, T. An Essay on the Cohesion of Fluids. *Philos. Trans. R. Soc. Lond.* **95,** 65–87 (1805).

12. Reiter, G. Dewetting of thin polymer films. *Phys. Rev. Lett.* **68,** 75–78 (1992).

13. Xie, R., Karim, A., Douglas, J. F., Han, C. C. & Weiss, R. A. Spinodal Dewetting of Thin Polymer Films. *Phys. Rev. Lett.* **81,** 1251–1254 (1998).

14. Henley, S. J., Carey, J. D. & Silva, S. R. P. Pulsed-laser-induced nanoscale island formation in thin metal-on-oxide films. *Phys. Rev. B* **72,** 195408 (2005).

15. Bischof, J., Scherer, D., Herminghaus, S. & Leiderer, P. Dewetting Modes of Thin Metallic Films: Nucleation of Holes and Spinodal Dewetting. *Phys. Rev. Lett.* **77,** 1536–1539 (1996).

16. Khenner, M., Yadavali, S. & Kalyanaraman, R. Formation of organized nanostructures from unstable bilayers of thin metallic liquids. *Phys. Fluids* **23,** 122105–122105–14 (2011).

17. Yadavali, S., Krishna, H. & Kalyanaraman, R. Morphology transitions in bilayer spinodal dewetting systems. *Phys. Rev. B* **85,** 235446 (2012).

18. Oh, Y.-J., Kim, J.-H., Thompson, C. V. & Ross, C. A. Templated assembly of Co-Pt nanoparticles via thermal and laser-induced dewetting of bilayer metal films. *Nanoscale* **5,** 401–407 (2013).

19. Hu, X., Cahill, D. G. & Averback, R. S. Nanoscale pattern formation in Pt thin films due to ion-beam-induced dewetting. *Appl. Phys. Lett.* **76,** 3215–3217 (2000).

20. Matheswaran, P. *et al.* 130 MeV Au ion irradiation induced dewetting on In2Te3 thin film. *Appl. Surf. Sci.* **258,** 8558–8563 (2012).

21. Jacobs, K., Seemann, R. & Herminghaus, S. *Stability and dewetting of thin liquid films*. (2008). at <http://arxiv.org/abs/0805.4336>

22. Thiele, U., Velarde, M. & Neuffer, K. Dewetting: Film Rupture by Nucleation in the Spinodal Regime. *Phys. Rev. Lett.* **87,** (2001).

23. Balluffi, R. W., Allen, S. M., Carter, W. C. & Kemper, R. A. *Kinetics of materials*. (J. Wiley & Sons, 2005).

24. Herminghaus, S. *et al.* Spinodal Dewetting in Liquid Crystal and Liquid Metal Films. *Science* **282,** 916–919 (1998).

25. Becker, J. *et al.* Complex dewetting scenarios captured by thin-film models. *Nat. Mater.* **2,** 59–63 (2003).

26. Israelachvili, J. N. *Intermolecular and Surface Forces*. (Academic Press, 2010).

27. Giermann, A. L. & Thompson, C. V. Solid-state dewetting for ordered arrays of crystallographically oriented metal particles. *Appl. Phys. Lett.* **86,** 121903–121903–3 (2005).

28. Kim, D., Giermann, A. L. & Thompson, C. V. Solid-state dewetting of patterned thin films. *Appl. Phys. Lett.* **95,** 251903–251903–3 (2009).

29. Oh, Y.-J., Ross, C. A., Jung, Y. S., Wang, Y. & Thompson, C. V. Cobalt nanoparticle arrays made by templated solid-state dewetting. *Small Weinh. Bergstr. Ger.* **5,** 860–865 (2009).

30. Petersen, J. & Mayr, S. G. Dewetting of Ni and NiAg solid thin films and formation of nanowires on ripple patterned substrates. *J. Appl. Phys.* **103,** 023520–023520–8 (2008).

31. Thompson, C. V. Solid-State Dewetting of Thin Films. *Annu. Rev. Mater. Res.* **42,** 399–434 (2012).

32. Strobel, S., Kirkendall, C., Chang, J.-B. & Berggren, K. K. Sub-10 nm structures on silicon by thermal dewetting of platinum. *Nanotechnology* **21,** 505301 (2010).

33. Luber, E. J., Olsen, B. C., Ophus, C. & Mitlin, D. Solid-state dewetting mechanisms of ultrathin Ni films revealed by combining in situ time resolved differential reflectometry monitoring and atomic force microscopy. *Phys. Rev. B* **82,** (2010).

34. Wang, D. & Schaaf, P. Solid-state dewetting for fabrication of metallic nanoparticles and influences of nanostructured substrates and dealloying. *Phys. Status Solidi A* **210,** 1544–1551 (2013).

35. Ruffino, F. & Grimaldi, M. G. Dewetting of template-confined Au films on SiC surface: From patterned films to patterned arrays of nanoparticles. *Vacuum* **99,** 28–37 (2013).

36. Manuela Müller, C. & Spolenak, R. Dewetting of Au and AuPt alloy films: A dewetting zone model. *J. Appl. Phys.* **113,** 094301–094301–13 (2013).

37. Mullins, W. W. Flattening of a Nearly Plane Solid Surface due to Capillarity. *J. Appl. Phys.* **30,** 77–83 (1959).

38. Thompson, C. V. 3.47 Processing of Materials on the Nanoscale Lecture Notes, Massachusetts Institute of Technology. (2009).

39. Mullins, W. W. Theory of Thermal Grooving. *J. Appl. Phys.* **28,** 333–339 (1957).

40. Srolovitz, D. J. & Safran, S. A. Capillary instabilities in thin films. I. Energetics. *J. Appl. Phys.* **60,** 247–254 (1986).

41. Srolovitz, D. J. & Safran, S. A. Capillary instabilities in thin films. II. Kinetics. *J. Appl. Phys.* **60,** 255–260 (1986).

42. Gadkari, P. R., Warren, A. P., Todi, R. M., Petrova, R. V. & Coffey, K. R. Comparison of the agglomeration behavior of thin metallic films on SiO2. *J. Vac. Sci. Technol. Vac. Surf. Films* **23,** 1152–1161 (2005).

43. Jiran, E. & Thompson, C. V. Capillary instabilities in thin films. *J. Electron. Mater.* **19,** 1153–1160 (1990).

44. Brandon, R. & Bradshaw, F. J. *THE MOBILITY OF THE SURFACE ATOMS OF COPPER AND SILVER EVAPORATED DEPOSITS.* (1966).

45. Wong, H., Voorhees, P. W., Miksis, M. J. & Davis, S. H. Periodic mass shedding of a retracting solid film step. *Acta Mater.* **48,** 1719–1728 (2000).

46. Kan, W. & Wong, H. Fingering instability of a retracting solid film edge. *J. Appl. Phys.* **97,** 043515 (2005).

47. Ishikawa, Y., Imai, Y., Ikeda, H. & Tabe, M. Pattern-induced alignment of silicon islands on buried oxide layer of silicon-on-insulator structure. *Appl. Phys. Lett.* **83,** 3162 (2003).

48. Sutter, P., Ernst, W., Choi, Y. S. & Sutter, E. Mechanisms of thermally induced dewetting of ultrathin silicon-on-insulator. *Appl. Phys. Lett.* **88,** 141924 (2006).

49. Danielson, D. T., Sparacin, D. K., Michel, J. & Kimerling, L. C. Surface-energy-driven dewetting theory of silicon-on-insulator agglomeration. *J. Appl. Phys.* **100,** 083507 (2006).

50. Ye, J. Solid-state Dewetting of Continuous and Patterned Single Crystal Ni Thin Films. (MIT, 2011).

51. Rayleigh, L. On The Instability Of Jets. *Proc. Lond. Math. Soc.* **s1-10,** 4–13 (1878).

52. Wille, L. T. *Mechanisms and principles of epitaxial growth in metallic systems: symposium held April 13-14, 1998, San Francisco, California, U.S.A.* (Materials Research Society, 1998).

53. Zotov, A. V. & Saranin, A. A. Island coarsening. at <http://eng.thesaurus.rusnano.com/wiki/article5246>

54. Porter, D. A. & Easterling, K. E. *Phase Transformations in Metals and Alloys, Third Edition (Revised Reprint).* (CRC Press, 1992).

55. Winterbottom, W. L. Equilibrium shape of a small particle in contact with a foreign substrate. *Acta Metall.* **15,** 303–310 (1967).

56. Müller, C. M., Mornaghini, F. C. F. & Spolenak, R. Ordered arrays of faceted gold nanoparticles obtained by dewetting and nanosphere lithography. *Nanotechnology* **19,** 485306 (2008).

57. Kojima, Y. & Kato, T. Nanoparticle formation in Au thin films by electron-beam-induced dewetting. *Nanotechnology* **19,** 255605 (2008).

58. Nichols, F. A. & Mullins, W. W. Morphological Changes of a Surface of Revolution due to Capillarity-Induced Surface Diffusion. *J. Appl. Phys.* **36,** 1826–1835 (2004).

59. Jiran, E. & Thompson, C. V. Capillary instabilities in thin, continuous films. *Thin Solid Films* **208,** 23–28 (1992).

60. Wang, D. & Schaaf, P. Two-dimensional nanoparticle arrays formed by dewetting of thin gold films deposited on pre-patterned substrates. *J. Mater. Sci. Mater. Electron.* (2010). doi:10.1007/s10854-010-0260-2

61. Basu, J., Carter, C. B., Divakar, R., Mukherjee, B. & Ravishankar, N. Nanopatterning by solid-state dewetting on reconstructed ceramic surfaces. *Appl. Phys. Lett.* **94,** 171114 (2009).

62. Giermann, A. L. & Thompson, C. V. Three-dimensional graphoepitaxial alignment resulting from solid-state dewetting of Au films on surfaces with monoperiodic topography. *Appl. Phys. Lett.* **101,** 051904 (2012).

63. Callister, W. D. *Materials Science and Engineering: An Introduction.* (John Wiley & Sons Australia, Limited, 2006).

64. Haniff, M. A. S. M. *et al.* Formation of Co, Fe, and Co–Fe nanoparticles through solid-state dewetting in the presence of hydrogen plasma and their electrical properties. *Vacuum* **101,** 371–376 (2014).

65. Wang, D. & Schaaf, P. Nanoporous gold nanoparticles. *J. Mater. Chem.* **22,** 5344 (2012).

66. Wang, D., Ji, R., Albrecht, A. & Schaaf, P. Ordered arrays of nanoporous gold nanoparticles. *Beilstein J. Nanotechnol.* **3,** 651–657 (2012).

67. Choi, Y. & Suresh, S. Size effects on the mechanical properties of thin polycrystalline metal films on substrates. *Acta Mater.* **50,** 1881–1893 (2002).

68. Dehm, G., Wagner, T., Balk, J., Arzt, E. & Inkson, B. J. Plasticity and Interfacial Dislocation Mechanisms in Epitaxial and Polycrystalline Al Films Constrained by Substrates. *J Mater Sci Technol* **18,** 113–117 (2002).

69. Fong, D. D. Stresses in Cu Thin Films and Ag/Ni Multilayers. (Harvard University, 2001).

70. Wang, D. & Schaaf, P. Ni–Au bi-metallic nanoparticles formed via dewetting. *Mater. Lett.* **70,** 30–33 (2012).

71. Franke, P. & Neuschütz, D. in *Binary Systems. Part 5: Binary Systems Supplement 1* (eds. Franke, P. & Neuschütz, D.) 1–4 (Springer Berlin

Heidelberg, 2007). at <http://link.springer.com/chapter/10.1007/978-3-540-45280-5_30>

72. Amram, D., Klinger, L. & Rabkin, E. Phase transformations in Au(Fe) nano- and microparticles obtained by solid state dewetting of thin Au–Fe bilayer films. *Acta Mater.* **61,** 5130–5143 (2013).

73. Juszczyk, W., Karpiński, Z., Łomot, D. & Pielaszek, J. Transformation of Pd/SiO2 into palladium silicide during reduction at 450 and 500 °C. *J. Catal.* **220,** 299–308 (2003).

74. Plummer, J. D., Deal, M. & Griffin, P. D. *Silicon VLSI Technology: Fundamentals, Practice, and Modeling*. (Prentice Hall, 2000).

75. Ghandhi, S. K. *VLSI Fabrication Principles: Silicon and Gallium Arsenide, 2nd Edition*. (Wiley-Interscience, 1994).

76. Smith, H. I. A review of submicron lithography. *Superlattices Microstruct.* **2,** 129–142 (1986).

77. Smith, H. I. Low cost nanolithography with nanoaccuracy. *Phys. E Low-Dimens. Syst. Nanostructures* **11,** 104–109 (2001).

78. Choi, W. K. *et al.* Synthesis of Silicon Nanowires and Nanofin Arrays Using Interference Lithography and Catalytic Etching. *Nano Lett.* **8,** 3799–3802 (2008).

79. Jang, H. S., Kim, G. H., Lee, J. & Choi, K. B. Eliminating the undercut phenomenon in interference lithography for the fabrication of nano-imprint lithography stamp. *Curr. Appl. Phys.* **10,** 1436–1441 (2010).

80. Reimer, L. *Scanning Electron Microscopy: Physics of Image Formation and Microanalysis*. (Springer, 1998).

81. Egerton, R. F. *Physical Principles of Electron Microscopy: An Introduction to TEM, SEM, and AEM*. (Springer, 2005).

82. Williams, D. B. & Carter, C. B. *Transmission Electron Microscopy: A Textbook for Materials Science*. (Springer, 2009).

83. Bell, D. C. & Garratt-Reed, A. J. *Energy Dispersive X-ray Analysis in the Electron Microscope*. (Garland Science, 2003).

84. Nalwa, H. S. *Handbook of Thin Films: Deposition and Processing*. (Academic Press, 2001).

85. Ulaby, F. F. T., Michielssen, E. & Ravaioli, U. *Fundamentals of Applied Electromagnetics*. (Prentice Hall PTR, 2010).

86. Ishida, K. & Nishizawa, T. The Co-Pd (Cobalt-Palladium) System. *J. Phase Equilibria* **12,** 83–87 (1991).

87. Li, H.-T. *et al.* Interfacial Stoichiometry and Adhesion at Metal/α-Al2O3 Interfaces: Interfacial Stoichiometry and Adhesion at Metal/α-Al2O3 Interfaces. *J. Am. Ceram. Soc.* **94,** s154–s159 (2011).

88. Zhang, J.-M., Ma, F. & Xu, K.-W. Calculation of the surface energy of FCC metals with modified embedded-atom method. *Appl. Surf. Sci.* **229,** 34–42 (2004).

89. Alde ń, M., Mirbt, S., Skriver, H. L., Rosengaard, N. M. & Johansson, B. Surface magnetism in iron, cobalt, and nickel. *Phys. Rev. B* **46,** 6303–6312 (1992).

90. Tu, K.-N. *Electronic Thin-Film Reliability*. (Cambridge University Press, 2010).

91. Zucker, R. V., Chatain, D., Dahmen, U., Hag ège, S. & Carter, W. C. New software tools for the calculation and display of isolated and attached interfacial-energy minimizing particle shapes. *J. Mater. Sci.* **47,** 8290–8302 (2012).

92. Wolfram CDF Player for Interactive Computable Document Format. at <http://www.wolfram.com/cdf-player/>

93. EniG. Periodic Table of the Elements, Calculators, and Printable Materials. at <http://www.periodni.com/index.html>

94. Zhu, T. *et al.* Roughening of Pt nanoparticles induced by surface-oxide formation. *Phys. Chem. Chem. Phys.* **15,** 2268–2272 (2013).

95. Dobbrow, C. & Schmidt, A. M. Improvement of the oxidation stability of cobalt nanoparticles. *Beilstein J. Nanotechnol.* **3,** 75–81 (2012).

96. Okkerse, B. Self-Diffusion of Gold. *Phys. Rev.* **103,** 1246–1249 (1956).

97. Neumann, G. M. *Surface self-diffusion of metals,*. (Diffusion Information Center, 1972).

98. Beszeda, I., Gontier-Moya, E. G. & Imre, Á. W. Surface Ostwald-ripening and evaporation of gold beaded films on sapphire. *Appl. Phys. A* **81,** 673–677 (2005).

99. Peterson, N. L. Isotope Effect in Self-Diffusion in Palladium. *Phys. Rev.* **136,** A568–A574 (1964).

100. Philibert, J.-M. *Atom movements - Diffusion and mass transport in solids*. (EDP Sciences, 2012).

101. Imre, Á. & Beke, D. L. Determination of surface diffusion parameters of Pd on sapphire from SEM measurements of morphological changes of beaded films. *Appl. Phys. A* **72,** 357–360 (2001).

102. Bussmann, W., Herzig, C., Rempp, W., Maier, K. & Mehrer, H. Isotope effect and self-diffusion in face-centred cubic cobalt. *Phys. Status Solidi A* **56,** 87–97 (1979).

103. Mills, B. & Howey, J. R. Surface Diffusion of Cobalt. *Met. Sci.* **8,** 125–128 (1974).

104. Kailasam, S. K., Lacombe, J. C. & Glicksman, M. E. Evaluation of the methods for calculating the concentration-dependent diffusivity in binary systems. *Metall. Mater. Trans. A* **30,** 2605–2610 (1999).

105. Rasband, W. S. ImageJ (U.S. National Institutes of Health, Bethesda, Maryland, USA, 1997-2012). at <http://imagej.nih.gov/ij/>

106. Brown, A. M. & Ashby, M. F. Correlations for diffusion constants. *Acta Metall.* **28,** 1085–1101 (1980).

107. Ellingham, H. J. T. Reducibility of oxides and sulfides in metallurgical processes. *J. Soc. Chem. Ind.* **63,** 125 (1944).

108. Prasad, J. J. B. & Reddy, K. V. Self diffusion studies on cobalt thin films. *Bull. Mater. Sci.* **7,** 15–20 (1985).

109. Beszeda, I., Gontier-Moya, E. G. & Beke, D. L. Investigation of mass transfer surface self-diffusion on palladium. *Surf. Sci.* **547,** 229–238 (2003).

110. Okamoto, H., Massalski, T. B., Nishizawa, T. & Hasebe, M. The Au-Co (Gold-Cobalt) system. *Bull. Alloy Phase Diagr.* **6,** 449–454 (1985).

111. Krishna, H. *et al.* Self-Organization of Nanoscale Multilayer Liquid Metal Films: Experiment and Theory. *ACS Nano* **5,** 470–476 (2011).

112. Sachan, R. *et al.* Self-organized bimetallic Ag–Co nanoparticles with tunable localized surface plasmons showing high environmental stability and sensitivity. *Nanotechnology* **23,** 275604 (2012).

113. Bhushan, B. Adhesion and stiction: Mechanisms, measurement techniques, and methods for reduction. *J. Vac. Sci. Technol. B Microelectron. Nanometer Struct.* **21,** 2262 (2003).

114. Wen, T. & Krishnan, K. M. Cobalt-based magnetic nanocomposites: fabrication, fundamentals and applications. *J. Phys. Appl. Phys.* **44,** 393001 (2011).

115. Ohring, M. *Materials Science of Thin Films*. (Academic Press, 2001).

116. Honig, R. Vapor pressure data for the solid and liquid elements. *RCA Rev.* **23,** 567–586 (1962).

117. Jalani, G. *et al.* Controlled biohybrid nanoprobes with silver nanoparticle clusters for Raman imaging. *Analyst* **138,** 4756–4759 (2013).

118. Lu, Y., Liu, G. L. & Lee, L. P. High-Density Silver Nanoparticle Film with Temperature-Controllable Interparticle Spacing for a Tunable Surface Enhanced Raman Scattering Substrate. *Nano Lett.* **5,** 5–9 (2005).

119. Bu, T., Zako, T., Fujita, M. & Maeda, M. Detection of DNA induced gold nanoparticle aggregation with dark field imaging. *Chem. Commun.* **49,** 7531 (2013).

120. New, R. M. H., Pease, R. F. W. & White, R. L. Lithographically patterned single-domain cobalt islands for high-density magnetic recording. *J. Magn. Magn. Mater.* **155,** 140–145 (1996).

121. S Yamamoto, T. A. Cobalt ferrite thin film hard disk for high-density perpendicular magnetic recording.

122. Hasanzadeh, M. *et al.* Cobalt hydroxide nanoparticles modified glassy carbon electrode as a biosensor for electrooxidation and determination of some amino acids. *Anal. Biochem.* **389,** 130–137 (2009).

123. Niu, S., Sun, J., Nan, C. & Lin, J. Sensitive DNA biosensor improved by 1,10-phenanthroline cobalt complex as indicator based on the electrode modified by gold nanoparticles and graphene. *Sens. Actuators B Chem.* **176,** 58–63 (2013).

124. Zhang, H. *et al.* The nature of cobalt species in carbon nanotubes and their catalytic performance in Fischer–Tropsch reaction. *J. Mater. Chem.* **19,** 9241–9249 (2009).

125. He, M. *et al.* Chiral-Selective Growth of Single-Walled Carbon Nanotubes on Lattice-Mismatched Epitaxial Cobalt Nanoparticles. *Sci. Rep.* **3,** (2013).

126. Varadan, V. K., Chen, L. & Xie, J. *Nanomedicine: Design and Applications of Magnetic Nanomaterials, Nanosensors and Nanosystems.* (John Wiley & Sons, 2008).

127. Lee, B. W., Alsenz, R., Ignatiev, A. & Van Hove, M. A. Surface structures of the two allotropic phases of cobalt. *Phys. Rev. B* **17,** 1510–1520 (1978).

128. *Materials Science with Ion Beams.* at <http://www.springer.com/materials/book/978-3-540-88788-1>

129. Liu, W. K. & Santos, M. B. *Thin Films: Heteroepitaxial Systems.* (World Scientific, 1999).

130. Griffiths, D. J. *Introduction to electrodynamics.* (Prentice Hall, 1999).

131. Poudyal, N. *Fabrication of Superparamagnetic and Ferromagnetic Nanoparticles*. (ProQuest, 2008).

132. Binns, C. *Introduction to Nanoscience and Nanotechnology*. (John Wiley & Sons, 2010).

133. Radu, C. *Study of Magnetization Switching in Coupled Magnetic Nanostructured Systems*. (ProQuest, 2008).

134. Dutta, B. N. & Dayal, B. Lattice Constants and Thermal Expansion of Palladium and Tungsten up to 878 ℃ by X-Ray Method. *Phys. Status Solidi B* **3,** 2253–2259 (1963).

135. Oleinik, I. I., Yu, E. & Pettifor, D. G. First-principles modelling of magnetic tunnel junctions. *Psi-K Sci. Highlight Mon.* **40,** (2000).

136. Kraus, L. & Švec, P. Magnetoelastic hysteresis of amorphous ribbons. *J. Appl. Phys.* **93,** 7220–7222 (2003).

137. Tompkins, H. G. & Augis, J. A. The oxidation of cobalt in air from room temperature to 467 °C. *Oxid. Met.* **16,** 355–369 (1981).

138. Varón, M. *et al.* Spontaneous formation of hollow cobalt oxide nanoparticles by the Kirkendall effect at room temperature at the water–air interface. *Nanoscale* **5,** 2429 (2013).

139. Bozorth, R., Wolff, P., Davis, D., Compton, V. & Wernick, J. Ferromagnetism in Dilute Solutions of Cobalt in Palladium. *Phys. Rev.* **122,** 1157–1160 (1961).

140. Hashimoto, S., Ochiai, Y. & Aso, K. Perpendicular Magnetic Anisotropy in Sputtered CoPd Alloy Films. *Jpn. J. Appl. Phys.* **28,** 1596–1599 (1989).

141. Constant, F. W. The Magnetic Properties of Certain Pt-Co and Pd-Co Alloys. *Phys. Rev.* **36,** 1654–1660 (1930).

142. Tovar Costa, M. V., de Castro Barbosa, A. C. & Costa, A. T. Giant magnetic moment dynamics in Pd. *Phys. Status Solidi B* **241,** 2415–2418 (2004).

143. Crangle, J. & Scott, W. R. Dilute Ferromagnetic Alloys. *J. Appl. Phys.* **36,** 921–928 (2004).

144. Ng, H. T. *et al.* Single Crystal Nanowire Vertical Surround-Gate Field-Effect Transistor. *Nano Lett.* **4,** 1247–1252 (2004).

145. Shao, M.-W. *et al.* Fabrication and application of long strands of silicon nanowires as sensors for bovine serum albumin detection. *Appl. Phys. Lett.* **87,** 183106–183106–3 (2005).

146. Kelzenberg, M. D. *et al.* Photovoltaic Measurements in Single-Nanowire Silicon Solar Cells. *Nano Lett* **8,** 710–714 (2008).

147. Smith, R. C. & Silva, S. R. P. Maximizing the electron field emission performance of carbon nanotube arrays. *Appl. Phys. Lett.* **94,** 133104–133104–3 (2009).

148. Yun, J. *et al.* Converting carbon nanofibers to carbon nanoneedles: catalyst splitting and reverse motion. *Nanoscale* **2,** 2180–2185 (2010).

149. Westwater, J. Growth of silicon nanowires via gold/silane vapor–liquid–solid reaction. *J. Vac. Sci. Technol. B Microelectron. Nanometer Struct.* **15,** 554 (1997).

150. Carole, D. *et al.* Growth of silicon oxide nanowires at low temperature using tin hydroxide catalyst. *J. Cryst. Growth* (2011).

151. Cui, Y., Lauhon, L. J., Gudiksen, M. S., Wang, J. & Lieber, C. M. Diameter-controlled synthesis of single-crystal silicon nanowires. *Appl. Phys. Lett.* **78,** 2214–2216 (2001).

152. Kolb, F. M. *et al.* Analysis of Silicon Nanowires Grown by Combining SiO Evaporation with the VLS Mechanism. *J. Electrochem. Soc.* **151,** G472–G475 (2004).

153. Zhang, J.-G. *et al.* Vapor-induced solid–liquid–solid process for silicon-based nanowire growth. *J. Power Sources* **195,** 1691–1697 (2010).

154. Yu, L. & Roca i Cabarrocas, P. Initial nucleation and growth of in-plane solid-liquid-solid silicon nanowires catalyzed by indium. *Phys. Rev. B* **80,** 085313 (2009).

155. Elechiguerra, J., Manriquez, J. & Yacaman, M. Growth of amorphous SiO2 nanowires on Si using a Pd/Au thin film as a   catalyst RID B-5622-2009. *Appl. Phys. -Mater. Sci. Process.* **79,** 461–467 (2004).

156. Yang, Z. *et al.* Growth of amorphous SiO2 nano-wires on pre-oxidized silicon substrate via chemical vapor deposition. *J. Non-Cryst. Solids* **354,** 1731–1735 (2008).

157. Lee, J.-B., Choi, C.-J. & Seong, T.-Y. Growth of amorphous silica nanowires using nickel silicide catalyst by a thermal annealing process. *Curr. Appl. Phys.* **11,** 199–202 (2011).

158. Yan, H. . *et al.* Growth of amorphous silicon nanowires via a solid-liquid-solid mechanism. *Chem. Phys. Lett.* **323,** 224–228 (2000).

159. Wang, C.-Y., Chan, L.-H., Xiao, D.-Q., Lin, T.-C. & Shih, H. C. Mechanism of solid-liquid-solid on the silicon oxide nanowire growth. *J. Vac. Sci. Technol. B Microelectron. Nanometer Struct.* **24,** 613 (2006).

160. Park, H.-K. *et al.* Formation of silicon oxide nanowires directly from Au/Si and Pd-Au/Si substrates. *Phys. E-Low-Dimens. Syst. Nanostructures* **37,** 158–162 (2007).

161. Tuan, H.-Y., Lee, D. C. & Korgel, B. A. Nanocrystal-mediated crystallization of silicon and germanium nanowires in organic solvents: The role of catalysis and solid-phase seeding RID C-1835-2011. *Angew. Chem.-Int. Ed.* **45,** 5184–5187 (2006).

162. Carter, J. D. *et al.* Silicon-based nanowires from silicon wafers catalyzed by cobalt nanoparticles in a hydrogen environment. *Chem. Commun.* 2274 (2005). doi:10.1039/b417740a

163. Zhang, Z., Liu, L., Shimizu, T., Senz, S. & G\ösele, U. Synthesis of silicon nanotubes with cobalt silicide ends using anodized aluminum oxide template. *Nanotechnology* **21,** 055603 (2010).

164. Jeon, M., Uchiyama, H. & Kamisako, K. Characterization of Tin-catalyzed silicon nanowires synthesized by the hydrogen radical-assisted deposition method. *Mater. Lett.* **63,** 246–248 (2009).

165. Chen, Z. H. *et al.* Applications of silicon nanowires functionalized with palladium nanoparticles in hydrogen sensors. *Nanotechnology* **18,** 345502 (2007).

166. Sharma, S. & Sunkara, M. Direct synthesis of single-crystalline silicon nanowires using molten gallium and silane plasma RID A-3033-2008. *Nanotechnology* **15,** 130–134 (2004).

167. Zhang, Z., Shimizu, T., Chen, L., Senz, S. & Gösele, U. Bottom-Imprint Method for VSS Growth of Epitaxial Silicon Nanowire Arrays with an Aluminium Catalyst. *Adv. Mater.* **21,** 4701–4705 (2009).

168. Wang, Y., Schmidt, V., Senz, S. & Gosele, U. Epitaxial growth of silicon nanowires using an aluminium catalyst. *Nat Nano* **1,** 186–189 (2006).

169. Hofmann, S. *et al.* Ledge-flow-controlled catalyst interface dynamics during Si nanowire growth. *Nat Mater* **7,** 372–375 (2008).

170. Renard, V. T. *et al.* Catalyst preparation for CMOS-compatible silicon nanowire synthesis. *Nat Nano* **4,** 654–657 (2009).

171. Kuo, C. Y. & Gau, C. Vapor–solid–solid growth of crystalline silicon nanowires using anodic aluminum oxide template. *Thin Solid Films* **519,** 3603–3607 (2011).

172. Mbenkum, B. N. *et al.* Low-Temperature Growth of Silicon Nanotubes and Nanowires on Amorphous Substrates. *ACS Nano* **4,** 1805–1812 (2010).

173. Sha, J. *et al.* Silicon Nanotubes. *Adv. Mater.* **14,** 1219–1221 (2002).

174. Warner, J. S. The Free Energy of Formation of Palladium Oxide. *J. Electrochem. Soc.* **114,** 68–71 (1967).

175. Okamoto, H. Pd-Si (Palladium-Silicon). *J. Phase Equilibria Diffus.* **28,** 231–232 (2007).

176. Oates, W. A. & Flanagan, T. B. The reaction of hydrogen atoms with palladium and its alloys. *Can. J. Chem.* **53,** 694–701 (1975).

177. Kawasaki, A., Itoh, S., Shima, K. & Yamazaki, T. Deformation of palladium plates by a small external stress during hydrogen absorption and desorption. *Mater. Sci. Eng. A* **551,** 231–235 (2012).

178. arXiv, E. T. F. the. Absorbing Hydrogen Turns Palladium Into A Quasi Liquid. *MIT Technology Review* (2010). at <http://www.technologyreview.com/view/421755/absorbing-hydrogen-turns-palladium-into-a-quasi-liquid/>

179. Tso, S. T. & Pask, J. A. Reaction of Fused Silica With Hydrogen Gas. *J. Am. Ceram. Soc.* **65,** 457–460 (1982).

180. OZTURK, B. & FRUEHAN, R. The rate of formation of SiO by the reaction of CO or H2 with silica and silicate slags. *Metall. Trans. B-Process Metall.* **16,** 801–806 (1985).

181. Tromp, R., G. Rubloff, Balk, P., LeGoues, F. & van Loenen, E. High-Temperature SiO2 Decomposition at the SiO2/Si Interface. *Phys. Rev. Lett.* **55,** 2332–2335 (1985).

182. Sasse, H. -E & König, U. SiO diffusion during thermal decomposition of SiO2. *J. Appl. Phys.* **67,** 6194–6196 (1990).

183. Davis, S. G., Anthrop, D. F. & Searcy, A. W. Vapor Pressure of Silicon and the Dissociation Pressure of Silicon Carbide. *J. Chem. Phys.* **34,** 659–664 (1961).

184. Langmuir, I. The Vapor Pressure of Metallic Tungsten. *Phys. Rev.* **2,** 329–342 (1913).

185. Smith, D. L. *Thin-film deposition: principles and practice.* (McGraw-Hill Professional, 1995).

186. Vlasyuk, R. Z., Kravchenko, L. F., Kurochkin, V. D. & Radomysel'skii, I. D. Evaporation of the main components of P/M brass during heating. *Powder Metall. Met. Ceram.* **26,** 123–126 (1987).

187. Siddiqui, R. A. Experimental Investigations of Thermodynamic Properties of Organometallic Compounds, PhD Thesis. (Universitat Duisburg-Essen, 2009).

188. Singhal, S. C., Dokiya, M., Division, E. S. H. T. M. & Division, E. S. B. *Solid oxide fuel cells: (SOFC VI)⬚: proceedings of the Sixth International Symposium.* (The Electrochemical Society, 1999).

189. Helveg, S. *et al.* Atomic-scale imaging of carbon nanofibre growth. *Nature* **427,** 426–429 (2004).

190. Maier, S. A. *et al.* Plasmonics—A Route to Nanoscale Optical Devices. *Adv. Mater.* **13,** 1501–1505 (2001).

191. Quinten, M., Leitner, A., Krenn, J. R. & Aussenegg, F. R. Electromagnetic energy transport via linear chains of silver nanoparticles. *Opt. Lett.* **23,** 1331–1333 (1998).